

Syracuse University

SURFACE at Syracuse University

Dissertations - ALL

SURFACE at Syracuse University

8-26-2022

Investigation of Holographic Lattice Theories

Muhammad Asaduzzaman

Syracuse University, asaduzzamanmsu@gmail.com

Follow this and additional works at: <https://surface.syr.edu/etd>



Part of the [Elementary Particles and Fields and String Theory Commons](#)

Recommended Citation

Asaduzzaman, Muhammad, "Investigation of Holographic Lattice Theories" (2022). *Dissertations - ALL*. 1651.

<https://surface.syr.edu/etd/1651>

This Dissertation is brought to you for free and open access by the SURFACE at Syracuse University at SURFACE at Syracuse University. It has been accepted for inclusion in Dissertations - ALL by an authorized administrator of SURFACE at Syracuse University. For more information, please contact surface@syr.edu.

Abstract

The Anti-de Sitter/Conformal Field theory (AdS/CFT) correspondence, also known as holography, has been the focus of a great deal of interest and research for the last two decades. It has improved our understanding of general relativity and quantum field theories simultaneously through the interplay between these two different kinds of theories. However, there are still many aspects of holography that we do not understand or demand further analysis. Perturbative quantum field theory and perturbative metric expansion techniques are not equipped to investigate holography in some of the most interesting regimes such as the strongly interacting gravitational theory in anti-de Sitter space (that potentially can have a dual field theory at the boundary with a small number of degrees of freedom, hence away from the large N limit).

In this thesis, I have attempted to contribute to understanding holography in these more difficult regimes. Specifically, I have used lattice techniques in Wick-rotated Anti-de Sitter (AdS) spacetime to investigate holography. After a review of the properties of Anti-de Sitter space and some continuum results, lattice construction of the hyperbolic space and the algorithms used for analysis are discussed. Our initial attempt investigated free scalar fields in hyperbolic space in two and three spacetime dimensions. It has been demonstrated that properties of the bulk lattice geometry information are encoded in the dual CFT through mapping the mass spectrum of the bulk scalar field to the scaling dimension of the boundary CFT operators. Holography has also been investigated for the nearest-neighbor Ising spin model on a hyperbolic space at various temperatures. The principal focus has been measuring boundary correlation functions over a range of temperatures. This yields a temperature-dependent scaling exponent of the boundary operator. Scaling the magnetic susceptibility data at different lattice volumes also allows us to compute the same scaling exponent, demonstrating good agreement with the correlation function measurements. A phase transition temperature in the bulk geometry can be seen to correlate with a min-

imal boundary scaling dimension. Lattice simulation results are complemented with a discussion of the high-temperature expansion and the duality (in the sense of Kramers and Wannier).

Finally, we show how lattice techniques can be used to probe strong fluctuations of the bulk geometry. A new relation of the scaling dimensions to the bulk mass is derived in this regime. We show that the backreaction of fermionic matter fields can dramatically alter the nature of the bulk space. Hyperbolic space configuration dominates the dynamically generated ensemble of simplicial manifolds in the limit of a large number of Kähler-Dirac fields.

Apart from the apparent advantage of probing duality in this uncharted territory of strong geometry fluctuation and strongly coupled field theories in hyperbolic space, the tools developed in this thesis should allow investigation of different aspects of quantum information science and tensor network ideas.

Investigation of Holographic Lattice Theories

by

Muhammad Asaduzzaman

B.Sc., Bangladesh University of Engineering & Technology, 2013

M.Sc., University of Dhaka, 2016

DISSERTATION

Submitted in partial fulfillment of the requirements for the degree of

Doctor of Philosophy in Physics

Syracuse University

August 2022

Copyright © Muhammad Asaduzzaman, August 2022
All rights reserved

To everyone who is fighting against the rotten social customs and beliefs.

Acknowledgements

I am thankful to my advisor Simon Catterall for his support, encouragement, and numerous conversations during which I learned to think like a physicist. Among many other things, he taught me how to search for new exciting physics, scout through the literature on relevant topics, and use numerical simulation to develop an understanding of physics. He has been very patient with me and, over the years, helped me to be more independent in my research. Also, I learned from him how to get the most out of collaborative efforts. I have benefited from my interactions with Yannick Meurice, who taught me many aspects of quantum information science over our numerous zoom calls and in-person discussion at the University of Iowa. I thank the present and past members of the QuLat collaboration. Special thanks to Judah, with whom I have had numerous discussions and communications over slack, email, and during his stay at Syracuse University as a postdoc. I have also spent time working with Jack Laiho on Euclidean dynamical triangulations and would like to thank him for many discussions on lattice simulations and lattice gravity. I also would like to thank Jay Hubisz for many illuminating discussions during our meetings on the projects on holography. I thank Raghav for providing me useful advice during my Ph.D. journey.

I want to thank all my committee members for serving on my thesis committee: Simon Catterall, Jay Hubisz, Jack Laiho, Scott Watson, Carl Rosenzweig, and Graham Leuschke. I also am grateful to all the people working in the office of the physics department. Thanks for helping numerous times with thousands of academic and non-academic issues. Many thanks to these two kind-hearted people- Yudy, & Patty. I also would like to thank all the professors with whom I came in contact during my graduate coursework or for working with them as their teaching assistant. Interaction with them was mostly excellent, and I will be forever grateful for that. I also would like to thank the professors with whom I came in contact during my M.Sc. and B.Sc. studies, including Arshad Momen, and Golam Mohammed Bhuiyan.

At last, I would like to thank my parents for all the sacrifices they made for me. Thanks to my ma (mother) for being my first teacher in life, and thanks to my abbu (father) for being a kind soul. I thank my sister for always believing in me, and thankful for numerous

little conversations which always relieved my stress. I want to thank my wife for providing encouragement and setting me straight with logic during hard times. Sharing the Ph.D. journey with her kept me sane and focused on the goal. It will be a great deal of injustice if I do not name a few other persons who helped me grow over the years - Monowara aunt, Babu mama, Zia chacha, Gaffar Ali. I am thankful to my wonderful friends - Bashit, Rumman, Raj, Preeti, Deepa, Sumon, Anand, Shumon, Arnob, Taskin, Raghav, Emtiaz, Mamun, Abid, Goksu, Bharath, Sarthak, Chaitanya, Joe, Sirat. Also, thanks to the members of the Bangladeshi community at Syracuse and Charlottesville, VA (where I spent a wonderful summer). This thesis will not have been possible without their unending love and warmth.

List of Papers

Chapters 2, 3, 4 of the dissertation are comprised of the work carried out in the following papers.

1. **Holography on tessellations of hyperbolic space**; Muhammad Asaduzzaman, Simon Catterall, Jay Hubisz, Roice Nelson and Judah Unmuth-Yockey; Phys. Rev. D 102, 034511 (August, 2020).
<https://link.aps.org/doi/10.1103/PhysRevD.102.034511>
2. **Holography for Ising spins on the hyperbolic plane**; Muhammad Asaduzzaman, Simon Catterall, Jay Hubisz, Roice Nelson and Judah Unmuth-Yockey; arXiv:2112.00184 [hep-lat], submitted to Phys. Rev. D.
<https://arxiv.org/abs/2112.00184>
3. **Scalar fields on fluctuating hyperbolic geometries**; Muhammad Asaduzzaman, Simon Catterall; lattice proceedings, 2021.
<https://arxiv.org/abs/2112.00927>

The following research publications have not been included in the thesis due to their disjoint research field to the main theme of the dissertation work:

1. **Tensor network formulation of two-dimensional gravity**; Muhammad Asaduzzaman, Simon Catterall and Judah Unmuth-Yockey; Phys. Rev. D 102, 054510 (September, 2020).
<https://link.aps.org/doi/10.1103/PhysRevD.102.054510>
2. **Lattice Gauge Theory and Two Dimensional Quantum Gravity** Muhammad Asaduzzaman, Simon Catterall, and Judah Unmuth-Yockey; PoS LATTICE2019 (2020), 043.
<https://pos.sissa.it/363/043>

3. **Euclidean Dynamical Triangulations Revisited;** Muhammad Asaduzzaman, Simon Catterall; arXiv:2207.12642 [hep-lat] (July 2022)
<https://arxiv.org/pdf/2207.12642.pdf>

4. **Quantum Simulation of the N flavor Gross-Neveu Model** Muhammad Asaduzzaman; Simon Catterall; Goksu Can Toga; Yannick Meurice; Ryo Sakai; arXiv:2208.05906 [hep-lat] (August 2022)
<https://arxiv.org/abs/2208.05906>

Contents

1 Gravity and holography	1
1.1 Introduction	1
1.2 Maldacena’s conjecture	3
1.3 A holographic dictionary	4
1.4 Bulk scalar fields on AdS: continuum description	6
1.4.1 Classical solution of bulk field	7
1.4.2 Different quantizations	8
1.4.3 Boundary condition	10
1.4.4 Green’s function	11
1.5 Construction of Hyperbolic Lattices	13
1.6 Lattice simulation	16
1.6.1 Review of the Metropolis Algorithm	18
1.6.2 Review of the Cluster Algorithm	19
1.6.3 Monte Carlo simulation of dynamical lattice geometry	21
2 Massive scalar fields on hyperbolic space	26
2.1 Introduction	26
2.2 Two-dimensional hyperbolic geometry	28
2.3 Other two-dimensional tessellations	37
2.4 Three-dimensional hyperbolic geometry	38
2.5 Conclusions	46

3	Ising spins on hyperbolic space	49
3.1	Introduction	49
3.2	The model and bulk phase structure	51
3.3	Boundary Thermodynamics	57
3.4	Summary and Prospects	63
4	Scalar fields on fluctuating hyperbolic geometries	65
4.1	Introduction	65
4.2	Introducing bulk curvature fluctuations	67
4.3	Results: curvature-squared operator	68
4.4	Curvature fluctuation from matter fields	72
4.5	Kähler Dirac Operator Construction and Results	74
4.6	Conclusions	75
5	Conclusions	77
	Bibliography	80

List of Figures

1.1	Construction of fundamental triangle $\triangle OA_1M$ for a $\{p, q\}$ tessellated disk. $p = 4$ is considered in the diagram.	15
1.2	Ergodic moves in the class of two-dimensional triangulation. Node insertion and deletion (top), and link flip (bottom).	22
2.1	$\{3,7\}$ tessellation in the Poincare Disk model of the hyperbolic plane.	29
2.2	A zoom-in of the boundary of the Poincaré disk shown in Fig. 2.1.	29
2.3	The volume, V_e , associated with an edge is shown in yellow, and the volume, V_v , associated with a vertex is shown in blue. In two dimensions, since each p -gon has the same number of vertices as edges, these volumes are always the same (in this case they are both $1/3$ of the area of the total triangle).	30
2.4	Four different correlators corresponding to different squared bare masses are plotted in log-log coordinates for the case of a 13-layer lattice, with the squared boundary mass set to $M^2 = 1000$. The masses here from top to bottom are $m_0^2 = -0.1, 0.2, 0.5,$ and 0.8	31
2.5	The power law obtained from fitting the correlation function in Eq. (2.8) versus the squared bare mass. Here we show the result for a 13-layer lattice with squared boundary mass, $M^2 = 1000$. We find good qualitative agreement with Eq. (2.2).	33

2.6	The large-volume extrapolation of the B parameter as a function of the inverse volume of the boundary, for a boundary mass of $M^2 = 1000$. We have re-scaled by 100 triangles to remove clutter on the x -axis. We fit a line to this data to extract the B parameter at infinite volume, B_∞ . We have included the systematic error, due to the choice of the fit range, in orange.	34
2.7	The boundary two-point correlator is plotted in log-log coordinates for the lattice $\{p, q\} = \{4, 5\}$. Here four bulk masses are shown for the values of $m_0^2 = -0.1, 0.2, 0.5$, and 0.8 , with a boundary mass of $M^2 = 500$. The lattice is comprised of eight layers of squares.	35
2.8	The power-law extracted from the correlator data for the $\{p, q\} = \{4, 5\}$ lattice. This data is for a eight layer lattice with a boundary mass of $M^2 = 500$. The fit parameters for this fit are quoted inside the figure.	35
2.9	The finite-size scaling for the B fit parameter versus the inverse boundary size. Here we re-scaled the x -axis by 100 squares to declutter the axis labels. This fit is for a boundary mass of $M^2 = 500$	36
2.10	Boundary mass (M^2) dependence of the fit parameter Δ in the two point function for a 10 layer lattice in the $\{3, 8\}$ geometry. Error bars are of the order 10^{-4} or smaller and not visible in the figure.	36
2.11	The boundary two-point correlator is plotted in log-log coordinates for the lattice $\{p, q\} = \{3, 8\}$. Here four bulk masses are shown for the values of $m_0^2 = -0.1, 0.2, 0.5$, and 0.8 , with a boundary mass of $M^2 = 2000$. The lattice is comprised of 12 layers of triangles.	38
2.12	The power-law extracted from the correlator data for the $\{p, q\} = \{3, 8\}$ lattice. This data is for a eight layer lattice with a boundary mass of $M^2 = 2000$. The fit parameters for this fit are quoted inside the figure.	39
2.13	An in-space view of the order-5 cubic honeycomb.	40
2.14	Visualization of step-by-step construction of the lattice with layers of cubes in the $\{4, 3, 5\}$ honeycomb. The cube edge lengths appear to vary in length in the Poincaré ball model; however, the lattice here has a fixed edge length, a .	41

2.15	(a) The portion of volume associated with an edge of a cube highlighted, in the text, V_e . (b) The portion of volume associated with a vertex of a cube highlighted, in the text, V_v . For a lattice with uniform edge length $a = 1$, these correspond to $1/12$ and $1/8$ respectively.	42
2.16	A log-log plot of the boundary-boundary correlator, $C(r)$, as a function of distance along the boundary, for a seven-layer lattice. Here the bulk masses from top to bottom are $m_0^2 = -0.7, -0.3, 0.4$, and 0.9 , and the boundary mass is $M^2 = 10$	44
2.17	A fit of Δ versus the squared mass using Eq. (2.11) for a six-layer lattice. Here the boundary mass is $M^2 = 10$	45
2.18	The finite-size scaling of the fit parameter, A , from Eq. (2.11). The volumes have been rescaled by 1000 for readability. All three volumes use the same boundary mass of $M^2 = 10$	46
2.19	The finite-size scaling of the fit parameter, B , from Eq. (2.11). The volumes have been rescaled by 1000 for readability. All three volumes use the same boundary mass of $M^2 = 10$	47
3.1	(a) The full $\{3, 7\}$ lattice, highlighting 10 layers and 591 nodes. The first 10 layers are drawn in one color and the subsequent 3 layers each colored uniquely. (b) A close-up of the boundary of the lattice. Connectivity of the boundary vertices has no fixed pattern as additional layers are added.	51
3.2	The bulk magnetic susceptibility computed from $N_{\text{bulk}} = 591$ spins on the 10 innermost layers of the tessellation as additional outer layers are added up to a maximum of $N_0 = 3495$	52
3.3	(a) The peak in the bulk susceptibility vs $\ell = \log(N_{\text{bulk}})$ in log-log coordinates. The scaling exponent γ_B/ν_B corresponds to the slope of the fitted line. (b) Collapsing bulk susceptibility data with rescaling allows to find the exponent ν_B	54

3.4	(a) Bulk magnetization, (b) internal energy and (c) heat capacity are computed from $N_{\text{bulk}} = 591$ spins on 10 innermost layers of the tessellation as additional outer layers are added up to a maximum of $N_{\text{total}} = 3495$	55
3.5	(a) Boundary magnetization and (b) boundary susceptibility are plotted against bulk-temperature from 10 to 13 layered Poincaré disk with increasing number of boundary spins N_{∂}	56
3.6	Logarithm of the boundary susceptibility (χ_{∂}) is plotted against logarithm of the total number of boundary points (N_{∂}) for $T =$ (a) 2.7, (b) 3.0, (c) 3.4. Scaling exponents of the boundary susceptibility (γ/ν) are computed from the linear fit of the data.	57
3.7	The boundary-boundary correlation function at $T =$ (a) 2.7, (b) 3.0, (c) 3.4, plotted against boundary distance squared $r^2 \sim (1 - \cos \theta)$. Results shown here are from the analysis of a 12 layered Poincaré disk with boundary length $N_{\partial} = 1062$. χ^2 per degree of freedom and the p-value of the fits are noted in the figures.	59
3.8	The scaling exponent of the boundary spin operator computed from fits to the boundary two-point correlator, denoted by Δ , and from the finite-size scaling of the boundary susceptibility, denoted by $(1 - \gamma/\nu)/2$	60
3.9	Relation between dual inverse temperature and the dual temperature.	60
3.10	The boundary-boundary correlation function of the dual spin variable ($C = \langle \sigma_0 \sigma_r \rangle$) at $\tilde{T} =$ (a) 1.1, (b) 1.2, (c) 1.3 plotted against boundary distance squared $r^2 \sim (1 - \cos \theta)$. Results shown here are from the analysis of a six-layered $\{7, 3\}$ Poincaré disk with boundary length $N_{\partial} = 3647$	61
3.11	Scaling exponent of the dual boundary spin operator ($\tilde{\Delta}$) computed from the fits of the boundary correlator.	62
3.12	(a) Scaling exponents at direct lattice Δ vs. dual inverse temperature ($\tilde{\beta}$), and (b) scaling exponent at dual lattice ($\tilde{\beta}$) vs. inverse temperature at direct lattice (β). Linear fits at high temperature are shown with the extracted slope denoted in the figure.	62

4.1	Number of bulk vertices $N(q_B)$ with coordination number q are plotted at different β : $\beta = 0.0$ (black), $\beta = 0.01$ (blue), $\beta = 0.1$ (purple), $\beta = 0.5$ (red), $\beta = 1.0$ (cyan), and $\beta = 3.0$ (green).	68
4.2	Sample thermalized configurations from time evolution of geometry during MCMC simulation at different β	69
4.3	Two point function is plotted against boundary distance in angular coordinate for a scalar field with bulk mass $m = 0$, here $r^2 \propto (1 - \cos \theta)$. Slope of the fitted line denotes the scaling exponent Δ of the boundary operator.	70
4.4	Bulk mass dependence of the scaling exponent at (a) $\beta = 3.0$ and $\beta = 1.0$	70
4.5	Lattice propagator computed from the simulation with $N_f = 10$ Kähler Dirac fermions is plotted against distance-squared $r^2 \propto (1 - \cos \theta)$. The slope Δ of the linear fit denotes the scaling exponent of the boundary field operator.	75

List of Tables

2.1	{3, 8} tessellation results	37
-----	---------------------------------------	----

Chapter 1

Gravity and holography

1.1 Introduction

The AdS-CFT correspondence, even though it has its origins in string theory, can be understood without recourse to that theory. In essence, it posits that specific quantum field theories in d -dimensional flat space have a dual description in terms of a gravitational theory in $d + 1$ dimensions. This is a strong-weak coupling duality – strongly coupled flat space theories are described by weakly coupled gravity theories. In practice it has allowed for the study of strongly coupled field theories in terms of classical solutions of gravitational systems. It is best understood in the case of gravitational theories formulated on an anti-de Sitter background, where the dual theory is a conformal field theory residing on the boundary of anti-de Sitter space. The fact that a bulk gravity theory can be described as a field theory at the boundary of that space is why the correspondence is often termed a holographic duality. It is sometimes also referred to as gauge-gravity duality as it allows quantum mechanical features of a gauge theory to be understood in terms of gravitational observables in the dual theory - for example the finite temperature deconfinement of gauge theories in terms of transitions between different types of classical black hole. For a preliminary review on the subject matter, these review articles on AdS/CFT can be consulted [1–3].

One of the fascinating aspects of this duality is that it improves our understanding of strongly coupled field theories using gravitational techniques. On the other hand, it also opens a window on quantum gravity using flat space quantum field theory. It indeed serves

as a motivation to develop lattice techniques for investigating holography. Example of applications of holography where general relativity has improved our understanding of QFT are AdS/QCD program [4–6] and AdS/CMT program [7–9]. Before the inception of duality, lattice QCD was the only available tool to answer questions about the low energy regime of QCD. The use of duality has provided important insights into the strongly coupled regime of QCD. For example, the lower bound of the ratio of the shear viscosity to volume density was derived for a large class of strongly coupled theories using the dual description of black holes in AdS space [7]. Moreover, the techniques of duality have been used to estimate the deconfinement temperature [10] and radiation properties of a quark in quark-gluon plasma [11]. On the other hand, AdS/CMT prescription allows to explore strongly correlated condensed matter systems that are difficult to investigate with traditional condensed matter techniques. Another nice example in this field is holographic superconductivity investigated from the gravitational side of duality [12]. Cold atom experiments with optical lattices [13] can potentially investigate duality in table-top CMT experiments. AdS/CFT also revealed interesting physics pertaining to general relativity - for example, new black hole solution have been found as a result of lattice studies. In the continuum, several such solutions were found from the fluid/gravity correspondence [14], and from the investigation of superconductivity [12]. Another benefit of holographic studies has been the understanding of scenarios where the black hole is formed due to a small deformation of AdS and the scenarios with non-singular solutions (geons) to Einstein’s equation [15]. To address the same questions for non-perturbative deformations lattice simulation is likely the only viable tool in the near future.

Holography has had, and continues to have, an enormous effect on the amalgamation of different sub-fields of physics – from particle physics to condensed matter, nuclear and mathematical physics. Juan Maldacena proposed the correspondence in his seminal 1997 paper. From that point onward, it has been tested and proven to be correct in a myriad of cases. It is known to be true rigorously in certain limits where the gravitational coupling is weak and there are many local degrees of freedom. However there is no proof of the conjecture for strong gravitational coupling or for systems with only small numbers of local degrees of freedom per spacetime point. These regimes can be potentially tested using

lattice simulation which hence forms the main focus of this thesis. As a result, lattice studies will provide a potential avenue for exploring new kinds of conformal field theories. It is also interesting to point out that new applications like the ones discussed in the previous paragraph, can be originated from the lattice investigation as lattice studies potentially probe the unknown sector of the duality. For example, exploring new sectors of the phase diagram of different condensed matter systems which are in general not accessible to other methods can be explored. Many condensed matter systems have a natural representation in the lattice which hence provides an easier pathway for investigation using duality.

Now we describe the construction of this manuscript for the reader. In the remainder of this chapter, we discuss the definition of AdS/CFT correspondence and review some continuum results of the AdS/CFT dictionary. In the later part of the chapter, we review lattice construction of the hyperbolic space, metropolis and cluster algorithms, and some elementary discussion on dynamical triangulation. In chapter 2, we present the first test of lattice holography, where we discuss free scalar field model on 2D and 3D hyperbolic geometry. In the following chapter 3, we apply the lattice techniques to investigate a local interacting theory – Ising model. Finally, in chapter 4, we present results of perturbative and non-perturbative geometry fluctuation on scalar fields. We also show the backreaction effects of Kähler-Dirac matter fields on asymptotically hyperbolic spacetime. We conclude our discussion in chapter 5 summarizing the results and prospects of the work presented here.

1.2 Maldacena’s conjecture

Maldacena’s seminal paper focused on the connection between a particular Yang-Mills theory with $\mathcal{N} = 4$ supersymmetry and $SU(N_c)$ gauge symmetry in four dimensions and a certain string theory propagating on a five dimensional anti-de Sitter space [16]. In more detail the correspondence takes the form:

$$\text{String theory on } AdS_5 \times S^5 \quad \equiv \quad \mathcal{N} = 4 \text{ } SU(N) \text{ gauge theory.} \quad (1.1)$$

Evidence in favor of this theory came from both a matching of the isometries of AdS space with the conformal symmetries of the boundary theory and a correspondence between the scaling dimensions of certain operators in the $\mathcal{N} = 4$ theory and the spectrum of states of the bulk string theory in a certain limit. The correspondence can be proven perturbatively for large N_c and strong gauge coupling. It's interesting to point out that the global symmetries of the two theories match. The isometry group of AdS_5 is $SO(4, 2)$ and of S^5 is $SO(6)$. On the right hand side, $\mathcal{N} = 4$ SYM demonstrates the same symmetry groups. $SO(4, 2)$ is the conformal group in 4D and $SO(6) \sim SU(4)$ is associated with the R-symmetry of the boundary theory.

1.3 A holographic dictionary

Shortly after Maldacena's paper, Witten proposed an ansatz that allows us to relate the supergravity of the bulk with the field theory of the boundary of anti-de Sitter space [17]. Witten's paper first demonstrates that the asymptotic behavior of the bulk AdS fields determines the properties of the correlators at the boundary. To describe the ansatz mathematically, we first describe the metric of the Euclidean version of the AdS space. Consider coordinates of $(d + 1)$ dimensional Euclidean space with coordinates x_i , with $i = 0, \dots, d$. Equation of an open ball in $d + 1$ dimension can then be written as $\sum_{i=0}^d x_i^2 < 1$, and is described by the metric

$$ds^2 = \frac{4 \sum_{i=0}^d dx_i^2}{(1 - |x|^2)}. \quad (1.2)$$

Compactifying the open ball requires introduction of a non-unique function Ω on the boundary of the closed ball \bar{B}_{d+1} such that

$$ds^2 = \Omega^2 ds^2. \quad (1.3)$$

Any Ω can be chosen as long as it is positive on the open ball and has a first order zero on the boundary of the closed ball. The choice is non-unique up to a conformal transformation

$$\Omega \rightarrow \Omega \exp(\omega), \quad (1.4)$$

where ω is any real function on the closed ball. It's interesting to point out that any metric on the open ball with a double pole structure on boundary like Eqn. 1.2, induces a conformal structure on the boundary of the open ball in d -dimensional sphere S^d . On the other hand, a theorem of Graham and Lee [18] also suggests that any conformal structure on S^d arises from a unique metric upto diffeomorphism on the open ball B_{d+1} that obeys Einstein's equation with negative cosmological constant and a double-pole structure at the boundary.

Let us consider a field $\phi(\mathbf{x}, z)$ in $d + 1$ dimensional AdS space with $x_0 = z$ and $\mathbf{x} = (x_1, x_2, \dots, x_d)$. Restricted form of the bulk fields on boundary ($\phi_0^i(\mathbf{x})$), couples to the respective conformal fields \mathcal{O}^i via coupling $\int_{\partial\mathcal{M}=S^d} \phi_0^i \mathcal{O}^i$. The ansatz precisely relates the gravitational partition function Z_G with a well-defined boundary condition to the generating functional of the boundary conformal field theory

$$Z_G [\phi_0^i(x), h_{\mu\nu}; \partial M] = \left\langle \exp \left(- \sum_i \int d^d x \phi_0^i(x) \mathcal{O}^i(x) \right) \right\rangle_{\text{CFT}}. \quad (1.5)$$

The left-hand side is thus the partition function in asymptotically AdS space. On the left-hand side, ϕ_0^i is considered as the asymptotic form of the bulk fields on the boundary, and $h_{\mu\nu}$ is considered as the boundary condition for the bulk metric $g_{\mu\nu}$ which depends both on the topology of the space and on the actual form of the metric. On the right-hand side, they are considered sources or currents and relate to the conformal operators \mathcal{O}^i . Thus the asymptotic behavior of the gravity-action on the boundary of AdS space determines the correlation functions of the conformal boundary theory. Identifying the right hand side as $Z_{\text{CFT}}[\phi_0]$, n -point correlation function can be computed using the functional derivative

$$\langle \mathcal{O}^1(x_1) \cdots \mathcal{O}^n(x_n) \rangle_{\text{CFT}} \sim \frac{\delta^n}{\delta \phi_0^1(x_1) \cdots \delta \phi_0^n(x_n)} Z_{\text{CFT}}[\phi_0] \Big|_{\phi_0^i=0} \quad (1.6)$$

It is important to note that the dimensions (Δ^i) of the boundary operators (\mathcal{O}^i) are a function of the particle masses of the bulk gravity theory. A precise derivation for different types of the bulk fields in the gravity side to the boundary operator in the CFT side is beyond the scope of this thesis. However, we will state the results of the mapping of the AdS

fields to the CFT operators. First of all, the CFT operators should possess the same Lorentz structure to their corresponding bulk fields. The connection between the bulk mass and the dimension of the corresponding conformal operator has been developed for different kinds of fields — scalar fields [19–22], Dirac fields [23–25], massless vector fields [21, 26], massive vector fields [23, 27, 28], gravitons [29, 30], Rarita-Schwinger fields [31, 32], anti-symmetric p -form fields or anti-symmetric fields [33, 34], symmetric tensor fields [35]. We simply state some of the results of this dictionary in this section:

1. massive scalar field or massive spin-2 fields: $m^2\ell^2 = \Delta(\Delta - d)$
2. massless scalar field: $0 = \Delta - d$
3. Dirac spinor or Rarita-Schwinger field: $|m|\ell = \Delta - \frac{d}{2}$
4. p -form field: $m^2\ell^2 = (\Delta - p)(\Delta + p - d)$
5. rank- s symmetric tensor field: $m^2\ell^2 = (\Delta + s - 2)(\Delta - s + 2 - d)$.

In the description above, m -denotes the mass of the bulk field and ℓ is radius of curvature of the $d + 1$ dimensional AdS space, and Δ is the conformal dimension of the corresponding boundary operator. Since a massive scalar field plays a prominent role in our lattice studies, in the next subsection, we will review the derivation of the scaling exponent of the boundary field operator in terms of bare mass of the bulk field. Regularization and renormalization are required for the computation of the CFT two point functions. Different regularization can be used. However, physical results do not depend on the regularization scheme. We follow the approach known as ϵ expansion [22] in this regard. For the asymptotic prescription, see [17]. The counter-terms in two different regularization procedures would be different

1.4 Bulk scalar fields on AdS: continuum description

In this section, we consider an example of a massive free scalar field model in AdS space and demonstrate that the two point boundary correlation function indeed obeys power law as expected for a conformal field theory with a power equal to twice the scalar dimension which is determined by the bulk scalar mass.

1.4.1 Classical solution of bulk field

In this subsection, we outline the derivation of the classical solution of the free scalar field in the AdS Space. We start by writing down the Upper-Half-Plane (UHP) metric for anti-de Sitter space

$$ds^2 = \frac{\ell^2}{z^2} (\eta_{\mu\nu} dx^\mu dx^\nu + dz^2), \quad (1.7)$$

where z is scaled with the AdS radius ℓ . The corresponding scalar action takes the form

$$S = -\frac{1}{2} \int d^{d+1}X \sqrt{g} (g^{AB} \partial_A \phi \partial_B \phi + m^2 \phi^2) \quad (1.8)$$

This yields the classical equation of motion:

$$(-\Delta + m^2) \phi = 0 \quad (1.9)$$

where

$$\begin{aligned} \Delta &= \frac{1}{\sqrt{g}} \partial_A (\sqrt{g} g^{AB} \partial_B) \\ &= \frac{z^2}{\ell^2} (\partial_z^2 - (d-1)z^{-1} \partial_z + \partial_x^2) \end{aligned} \quad (1.10)$$

Separation of variables can be applied to find the solution of the differential equation in Eqn. 1.9.

$$\phi(z, x) = f(z) \Phi(x) \quad (1.11)$$

we find

$$(-\partial_E^2 - k^2) \Phi_k = 0 \quad (1.12)$$

and

$$[-z^{d+1} \partial_z (z^{-d+1} \partial_z) + m^2 \ell^2 + k^2 z^2] f_k = 0 \quad (1.13)$$

Thus

$$\phi(z, x) = \int d^d k f_k(z) \Phi_k(x) = \int \frac{d^d k}{(2\pi)^d} f_k(z) e^{ikx} \quad (1.14)$$

Defining $f_k = g_k z^{\frac{d}{2}}$,

$$(kz)^2 g_k'' + (kz) g_k' - \left(\frac{d^2}{4} + m^2 \ell^2 + k^2 z^2 \right) g_k = 0 \quad (1.15)$$

we find

$$g_k(kz) = a_k K_\nu(kz) + b_k I_\nu(kz) \quad (1.16)$$

where, $\nu = \sqrt{\frac{d^2}{4} + m^2 \ell^2}$ and

$$f_k(z) = a_k (kz)^{d/2} K_\nu(kz) + b_k (kz)^{d/2} I_\nu(kz) \quad (1.17)$$

This essentially demonstrates two different kinds of modes are present in the classical solution. The significance of these modes are discussed in the next subsection. Which of the modes survive depend on the choice of the boundary condition of the bulk fields.

1.4.2 Different quantizations

We asserted the significance of the different modes and associated the modes with different quantization schemes in this subsection. Using the limiting forms of the Bessel function at $z = 0$ and $z = \infty$, we find k -space solution assumes the following form near the boundary (at $z = 0$),

$$f_k(z) \approx (\phi_0(k) + \mathcal{O}(z^2)) z^{\Delta_-} + (\phi_1(k) + \mathcal{O}(z^2)) z^{\Delta_+} \quad (1.18)$$

with,

$$\phi_0(k) = a_k 2^{\nu-1} \Gamma(\nu) k^{\Delta_-} \quad (1.19)$$

and

$$\phi_1(k) = a_k 2^{-(\nu+1)} \Gamma(-\nu) k^{\Delta_+}. \quad (1.20)$$

Using Hamiltonian analysis it can be shown that $\phi_0(k)$ and $\phi_1(k)$ are related by a Legendre transformation [20]. The exponent Δ_\pm is given by

$$\Delta_\pm = \frac{d}{2} \pm \nu. \quad (1.21)$$

which is known as the scaling relation and will appear later when we discuss the boundary correlators. To derive this scaling relation is the central goal of the lattice simulation in our analysis of the free scalar field, which we present in the next chapter. From the expression of ν , it is evident that a small negative mass is allowed in the AdS space as long as Breitenlohner-Freedman bound $m^2\ell^2 > -\frac{d^2}{4}$ is satisfied. As long as the mass is above this limit, the negativity in m^2 does not imply the existence of tachyons since the energy associated is still positive, which is a consequence of the intrinsic negative curvature in the anti-de Sitter space. Boundary solution in the position space can be written using the Fourier transform of the boundary solution in Eqn. 1.18

$$\begin{aligned}\phi(z, \mathbf{x}) &= \int \frac{d^d k}{(2\pi)^d} f_k(z) e^{ikx} \\ &= \left(\phi_0(\mathbf{x}) + \mathcal{O}(z^2) \right) z^{\Delta_-} + \left(\phi_1(\mathbf{x}) + \mathcal{O}(z^2) \right) z^{\Delta_+},\end{aligned}\tag{1.22}$$

where, $\phi_i(x)$ is the Fourier transform of $\phi_i(k)$. Eqn. 1.22 hints that there are two possible quantization procedures which are associated with z^{Δ_+} and z^{Δ_-} part of the classical solution of the bulk field. Breitenlohner and Freedman first showed that the constraint for the existence of the two independent quantizations is [36]

$$-\frac{d^2}{4} < m^2\ell^2 < -\frac{d^2}{4} + 1.\tag{1.23}$$

Putting the asymptotic form in the action in Eqn. 1.8, we can find the bound of the operator dimension $\Delta > d/2$. However, the bound can be relaxed, which is easily seen from the alternative form of the action for the free scalar in the AdS space

$$S = \frac{1}{2} \int d^{d+1}x \sqrt{g} \phi (-\nabla^2 + m^2) \phi.\tag{1.24}$$

The less-restrictive bound $\Delta = (d/2 - 1)$ keeps the action finite and allows both modes for the mass-constraint described by Eqn. 1.23 due to Breitenlohner and Freedman. Thus as described in [36], one Lagrangian in AdS space can describe two different quantum field theories depending on the choice of the boundary condition.

1.4.3 Boundary condition

It is somewhat puzzling how two different quantization schemes are related. Computation of the two-point correlators of the free scalar model in the presence of different boundary conditions is discussed explicitly by Minces *et. el.* [37]. We do not attempt to reproduce their derivation. However, in this subsection, we will summarize some of their findings and discuss how different quantization schemes appear for the same theory.

First, depending on the choice of the boundary condition, we require to introduce a boundary term to the Eqn. 1.8 to ensure the action is stationary

$$S \rightarrow S' = S + S_{\partial}. \quad (1.25)$$

A cutoff is introduced at $z = \epsilon$ to capture the boundary effect at $z = 0$, and the computation is first performed in this UV cutoff. In the end, $\epsilon \rightarrow 0$ limit is taken. Now, stationarity of the action $\delta S' = 0$ puts a constraint on the variation of the boundary action,

$$\delta S_{\partial} = \int d^d x \epsilon^{-d+1} \partial_z \phi_{\epsilon} \delta \phi_{\epsilon}. \quad (1.26)$$

ϕ_{ϵ} is the value of the field at the cutoff boundary. Different choices of the boundary condition will yield different boundary actions. For example, for the Dirichlet boundary condition S is already stationary, whereas for the Neumann boundary condition, boundary action is

$$S_{\partial} = \int d^d x \epsilon^{-d+1} \phi_{\epsilon} \partial_z \phi_{\epsilon}. \quad (1.27)$$

Despite the differences in the details like the scaling of the bulk field near boundary, both Dirichlet and Neumann boundary conditions show similar exponent Δ_+ in the boundary correlators [37]. Similar techniques can be applied for different mixed boundary conditions. Careful tuning of a boundary action term is required to recover the Δ_- mode [37, 38].

1.4.4 Green's function

In the previous section, we reviewed why different boundary conditions require different actions. In this section, we make the connection of the boundary condition to the two quantization schemes that were briefly discussed in Sec. 1.4.2. In the process, we also review the computation of boundary Green's function using Witten's trick [17]. There is at least one other method of computing the Green's function, known as ϵ expansion [22] which we do not review in this manuscript.

Let us first compute the bulk to boundary correlator $K(z, \mathbf{x}; \mathbf{x}')$ and take the limit $z \rightarrow 0$ to find the boundary to boundary correlator $G(\mathbf{x}; \mathbf{x}')$. The first step to computing the correlation functions is to find the on-shell solution of the bulk field and find the asymptotic behavior of the fields at the boundary. Asymptotic behavior of the field near the boundary (at small z) is described by Eqn. 1.22 which is written in a slightly different form

$$\phi(z, \mathbf{x}) \sim \phi(\mathbf{x})z^{d-\Delta} + \mathcal{F}(\mathbf{x})z^\Delta, \quad (1.28)$$

where Δ can either of the roots in Eqn. 1.21, $\phi(\mathbf{x})$ is the source for a scalar operator $\mathcal{O}(\mathbf{x})$ of the boundary conformal field theory. From $\int d^d x \mathcal{O}(\mathbf{x}) \phi_0(\mathbf{x})$ one sees that $\mathcal{O}(\mathbf{x}) \rightarrow \mathcal{O}'(\mathbf{x}) = |\mathbf{x}'|^{2\Delta} \mathcal{O}(\mathbf{x}')$ so that $\mathcal{O}(\mathbf{x})$ has scale dimension Δ . In the second term, $\mathcal{F}(\mathbf{x})$ denotes the physical fluctuation in the presence of the source.

Green's equation can be written in the upper half plane coordinates

$$[-z^{d+1}\partial_z(z^{-d+1}\partial_z) + m^2L^2]K(z) = 0 \quad (1.29)$$

We first consider $\Delta = \Delta_+$ mode, with the choice of an ansatz solution

$$K(z) = C_{\Delta_+} z^{\Delta_+}. \quad (1.30)$$

Using isometries of the AdS space,

$$z \longrightarrow \frac{z}{z^2 + x^2}, \quad x \longrightarrow x - x'; \quad (1.31)$$

the solution can be written as

$$K(z, x; x') = C_{\Delta_+} \left(\frac{z}{z^2 + (x - x')^2} \right)^{\Delta_+} \quad (1.32)$$

Using the bulk to boundary correlator, an expression for the bulk field $\phi(z, \mathbf{x})$ can be obtained from the definition of Green's function. For a point source, the $\mathcal{F}(\mathbf{x})$ can be derived

$$\mathcal{F}(\mathbf{x}) = \pi^{-d/2} \frac{\Gamma(\Delta)}{\Gamma(\Delta - (d/2))} |\mathbf{x} - \mathbf{x}'|^{-2\Delta_+}. \quad (1.33)$$

It is shown in [39] that the two-point correlator of the boundary operators is

$$\langle \mathcal{O}(\mathbf{x}) \mathcal{O}(\mathbf{x}') \rangle \propto \mathcal{F}(\mathbf{x}). \quad (1.34)$$

It is then easy to verify the action required to obtain Δ_+ mode is

$$S = \frac{1}{2} \int d^d x dz z^{d+1-2\Delta} [(\partial_z \chi)^2 + (\partial_i \chi)^2], \quad (1.35)$$

where χ is a scaled version of the original field. The action above is convergent for $d/2 < \Delta < d/2 + 1$. For $\Delta > d/2 + 1$, a more intricate procedure is required to subtract the boundary divergences.

We will not review how to derive the action for the Δ_- mode. However, we make a note that the role of the $\phi(\mathbf{x})$ and $\mathcal{F}(\mathbf{x})$ is reversed. That is for Δ_- mode, $\mathcal{F}(\mathbf{x})$ acts as a source whereas $\phi(\mathbf{x})$ acts as fluctuation. Generator of the connected Green's function of the Δ_- theory can be derived from the Legendre transformation of the generators of the Δ_+ theory. The role switches due to the specific choices of the boundary condition.

Eqn. 1.33 can be considered as the expression for the scalar propagator in the Wick-rotated anti-de Sitter space (up to a normalization constant) in the continuum description. As the first test for lattice investigation of holography, a discretized version of the massive scalar field in hyperbolic space is investigated in chapter 2 where the central goal is to deduce

an equivalent expression in 2D and 3D hyperbolic space. We investigated the modification of this relation Eqn. 1.21 in the presence of curvature fluctuation in chapter 4. We will show that the discrete setting provides a perfect platform to investigate duality beyond the tree-level correspondence of the AdS space with boundary CFTs.

1.5 Construction of Hyperbolic Lattices

To develop numerical tools to investigate holography, we need to first construct a lattice on anti-de Sitter space. For flat Euclidean space \mathbb{R}^D , usually hypercubic lattices are used. Isometries of the flat space correspond to discrete translations along different axis and discrete rotations around different axes. Representing manifolds with curvature is not so trivial. In this thesis we will Wick rotate AdS space to obtain hyperbolic space. Hence in this section, we will discuss the construction of hyperbolic lattices.

In two dimensions, hyperbolic space \mathbb{H}^2 can be represented by the Euclidean Upper Half Plane (UHP). A length scale ℓ which is the radius of curvature of the hyperbolic space is associated with the constant negative curvature $K = \frac{-1}{\ell^2}$ of the hyperbolic space. UHP can represent hyperbolic space up to a Weyl factor

$$ds_{\text{UHP}}^2 = \ell^2 \frac{dx^2 + dy^2}{y^2}. \quad (1.36)$$

Using a Möbius transformation,

$$\omega = x + iy = -i(z + 1)/(z - 1), \quad |z| < 1 \quad (1.37)$$

the UHP plane can be converted into the Poincaré disk with metric

$$ds^2 = 4\ell^2 \frac{dzd\bar{z}}{(1 - |z|^2)^2}. \quad (1.38)$$

We will use the Poincaré disk representation to construct our lattice where position is given in complex polar coordinates $z = re^{i\theta}$. There are several other equivalent representations of hyperbolic space and each of those has their own advantages and usage. For example,

expressed in terms of radial geodesic coordinates ρ ,

$$ds^2 = d\rho^2 + \sinh^2(\rho)d\theta \quad (1.39)$$

For our lattice analysis, we exclusively used the Poincaré disk metric. The lattice points are generated inside the disk of unit radius. Triangle group symmetry is used to generate the lattice. A triangle group is a group that is realized through the reflection operation along the edges of the triangle. The triangle group can be realized as a group of motions for Euclidean plane, sphere, real projective plane and hyperbolic plane. For the hyperbolic lattice generation, Möbius triangles defined by three numbers (m, n, r) are used. The triplet determines the vertex angles and the sum of three vertex angles maintains the following inequality

$$\frac{\pi}{m} + \frac{\pi}{n} + \frac{\pi}{r} < \pi. \quad (1.40)$$

The reflections along different edges are considered as operations a, b, c . Two subsequent reflections along two adjacent edges with angle A are then equivalent to a rotation operation by an angle A . Identifying these rotation operations as α, β, γ , we have the following relations

$$a^2 = b^2 = c^2 = 1, \quad ab = \gamma, \quad bc = \alpha, \quad ca = \beta \quad (1.41)$$

For a lattice with triangle group $\Delta = (m, n, r)$, and rotation operations around the vertices α, β, γ denoted by angles $\pi/m, \pi/n, \pi/r$ respectively, it's straightforward to note that the following rule also holds

$$\alpha^{2m} = \beta^{2n} = \gamma^{2r} = 1. \quad (1.42)$$

We use these relations, Eqn. 1.41, 1.42, to generate the hyperbolic lattice. We worked on generating uniform lattices. In particular we are interested in tessellating the Poincaré disk with a $\{p, q\}$ tessellation. The pair indicates that a building block of p -gon is used with coordination number q for each vertex. For a $\{p, q\}$ tessellated Poincaré disk, the associated triangle group is $(m, n, r) = (2, p, q)$. The first step in the construction is to find the triangle called the fundamental triangle OA_1M . For the $\{p, q\}$ disk, we consider a p -gon $A_1A_2 \cdots A_p$ with equal edge length a positioned at the center of the Poincaré disk such that all points

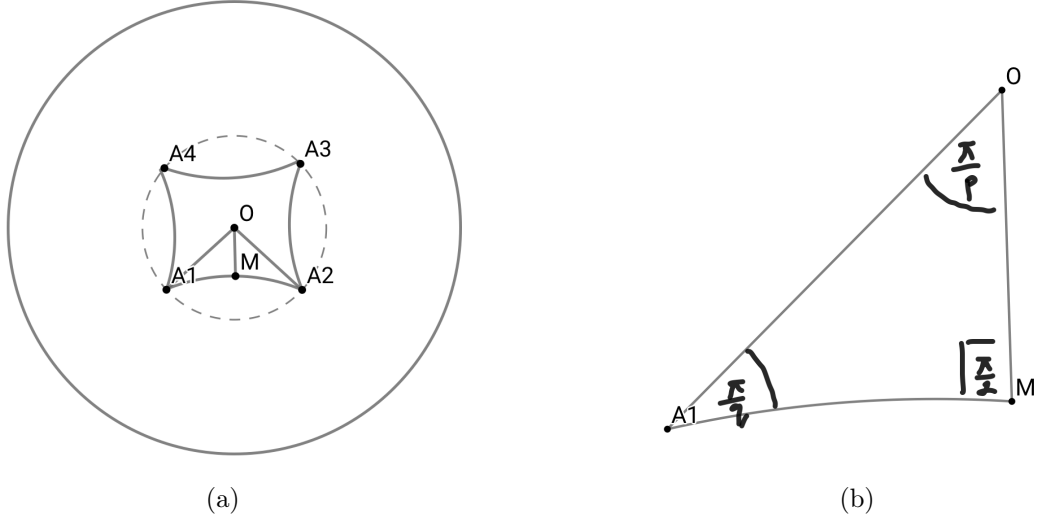


Figure 1.1: Construction of fundamental triangle $\triangle OA_1M$ for a $\{p, q\}$ tessellated disk. $p = 4$ is considered in the diagram.

are at the same distance from the origin O . Each edge of the p -gon creates an angle $2\pi/p$ at the center. Since the coordination number is q , any two adjacent edges create an angle $2\pi/q$. Next a perpendicular line OM is drawn and a triangle $\triangle OA_1M$ is created. $2p$ such triangles construct the p -gon $A_1A_2 \cdots A_p$. The angles of $\triangle OA_1M$ are $\pi/2$, π/p , and π/q . Now calculating the length $OA_1 = m$ and $OM = q$ will be sufficient to determine the coordinates of Q & M . The lengths are computed using the following identities

$$\sin\left(\frac{\pi}{p}\right) = \frac{\sinh(a/2)}{\sinh(m)} \quad (1.43)$$

$$\cos\left(\frac{\pi}{p}\right) = \frac{\tanh(q)}{\tanh(m)} \quad (1.44)$$

It seems that, like the lattice in the Euclidean space, the lattice spacing a in the negatively curved geometry can assume any value. However, an important distinction is that the edge length a in the uniform tessellated Poincaré disk is proportional to the geometry's intrinsic length scale (ℓ) $a \propto \ell$. The length scale ℓ appears in the Poincaré disk metric of the hyperbolic space in Eqn. 1.38 and thus the choice of the lattice spacing a in a uniform tessellation uniquely determines the scalar curvature $k = -\frac{1}{\ell^2}$ of the geometry. The area of

the fundamental triangle $\triangle OA_1M$ is then $A = |\pi - \frac{\pi}{2} - \frac{\pi}{p} - \frac{\pi}{q}| \ell^2 = |(1/2 - 1/p - 1/q)| \pi \ell^2$. Once the fundamental triangle has been created the symmetries are used to generate all the points in the lattice. Consider geometric operations S, T, U corresponding to the rotation relations α, β, γ respectively in Eqn. 1.42. In the Poincaré disk coordinate, this is equivalent to applying successively S and T operations on a point with complex coordinate z ,

$$S : z \rightarrow \frac{z - \sqrt{2 \cos(2\pi/q) - 1}}{z \sqrt{(2 \cos(2\pi/q) - 1) - 1}}, \quad (1.45)$$

whereas, $T = SU$ with

$$U : z \rightarrow e^{2\pi i/q} z \quad (1.46)$$

Starting with any vertex on the disk, application of S introduces a new vertex in the lattice which corresponds to a point in a new layer. Then, the application of T generates all the neighboring q points of the vertex. The process is repeated recursively and the hyperbolic lattice can be generated.

1.6 Lattice simulation

In Monte Carlo simulation one constructs a stochastic approximation to the path integrals that represent the Green's functions or correlation functions for some quantum field theory. For a model depending on a field $\phi(x)$ the expectation value of some observable or correlator $\mathcal{O}(\phi)$ can be computed from the expression:

$$\langle \mathcal{O} \rangle = \frac{1}{Z} \int D\phi e^{-S(\phi)} \quad (1.47)$$

Here $S(\phi)$ is called the action and $Z = \int D\phi e^{-S}$ is the partition function. As long as S is real this resembles a probability distribution and hence can be sampled stochastically according to that distribution. If the theory is discretized on a lattice the field $\phi(x) \rightarrow \phi_i$ can be indexed by a simple integer i which runs over all the local degrees of freedom. In some cases these degrees of freedom are simple spins which can take only a restricted set of values eg for Ising spins $\phi_i \rightarrow \sigma_i$ with $\sigma_i = \pm 1$. In this case the integrals at each lattice

site $\int d\phi_i$ are to be replaced by simple summations \sum_i over the values of the spin at that site. It should be noted that even in this limit the number of terms that arise in computing say the partition function is still enormous eg for a 10×10 2d lattice there are 2^{100} different configurations of the spins.

Fortunately, for the accurate estimation of the average value of observables, we do not need to generate all possible configurations as most configurations contribute little to the sum as they are damped off exponentially by the factor of e^{-S} . Rather a representative set of configurations that dominate Z – called an “ensemble” – can be generated using a stochastic algorithm and the average quantities can be computed just using these sample configurations. This is the basic idea of Monte Carlo simulation. In practice one starts from some initial configuration and generates another via a series of local “moves” or changes to the current configuration.

Only a few conditions need to be satisfied for a satisfactory Monte Carlo algorithm. First the moves must be ergodic which is simply the requirement that repeated application of these moves must be sufficient to move from any one point to any other point in the configuration space. Second, the probability that a move is accepted or not (the stochastic element) depends only on the change in the Boltzmann weight $e^{-\Delta S}$. Another important condition that is required is that the Boltzmann weights $W_r = e^{-S_r}$ are eigenvectors with unit eigenvalue of the transition matrix $T_{r,s}$. That is

$$\sum_s T_{r,s} W_s = W_r \tag{1.48}$$

with $T_{r,s}$ denoting the transition probability from state s to state r . T maintains the normalization condition $\sum_r W_{r,s} = 1$. In practice, a stricter condition named “detailed balanced” can be imposed which is

$$T_{r,s} W_s = T_{s,r} W_r \tag{1.49}$$

Using the Boltzmann weight $W_r = e^{-\beta S_r}$ with β a coupling constant the above equation reduces to

$$T_{r,s} \exp^{-\beta S_r} = T_{s,r} \exp^{-\beta S_s} . \tag{1.50}$$

Here, S_i denotes the action of the configuration i . In Euclidean space the action is often thought of as an energy E . The transition probability defined above is a composite object, and can be expressed as a product of the a priori probability $P_{r,s}$ and the acceptance probability $A^{r,s}$. The a priori probability is the probability of choosing the move that takes an state s to r in the configuration space. Hence, the above equation reads

$$P_{r,s}A^{r,s} \exp^{-\beta E_r} = P_{s,r}A_{s,r} \exp^{-\beta E_s} . \quad (1.51)$$

This equation is known as the detailed balance equation in the physics literature. Notice that Monte Carlo algorithms are quite generic and apply equally well in both flat space and hyperbolic space.

1.6.1 Review of the Metropolis Algorithm

Perhaps the most well known Monte Carlo algorithm is the Metropolis algorithm [40, 41].

The Metropolis-Hastings algorithm works by generating a sequence of sample configurations (ν) with probability density $f(\nu)$. One constructs the algorithm so that $f(\nu)$ is proportional to the target distribution $W(\nu) = e^{-S(\nu)}$. The process is a Markov process [42] and the configuration generated at a certain Monte Carlo time t depends only the state attained in the previous step $t - 1$ *. However, the new configuration can either be accepted or rejected depending on the values of $f(x)$ for the current configuration and proposed configuration. In the proposed configuration is accepted, the new configuration is used as the initial state for the next iteration. Otherwise, current state is used as the initial state.

The Metropolis algorithm provides a recipe to generate a Markov chain with a target probability distribution function with the help of a random number generator (RNG). In practice, pseudo-number generators are used for our simulation. We used the Mersenne Twister pseudo RNG of the C++ library. We tested our results against results obtained from `ran3()` of the text “Numerical Recipes” [43].

Given a configuration ν , the metropolis algorithm proposes a new configuration μ with

*In the discretized state space the Markov process is called a Markov chain.

a priori probabilities $p(\mu, \nu)$. New configuration is accepted with a probability

$$A^{r,s} = \min\left(1, \frac{W_r}{W_s}\right). \quad (1.52)$$

Thus

$$A^{r,s} = \Theta(E_s - E_r) + \exp(-\beta(E_r - E_s))\Theta(E_r - E_s) \quad (1.53)$$

where, Θ is the step function. Note that at each iteration for newly generated configuration ν , the total energy E_ν for the configuration is not needed. Rather the algorithm only requires knowledge of the energy difference between the two configurations which can be efficiently computed via a local operation. For example, for the computation of the observables for an Ising spin model, the Hamiltonian couples only nearest neighbor spins and so the change in the energy under a single "spin flip" requires only the computation of q terms where q is the local coordination number of the vertex in question. In practice we choose the spin to be updated at random although sequential update of spins is also possible [42]. It's important to mention that for the $E_r > E_s$ case in Eqn. 1.53, another random number x is generated in between 0 to 1, and the move is accepted only if $x < \exp(-\beta(E_r - E_s))$ [†].

Straightforward implementation of the metropolis algorithm is its greatest advantage. However, near criticality due to a long autocorrelation time, a phenomenon called "critical slowing down" occurs and it is advantageous to use other algorithms which change the spin configuration globally. Critical slowing down just means that successive configurations are statistically correlated and one must apply the Metropolis algorithm many times to obtain a decorrelated configuration to use in the Monte Carlo averaging. One algorithm that provides a much better performance near criticality is the cluster Monte Carlo algorithm which we discuss in the following section.

1.6.2 Review of the Cluster Algorithm

We used cluster Monte Carlo algorithm for the low temperature simulation of the Ising spin model on hyperbolic lattices which is discussed in chapter 3. This algorithm was introduced

[†]In practice, we used at least two random number generators for each of our studies to ensure that the pseudo-number generator works without any flaw

by Wolff in the context of 2D $O(N)$ σ model [44]. In the original paper, the algorithm was implemented for Ising model ($N = 1$), x-y model ($N = 2$) and Heisenberg model ($N = 3$). Due to much smaller autocorrelation times compared to the metropolis algorithm, the Wolff cluster algorithm shows improved performance near criticality in many statistical models.

The model was inspired by percolation theory and the previously developed percolation based theory Swendsen and Wang (SW) algorithm [45]. Even though SW algorithm immensely improved correlation time in the Potts model, the model suffered negatively for x-y model. This inspired researchers to look for improved cluster algorithms. Single cluster flip algorithm is one such improved algorithm which has since then been applied to many models including medium-range [46] and long-range spin models [47], anisotropic spin systems [48], XY model [49] since it's inception. We outline the steps to implement the algorithm below.

1. A lattice site i is randomly selected and the state of the spin is noted f .
2. Selected spin site is added to a cluster list C .
3. Next, a list of the neighboring sites $n(i)$ of selected lattice site i is made.
4. Iteratively the state of the spin in the list n is checked, and if the neighboring lattice site $n(i)$ has the same state to that of site i , the spin is added to the cluster C with probability p . Once the check is completed for $n(i)$, that spin is deleted from the list n . If the spin $n(i)$ is added to the cluster, then we replace i with $n(i)$: $i \leftarrow n(i)$.
5. Step 3 and 4 are repeated until the list $n(i)$ is exhausted.

Now, we will deduce the acceptance probability in the cluster Monte Carlo for a simulation with N_d spins. Assume that a cluster with n_c spins with state f is formed using the steps above. Also, assume that there are n_f spins connected to this cluster with the same state but due to the probabilistic nature of adding spins to the cluster, were not added to it. The probability of n_f spins not being added to cluster is $(1 - p)^{n_f}$. Thus, the a priori probability for a configuration to move from state ν to μ is

$$P_{\mu,\nu} = \frac{1}{N_d} p^{n_c} (1 - p)^{n_f}. \quad (1.54)$$

After flipping all the spins in the cluster in the ν configuration we will obtain the configuration

μ . The same cluster of n_c spins has now a different state g and if the number of spins with state g that were not added to the cluster is n_g , we can write an expression for the a priori probability of transition from μ to ν .

$$P_{\nu,\mu} = \frac{1}{N_d} p^{n_c} (1-p)^{n_g}. \quad (1.55)$$

Now if the Ising Hamiltonian is

$$H = -\beta \sum_{\langle ij \rangle} s_i s_j, \quad (1.56)$$

then the ratio of Boltzmann factors can be written as

$$\frac{W_\nu}{W_\mu} = \frac{\exp(-\beta(n_f - n_g))}{\exp(-\beta(n_g - n_f))} = \frac{\exp(-2\beta n_f)}{\exp(-2\beta n_g)} \quad (1.57)$$

Requiring detailed balance Eqn. 1.51 the acceptance probability is given by

$$\tilde{P}_{\mu,\nu} = \min \left\{ 1, \left[\frac{e^{-2\beta}}{1-p} \right]^{n_f} \left[\frac{1-p}{e^{-2\beta}} \right]^{n_g} \right\} \quad (1.58)$$

It's evident that the choice of $p = p^* = 1 - \exp(-2\beta)$ yields a rejection free algorithm and thus the whole cluster can be flipped at once. Unlike the metropolis algorithm, due to the choice of $p = p^*$, once the cluster is created it is flipped with certainty. Notice this procedure updates many spins at a time - it is global update. This is the reason it can beat any local algorithm which tries to update a single spin.

1.6.3 Monte Carlo simulation of dynamical lattice geometry

In this thesis we are also interested in models in which the tessellation of hyperbolic space is allowed to fluctuate. This represents the effects of quantum fluctuations in the (bulk) geometry. It is a topic that is hard to treat with analytic calculations but crucial to a proof that the AdS/CFT holds away from the limit of classical gravity. It hence forms an ideal target for numerical work.

To do this we need to develop Monte Carlo algorithms that are capable of sampling a

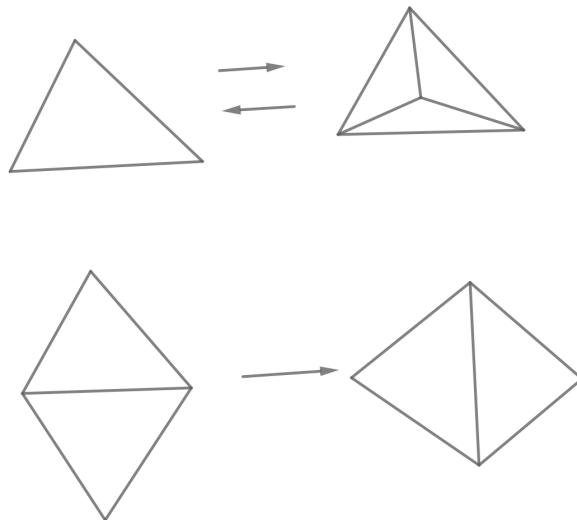


Figure 1.2: Ergodic moves in the class of two-dimensional triangulation. Node insertion and deletion (top), and link flip (bottom).

sum over many different lattice geometries. Again we seek local geometry moves that can be implemented in a manner that respects detailed balance and allows us to construct a Markov chain in the space of tessellated (or here triangulated) geometries. Fortunately this problem was solved many years ago in efforts to study discrete quantum gravity where the approach is called Euclidean dynamical triangulation. [50, 51]. A variation which allows for a well defined Wick rotation back to Minkowski space is called causal dynamical triangulation [52, 53][‡]. Scalar fields on fluctuating geometries are discussed in chapter 4. To generate an ensemble of simplicial manifolds, a set of local moves called “Pachner moves” are used. Any two triangulations of fixed topology are related through a sequence of Pachner moves. In two-dimensions, the Pachner moves involve inserting a node in the triangle, deleting a three-fold coordinated node, and performing a link flip. The set of moves are ergodic. See Fig. 1.2.

It is straightforward to use these moves to devise a simple Monte Carlo procedure which samples the sum over lattice geometries according to the discrete action described above. In two dimensions this sum over random lattices is known to reproduce the effects of integrating over metrics modulo diffeomorphisms in the continuum limit.

[‡]The author of this thesis has also been involved in this work with a recent paper exploring the phase diagram of the theory in four dimensions. However, this work is not included in this thesis to keep the latter tightly focused on holographic aspects of gravity.

The moves are identified as moves associated with the removal of a given subsimplex and hence can be indexed with an integer i , depending on the sub-simplex type. Thus node insertion is associated with a triangle ($i = 2$), node deletion is associated with a vertex ($i = 0$) and link flip is associated with link ($i = 1$). Node deletion can be considered as the inverse operation of the node insertion operation, and link flip operation is its own inverse. The order of sub-simplex ($O(i)$) is identified as the coordination number of the subsimplex. For example, any link belongs to two triangles in 2D and thus $O(1) = 2$ for any link in the 2D triangulation. This can all be generalized to d dimensions – there $d + 1$ possible moves and each move of type i can be inverted through a dual $d - i$ move.

Now we deduce a correct detailed balanced equation relating the local moves described above. Rewriting the detailed balance equation in Eqn. 1.51 with slightly different notation

$$W_\nu T_{\mu,\nu}^i = W_\mu T_{\nu,\mu}^{d-i}. \quad (1.59)$$

where T is labeled by the move type i .

Now the a priori probabilities P can be expressed as a product of probabilities of choosing the initial state and final states. Implementation of any Pachner move yields a unique final state from a given initial state. Detailed balance then dictates:

$$W_\mu P_{\mu,\nu}^i A_{\mu,\nu}^i = W_\nu P_{\nu,\mu}^{d-i} A_{\nu,\mu}^{d-i}. \quad (1.60)$$

Let us pick at random a simplex with probability $\frac{1}{N_d}$ where N_d is the number of d -simplices. For a type i move there are $\frac{1}{\binom{d+1}{i+1}}$ choices of i -simplex within that simplex. Thus the probability of finding this particular subsimplex to delete is

$$\frac{1}{d+1} \frac{O(i)}{N_d(\nu)} \frac{1}{\binom{d+1}{i+1}}. \quad (1.61)$$

where $O(i)$ is the number of simplices containing the given i -simplex. Likewise the inverse move has an a priori probability of

$$\frac{1}{d+1} \frac{O(d-i)}{N_d(\mu)} \frac{1}{\binom{d+1}{d-i+1}}. \quad (1.62)$$

This implies that the ratio of a priori probabilities for the move and its inverse is

$$\frac{N_d(\mu)}{N_d(\nu)} \frac{O(i)}{O(d-i)} \frac{\binom{d+1}{d-i+1}}{\binom{d+1}{i+1}}. \quad (1.63)$$

However, due to the nature of the Pachnar moves and the need to stay within the allowed set of combinatorial triangulations it's easy to verify that

$$\frac{O(i)}{O(d-i)} \frac{\binom{d+1}{d-i+1}}{\binom{d+1}{i+1}} = 1$$

Thus detailed balance for such moves then requires

$$e^{-S(\mu)} \frac{1}{N_d(\nu)} A_{\mu,\nu}^i = e^{-S(\nu)} \frac{1}{N_d(\mu)} A_{\nu,\mu}^{d-i}, \quad (1.64)$$

which reduces to the following equation for the acceptance probability of move i to obtain a state μ from an initial state ν

$$A_{\mu,\nu}^i = \frac{1}{1 + \left(1 + \frac{(2i-d)}{N_d(\mu)}\right) e^{S(\nu)-S(\mu)}} \quad (1.65)$$

This is the required expression of the acceptance probability to generate simplicial manifolds in our lattice simulation.

In principle, the simulation of a random triangulated disk can be obtained from the simulation of a sphere. One merely imagines cutting one vertex and its neighbour triangles out of the sphere. The length of the boundary of the resultant disk is then given by the number of neighbors of this special vertex. Simulations of the disk can be obtained by simulating a sphere containing one special “marked node” [54]. This node is never deleted and the action of the model can be modified to contain a term which fixes the number of its neighbors at whatever target disk boundary is needed. To generate disks that are asymptotically hyperbolic one must fix the connectivity of not just the special node (so that the number of vertices in the boundary is a fixed fraction of the total number of vertices in the disk) but also the connectivity of the boundary points to its nearest neighbours remain

fixed so that they resemble the known connectivity of a regular tessellation of hyperbolic space. This ensures that even after fluctuations of the bulk geometry the latter approaches a tessellation of hyperbolic space asymptotically. It turns out that this constraint is then sufficient to fix the average curvature of the disk to a constant negative value.

Chapter 2

Massive scalar fields on hyperbolic space

2.1 Introduction

In this chapter, we compute boundary correlation functions for massive scalar fields on tessellations of two- and three-dimensional hyperbolic geometries. We present evidence that the continuum relation between the scalar bulk mass and the scaling dimension associated with boundary-to-boundary correlation functions survives the truncation of approximating the continuum hyperbolic space with a lattice.

As discussed in the previous chapter in section 1.3, the posited duality can be expressed as an equality between the generating functional for a conformal field theory, and a restricted path integral over fields propagating in AdS:

$$Z_{\text{CFT}_d}[J(x)] = \int \mathcal{D}\phi \delta(\phi_0(x) - J(x)) e^{iS_{\text{AdS}_{d+1}}}. \quad (2.1)$$

The boundary values of the fields, ϕ_0 , do not fluctuate, as they are equivalent to classical sources on the CFT side of the duality. The earliest checks establishing the dictionary for this duality were performed by studying free, massive scalar fields, propagating on pure anti-de Sitter space [17, 19]. These established that the boundary-boundary two-point correlation function of such fields has a power law dependence on the boundary separation, where the

magnitude of the scaling exponent, Δ , is related to the bulk scalar mass, m_0 , via the relation

$$\Delta_{\pm} = \frac{d}{2} \pm \sqrt{\frac{d^2}{4} + m_0^2 \ell^2}, \quad (2.2)$$

where ℓ is the scalar curvature of the AdS space. The two choices for the scaling dimension are related to different treatments of the boundary action [20]. The Δ_- branch of solutions (which can saturate the unitarity bound, $\Delta = d/2 - 1$) requires tuning to be accessible in the absence of supersymmetry.

In this chapter, we put massive lattice scalar field theory on finite tessellations of negative-curvature spaces as test bed to determine which aspects of the AdS/CFT correspondence survive the latticization. Finite-volume and discreteness create both ultra-violet (UV) and infrared (IR) cutoffs, potentially creating both a gap in the spectrum and a limited penetration depth from the boundary into the bulk spacetime. Finite lattice spacing regulates the UV behavior of the correlators. Despite these artifacts, we show that such lattice theories do exhibit a sizable regime of scaling behavior, with this “conformal window” increasing with total lattice volume.

We specifically construct tessellations of both two- and three-dimensional hyperbolic spaces, construct scalar lattice actions, and compute the lattice Green’s functions to study the boundary-to-boundary correlators. We find general agreement with Eq. (2.2) in the large volume extrapolation.

Prior work has focused on the bulk behavior of spin models on fixed hyperbolic lattices and on using thermodynamic observables to map the phase diagram [55–58]. Here, the focus is on the structure of the boundary theory and, since free scalar fields are employed, the matter sector can be computed exactly including the boundary-boundary correlation function. This setup allows for a direct test of the continuum holographic behavior.

Reference [59] performed a investigation of the bulk and boundary scalar field propagators in two-dimensional hyperbolic space using lattice techniques. In this chapter, we extended the discussion to other two dimensional tessellations and in three dimensional tessellation of hyperbolic space. Even though we present some bulk results in our study, our primary focus has been the computation of boundary correlators.

The organization of this chapter is as follows. In Section 2.2 we describe the class of tessellations we use in two dimensions and the construction of the discrete Laplacian operator needed to study the boundary correlation functions. In Section 2.3, few other examples of two dimensional hyperbolic lattices are presented. In Section 2.4 we extend these calculations to three-dimensional hyperbolic geometry. Finally, we summarise our results in Section 2.5.

2.2 Two-dimensional hyperbolic geometry

Regular tessellations of the two-dimensional hyperbolic plane can be labeled by their Schläfli symbol, $\{p, q\}$, which denotes a tessellation by p -gons with the connectivity, q , being the number of p -gons meeting at a vertex. In order to generate a negative curvature space, the tessellation must satisfy $(p - 2)(q - 2) > 4$.

We construct our tessellations by first defining the geometry of a *fundamental domain triangle* from its three interior angles. For regular $\{p, q\}$ tessellations, these angles are $\pi/2$, π/p , and π/q . In the Poincaré disk model, geodesics are circular arcs (or lines) orthogonal to the disk boundary. Circle inversions in the model equate to reflections in the hyperbolic plane and using this property, we recursively reflect this triangle in its geodesic edges to fill the plane with copies of the fundamental region. Each copy corresponds to a symmetry of the tiling. Thus reflections generated by the sides of the triangles form a symmetry group, which is a $(2, p, q)$ triangle group for the $\{p, q\}$ tessellation. The regular tessellation forms a subset of edges of this group. For a discussion on the triangle group and the generation of the points of the fundamental triangle see Section 1.5.

It is quite straightforward to build the Laplacian matrix using the connectivity information of the vertices of the tessellated disk. In this way, the lattice is stored solely in terms of its adjacency information. The lattice is then composed of flat equilateral triangles with straight edges, all of which are the same length throughout the lattice.

A typical example of the lattice is shown in Fig. 2.1, where the tessellation is shown in the Poincaré disk model and corresponds to the $\{p, q\}$ combination $\{3, 7\}$. An image of the boundary connectivity can be seen in Fig. 2.2. We see the boundary has all manner of vertex connectivity, some even with seven-fold coordination.

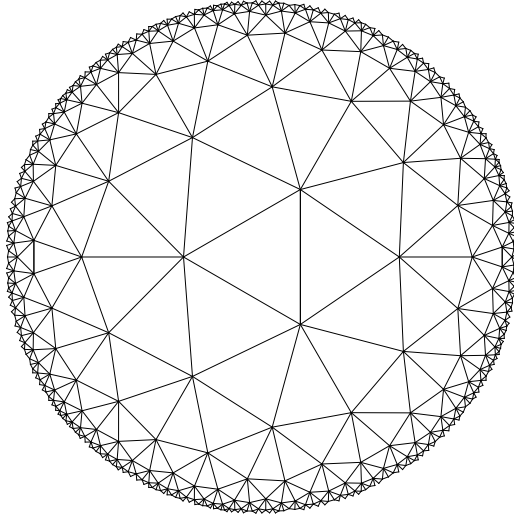


Figure 2.1: $\{3,7\}$ tessellation in the Poincaré Disk model of the hyperbolic plane.

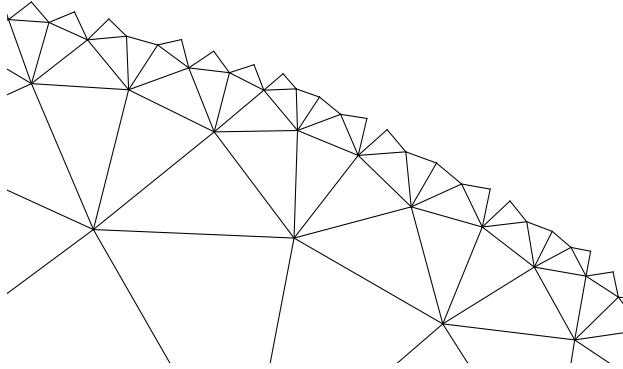


Figure 2.2: A zoom-in of the boundary of the Poincaré disk shown in Fig. 2.1.

In the continuum, the action for a massive scalar field in two Euclidean spacetime dimensions is given by

$$S_{\text{con.}} = \frac{1}{2} \int d^2x \sqrt{g} (\partial_\mu \phi \partial^\mu \phi + m_0^2 \phi^2), \quad (2.3)$$

where m_0 is the bare mass, and $d^2x \sqrt{g}$ is the amount of volume associated with each point in spacetime. The corresponding discrete action on a lattice of p -gons is then

$$S = \frac{1}{2} \sum_{\langle xy \rangle} p_{xy} V_e \frac{(\phi_x - \phi_y)^2}{a^2} + \frac{1}{2} \sum_x n_x m_0^2 V_v \phi_x^2. \quad (2.4)$$

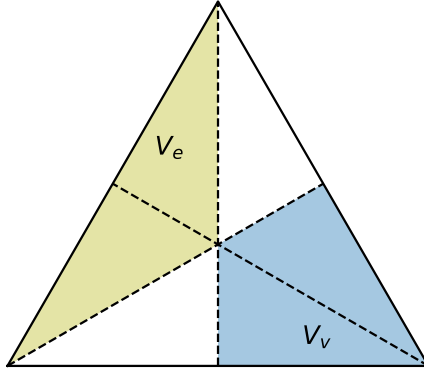


Figure 2.3: The volume, V_e , associated with an edge is shown in yellow, and the volume, V_v , associated with a vertex is shown in blue. In two dimensions, since each p -gon has the same number of vertices as edges, these volumes are always the same (in this case they are both $1/3$ of the area of the total triangle).

Here V_e denotes the volume of the lattice associated with an edge, V_v denotes the volume associated with a vertex, a denotes the lattice spacing, p_{xy} denotes the number of p -gons which share an edge (in the case of an infinite lattice this is always two), and n_x is the number of p -gons around a vertex. For two-dimensional p -gons,

$$V_v = V_e = \frac{a^2}{4} \cot \frac{\pi}{p}, \quad (2.5)$$

and an illustration of the volumes associated with links and edges are shown in Fig. 2.3. This definition of the mass and kinetic weights ensures that the sum of the weights gives the total volume of the lattice, *i.e.* $\sum_{\langle xy \rangle} p_{xy} V_e = \sum_x n_x V_v = A_p N_p$, where A_p is the area of a p -gon, and N_p is the number of p -gons. $\sum_{\langle xy \rangle}$ denotes a sum over all nearest-neighbor vertices, and \sum_x is over all vertices. We can write the action from Eq. (2.4) as

$$S = \sum_{x,y} \phi_x L_{xy} \phi_y \quad (2.6)$$

with L_{xy} given by

$$L_{xy} = -\frac{p_{xy}}{2} \delta_{x,y+\hat{1}} + \frac{1}{2} \left(\sum_z p_{xz} \delta_{z,x+\hat{1}} + m_0^2 n_x \right) \delta_{x,y}. \quad (2.7)$$

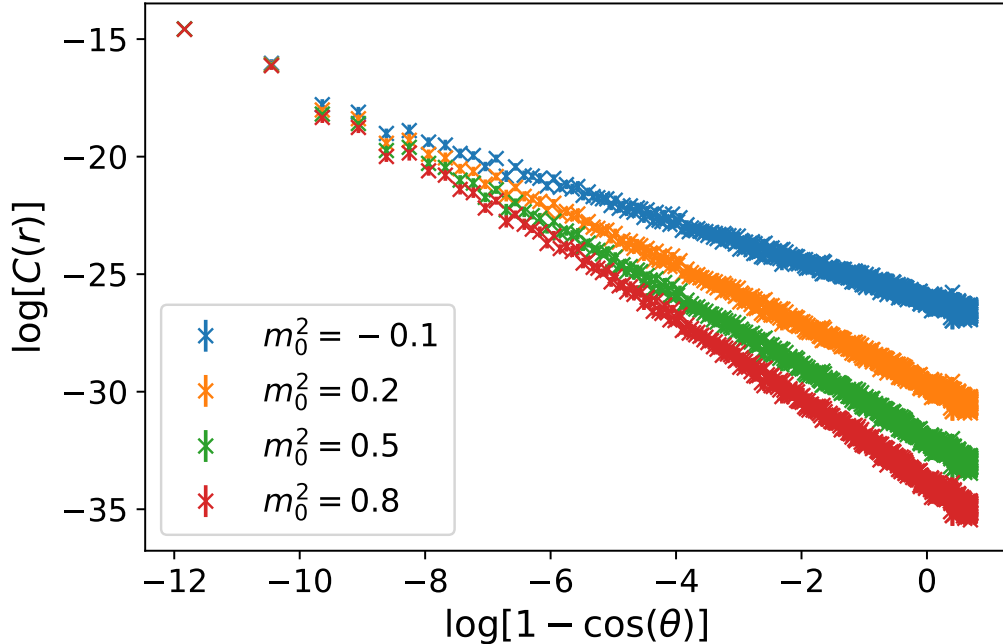


Figure 2.4: Four different correlators corresponding to different squared bare masses are plotted in log-log coordinates for the case of a 13-layer lattice, with the squared boundary mass set to $M^2 = 1000$. The masses here from top to bottom are $m_0^2 = -0.1, 0.2, 0.5$, and 0.8 .

In practice we can rescale the scalar field so that the kinetic term has unit weight.

We set the edge length, a , to one, throughout. In the bulk, for a two-dimensional lattice, $p_{xy} = 2$ and $n_x = q$, but these values change for edges and points on the boundary. We note that boundary terms must be added to appropriately approximate the infinite volume AdS/CFT correspondence, in which fields at the AdS boundary are not permitted to fluctuate. To simulate this, we include a large scalar mass, M , only on the boundary vertices and extrapolate fits as $M \rightarrow \infty$. The average boundary correlation function (propagator) is then computed from

$$C(r) = \frac{\sum_{x,y} L_{xy}^{-1} \delta_{r,d(x,y)}}{\sum_{x,y} \delta_{r,d(x,y)}}, \quad (2.8)$$

where $d(x, y)$ is the distance measured between boundary sites x and y along the boundary. Looking at this quantity, we observe a power law, $C(r) \sim r^{-2\Delta}$, as can be seen in Fig. 2.4, which shows the correlator for four different masses on a $\{3, 7\}$ tessellation with 13 layers containing a total of $N = 2244$ vertices.

To fit the data, we take into account the fact that at finite tessellation depth, the boundary is of finite size which provides an IR cutoff effect. The modified form of the correlators on the circular compact geometry is known [60], with the relation between flat space correlators and those on the circle corresponding to a conformal mapping from the Poincaré disk to the half-plane, and an additional overall factor associated with the finite size boundary metric [61]. The overall effect is a calculable deviation of the two-point correlation function from straight power law at distances comparable to the perimeter of the circle:

$$C(r) \propto \frac{1}{\left|1 - \cos\left(\pi \frac{r}{r_{\max}}\right)\right|^\Delta} \stackrel{r \ll r_{\max}}{\propto} \frac{1}{|r|^{2\Delta}} \quad (2.9)$$

where r is the distance along the boundary, and r_{\max} is the distance along the boundary between antipodal points.

We thus fit the correlator using the form,

$$\log C(r) = -\Delta \log(1 - \cos(\theta)) + k, \quad (2.10)$$

with k and Δ as fit parameters, and $\theta = \pi r/r_{\max}$. The error bars are found from using the jackknife method over a subset of the boundary points. In addition to the average over boundary points, we also find a non-negligible systematic error from deciding the fit range. We calculate this error by repeating the analysis for all different possible reasonable fit ranges and re-sample from these results. We add the errors found from this method in quadrature to the jackknife error, and find that the systematic part is by far the largest contribution to the error.

We check to see if the power, Δ , obeys a similar relation to Eq. (2.2), and fit Δ to the form,

$$\Delta = A + \sqrt{A^2 + Bm_0^2}, \quad (2.11)$$

where A and B are fit parameters. The solid curve in Fig. 2.5 indicates the best fit (least squares minimum) to Eq. (2.11) for a fixed system size and boundary mass. We expect A

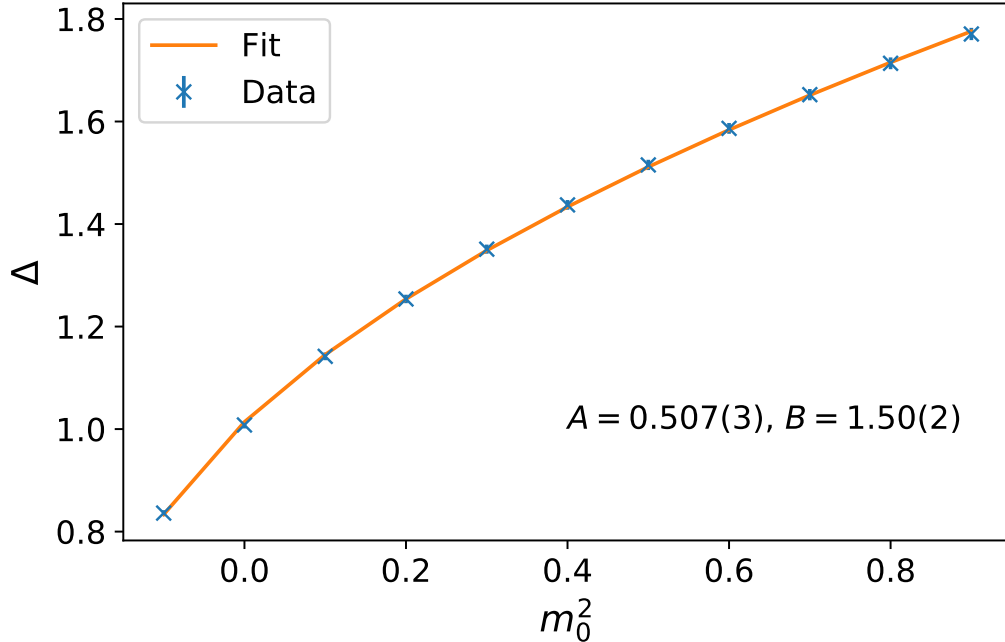


Figure 2.5: The power law obtained from fitting the correlation function in Eq. (2.8) versus the squared bare mass. Here we show the result for a 13-layer lattice with squared boundary mass, $M^2 = 1000$. We find good qualitative agreement with Eq. (2.2).

to correspond to half the effective boundary dimension, $d/2$, and B to an effective squared radius of curvature. We extract the parameters A and B from fits across a range of boundary masses and of system volumes.

Using the various system sizes and boundary masses, we extrapolate the parameters A and B to their values at the infinite-boundary mass, and infinite-system size limit. In practice, we first extrapolate in system size at fixed boundary mass, and then extrapolate to infinite boundary mass at infinite volume.

In the infinite-volume extrapolation, we identify the regime in which the fit parameters, A and B , scale approximately linearly with the inverse boundary size, N_{bound} . In other words,

$$A = \frac{C}{N_{bound}} + A_\infty, \quad B = \frac{D}{N_{bound}} + B_\infty, \quad (2.12)$$

where C , D , A_∞ and B_∞ are fit parameters. An example of the large-volume data is shown in Fig. 2.6.

Once we have A_∞ and B_∞ for each boundary mass, we extrapolate those values to infinite

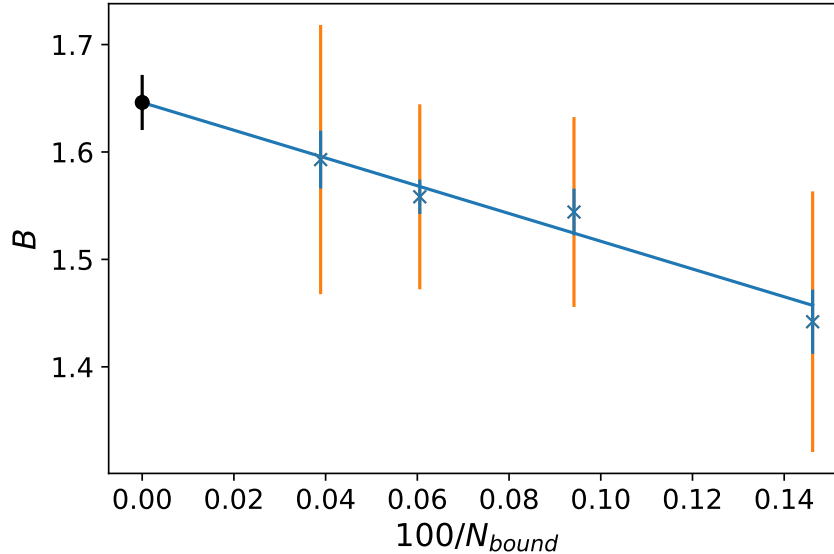


Figure 2.6: The large-volume extrapolation of the B parameter as a function of the inverse volume of the boundary, for a boundary mass of $M^2 = 1000$. We have re-scaled by 100 triangles to remove clutter on the x -axis. We fit a line to this data to extract the B parameter at infinite volume, B_∞ . We have included the systematic error, due to the choice of the fit range, in orange.

boundary mass. Again we look for a window of masses in which the parameters scale linearly in the inverse squared boundary mass, such that

$$A_\infty = \frac{E}{M^2} + A_\infty(M_\infty) \quad (2.13)$$

$$B_\infty = \frac{F}{M^2} + B_\infty(M_\infty), \quad (2.14)$$

where E , F , $A_\infty(M_\infty)$, and $B_\infty(M_\infty)$ are fit parameters. During our investigation we found we can take the boundary mass sufficiently large such that the extrapolation in large boundary mass is negligible. We find $A_\infty \simeq 0.505(7)$ and $B_\infty \simeq 1.65(3)$. In the next section we repeat this analysis for the case of $\{4, 5\}$ and $\{3, 8\}$ tessellations and again find an effective boundary dimension close to unity but a different value for B reflecting the differing local curvature.

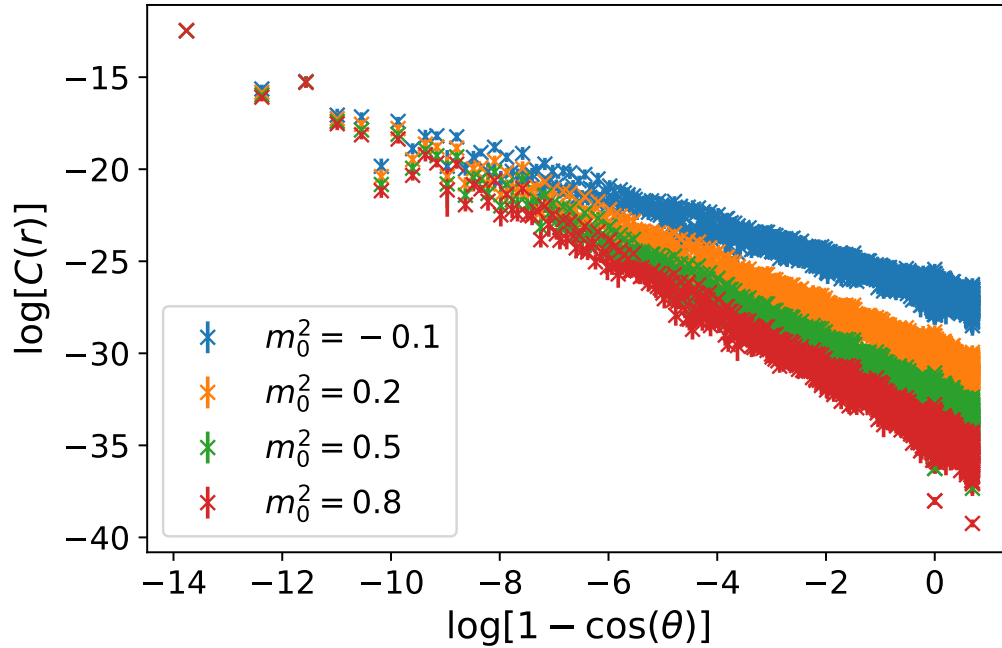


Figure 2.7: The boundary two-point correlator is plotted in log-log coordinates for the lattice $\{p, q\} = \{4, 5\}$. Here four bulk masses are shown for the values of $m_0^2 = -0.1, 0.2, 0.5,$ and 0.8 , with a boundary mass of $M^2 = 500$. The lattice is comprised of eight layers of squares.

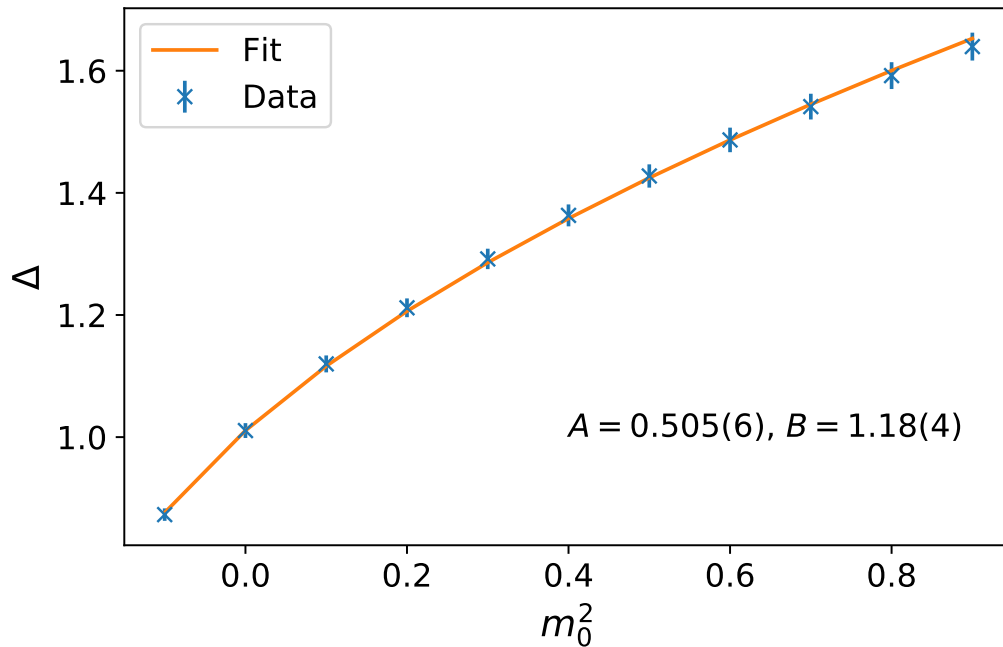


Figure 2.8: The power-law extracted from the correlator data for the $\{p, q\} = \{4, 5\}$ lattice. This data is for a eight layer lattice with a boundary mass of $M^2 = 500$. The fit parameters for this fit are quoted inside the figure.

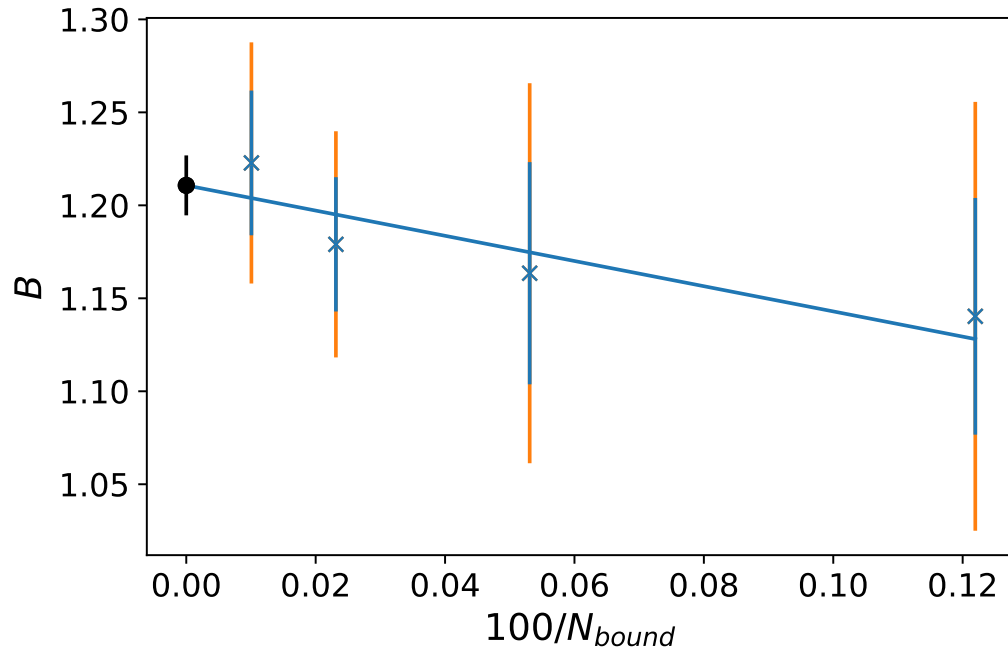


Figure 2.9: The finite-size scaling for the B fit parameter versus the inverse boundary size. Here we re-scaled the x -axis by 100 squares to declutter the axis labels. This fit is for a boundary mass of $M^2 = 500$.

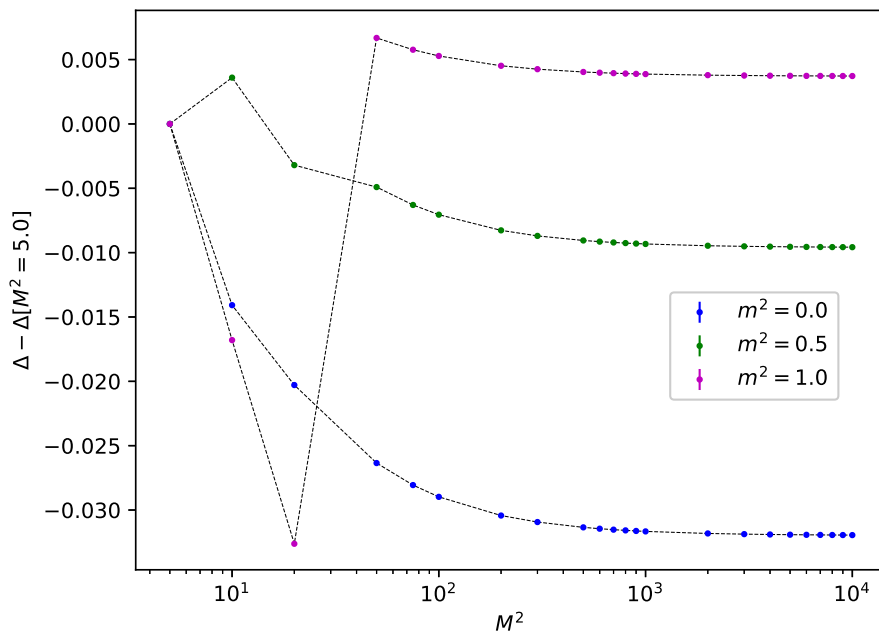


Figure 2.10: Boundary mass (M^2) dependence of the fit parameter Δ in the two point function for a 10 layer lattice in the $\{3, 8\}$ geometry. Error bars are of the order 10^{-4} or smaller and not visible in the figure.

2.3 Other two-dimensional tessellations

To ensure the fit parameters obtained in the $\{3, 7\}$ study were not trivial, we also considered a $\{p, q\} = \{4, 5\}$ and $\{p, q\} = \{3, 8\}$ lattice, and repeated the analysis. This should give the same result for A , since the boundary is still one-dimensional, however the curvature of the lattice is different from the $\{3, 7\}$ case, and so we would expect a different result for the B fit parameter. In Fig. 2.7 we see an example of the boundary-to-boundary two-point correlator for four different masses for the $\{4, 5\}$ tessellation.

There is more noise than in the $\{3, 7\}$ case, perhaps due to the more coarse nature of the tessellation using squares instead of triangles; however, the power-law behavior is still apparent. We used binning in distance r along boundary or equivalently in θ in the radial coordinates to reduce the fluctuation in the correlator data before performing the fits. This essentially reduces the fluctuation of the radial distance of the boundary points in the Poincaré disk picture while keeping the average radius of curvature unchanged, thus providing a better handle to predict the same continuum result.

Table 2.1: $\{3, 8\}$ tessellation results

Layer	r_{max}	bin-size	minimum fit-width	maximum fit-width	fit-range	A	B
10	523	10	50	180	$0 \leq \theta \leq 1.08$	0.493(3)	0.76(2)
11	903	10	90	280	$0 \leq \theta \leq 0.97$	0.500(1)	0.774(9)
12	1554	15	150	495	$0 \leq \theta \leq 1.00$	0.498(2)	0.81(2)
...	∞	0.502(3)	0.82(2)

From the linear fit of the boundary-boundary correlators we extracted Δ , which can be seen in Fig. 2.8. Again we see the boundary dimension parameter, A , gives a value similar to $d/2 = 1/2$. By studying multiple volumes at sufficiently large boundary mass, $M^2 = 500$, we extrapolate to the infinite volume limit. The result for the B parameter can be seen in Fig. 2.9. We find for our fits $A \simeq 0.506(2)$, and $B \simeq 1.21(2)$.

We have performed a similar analysis for the $\{3, 8\}$ case. In this case, the value of Δ settles down for boundary masses $M^2 \geq 1000$ (Fig. 2.10). So $M^2 = 2000$ is picked to perform the analysis. Few correlator plots are shown in the Fig. 2.11 and bulk mass dependence of the boundary operator is shown in Fig. 2.12 using simulation of twelve layered Poincaré disk.

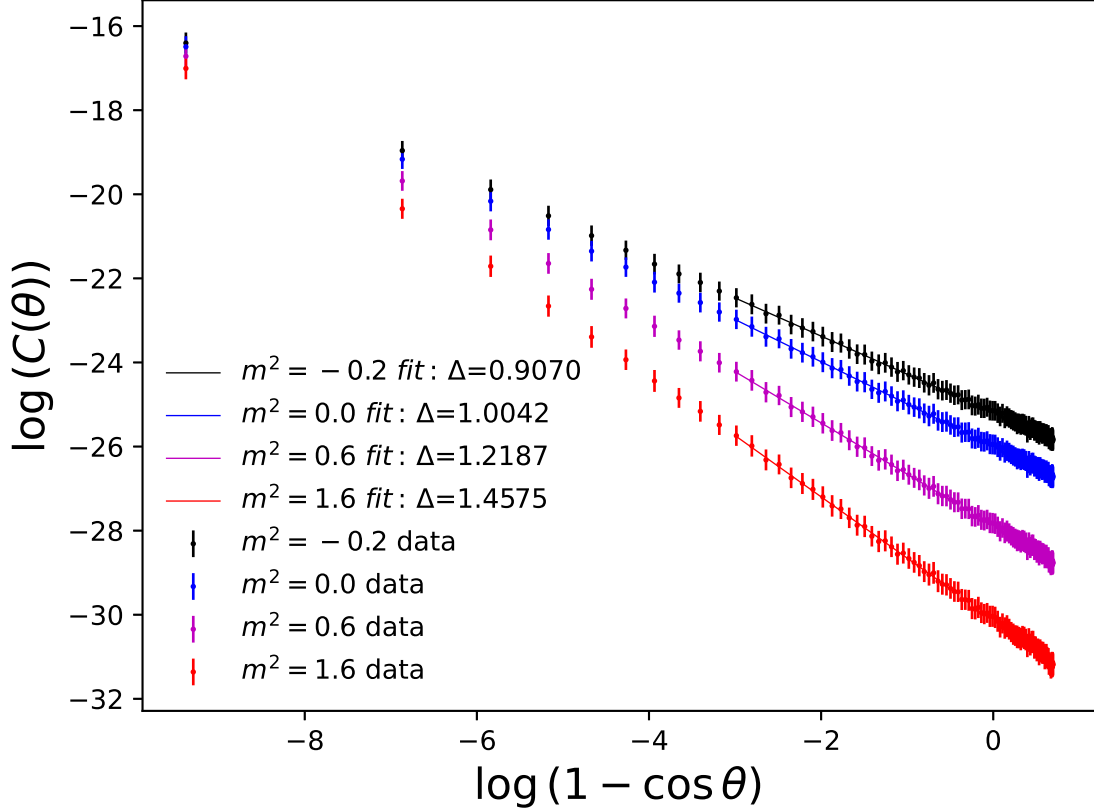


Figure 2.11: The boundary two-point correlator is plotted in log-log coordinates for the lattice $\{p, q\} = \{3, 8\}$. Here four bulk masses are shown for the values of $m_0^2 = -0.1, 0.2, 0.5,$ and 0.8 , with a boundary mass of $M^2 = 2000$. The lattice is comprised of 12 layers of triangles.

The results are summarized in the table 2.1. Notice that the fitted value for $B = 0.82(2)$ is once more close to theoretical expectations which predict $L^2 = B/2 = 0.43$ provided the kinetic term employs the dual lattice weight. A summary of the fit ranges, bin sizes, and parameter values for the $\{3, 8\}$ lattice can be found in table 2.1.

2.4 Three-dimensional hyperbolic geometry

We now transition to the case of three dimensions. First we describe the *honeycomb* used in this investigation, as well as its construction. Honeycombs are tessellations of three-dimensional space, packings of polyhedra that fill the entire space with no gaps.

Similar to the two-dimensional case, in three dimensions, one can succinctly describe

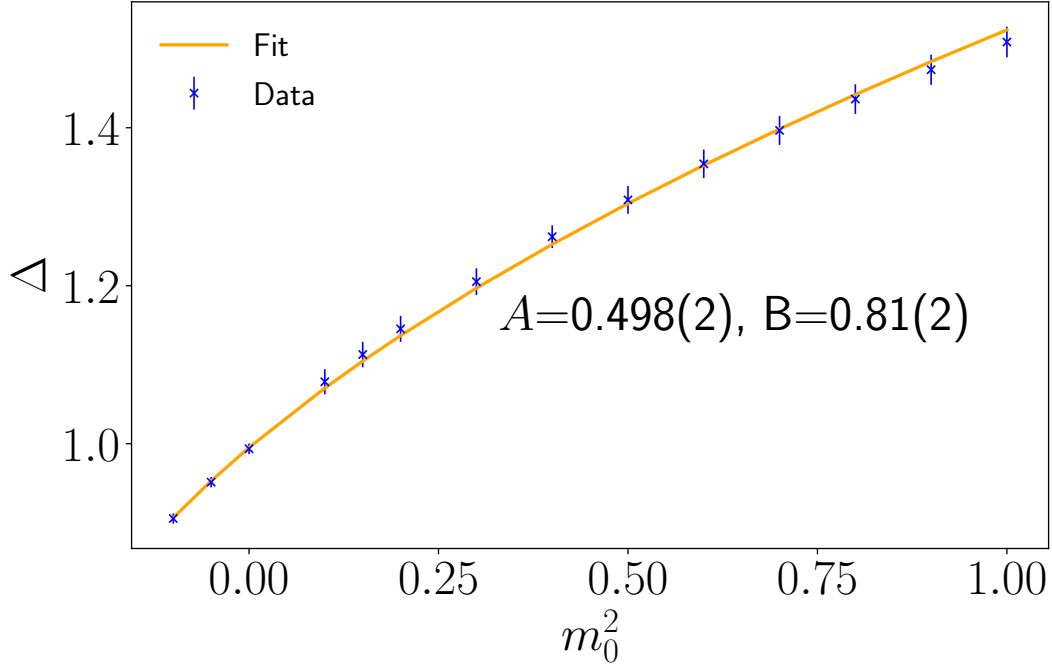


Figure 2.12: The power-law extracted from the correlator data for the $\{p, q\} = \{3, 8\}$ lattice. This data is for a eight layer lattice with a boundary mass of $M^2 = 2000$. The fit parameters for this fit are quoted inside the figure.

regular honeycombs with a Schläfli symbol, a recursive notation for regular tessellations. $\{p, q, r\}$ denotes a honeycomb of $\{p, q\}$ cells, which are polyhedra (or tessellations) of p -gons, where q of these surround each vertex [62]. Here we focus on the $\{4, 3, 5\}$, also known as the order-5 cubical honeycomb, because the $\{4, 3\}$ cubical cells pack 5 polyhedra around each edge. A projection of this lattice can be seen in Fig. 2.13. The excess of cubes around an edge gives a local curvature around each edge differing from flat. Since each Euclidean cube has a face-to-face angle of $\pi/2$, the deficit angle at an edge is $\theta_d = 2\pi - 5\pi/2 = -\pi/2$. For an infinite lattice, this corresponds to 20 cubes around each vertex, and each vertex has 12 neighboring vertices.

To calculate in hyperbolic space, our code operates natively in the Poincaré ball model. In this model, geodesic lines are circular arcs (or lines) orthogonal to the ball boundary, and geodesic surfaces are spheres (or planes) orthogonal to the boundary. Sphere inversions (see [63, pp. 124-126]) in the model equate to reflections in the underlying hyperbolic space and we use this property to build up our honeycomb.

A general, robust sphere inversion function is key– one that handles all special cases of

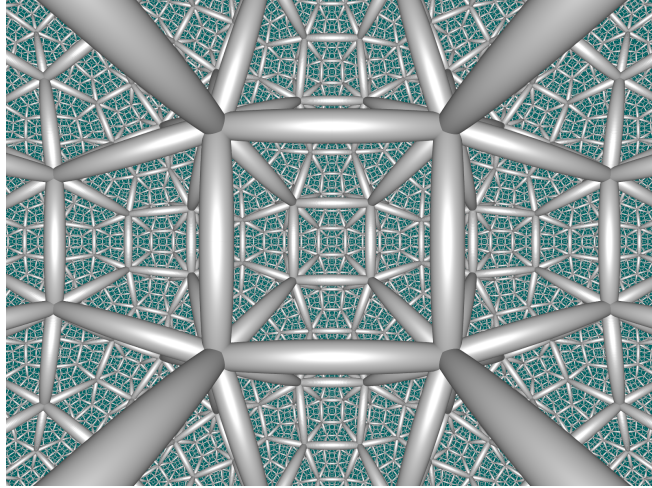


Figure 2.13: An in-space view of the order-5 cubic honeycomb.

spheres or planes reflecting to spheres or planes (as well as the corresponding cases for lines and arcs).

We begin constructing the honeycomb by defining the geometry of a *fundamental tetrahedron* from its six dihedral angles. For regular $\{p, q, r\}$ honeycombs, three of these angles (connected along a zig-zag chain of edges) are $\pi/2$, and the remaining angles are π/p , π/q , and π/r . Using sphere inversion, we recursively reflect the elements of the tetrahedron in its four faces to fill out the space with tetrahedra. Each tetrahedron represents a symmetry of the honeycomb. A fundamental tetrahedron can generate any regular $\{p, q, r\}$ honeycomb with $p, q, r \geq 3$ [64].

In our case, a set of 48 symmetry tetrahedra form each cube. Reflections in the six faces of these cubes build up the cubical honeycomb in layers of cells, with each successive layer containing all cells one step further in the cell adjacency graph of the honeycomb. The number of cubes in each layer are 1, 6, 30, 126, 498, \dots , with the total number of cubes up to each level the sum of the entries in this sequence. This can be seen in Fig. 2.14. We store all the cubes, faces, edges, and vertices that we see during the reflections, taking care to avoid duplicates. In the infinite-volume limit, we would fill the whole of hyperbolic space with cubes.

So far we have described the geometrical construction. We use this information to derive incidence information for all of the elements of the honeycomb, *i.e.* to determine which

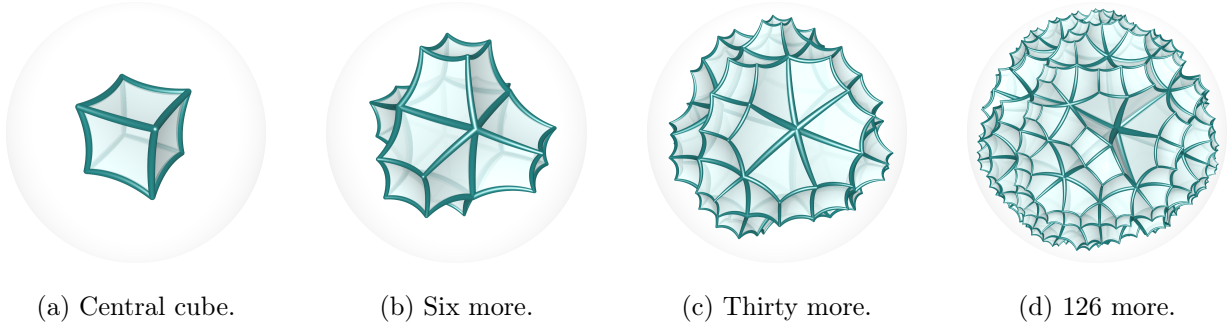


Figure 2.14: Visualization of step-by-step construction of the lattice with layers of cubes in the $\{4, 3, 5\}$ honeycomb. The cube edge lengths appear to vary in length in the Poincaré ball model; however, the lattice here has a fixed edge length, a .

vertices, edges, facets, and cubes connect to each other. This we encode as a list of *flags*. A flag is a sequence of elements, each contained in the next, with exactly one element from each dimension. All possible flags encode the full incidence information of our partially-built honeycombs. The incidence encoding is agnostic to geometrical distances.

We generate lists of flags out to various distances in the cell adjacency graph. The further one recurses, the less edge-effects appear in the incidence information. For example, after adding six layers of cubes, we get enough cells to completely surround all eight vertices of the central cube.

Using the lattice described above, we work with the same model as in two dimensions, and take a naive discretization of the scalar field action (this time in three dimensions) given by,

$$S_{\text{lat}} = \frac{1}{2} \sum_{\langle xy \rangle} p_{xy} V_e \frac{(\phi_x - \phi_y)^2}{a^2} + \frac{1}{2} \sum_x n_x V_v m_0^2 \phi_x^2. \quad (2.15)$$

Here $\sum_{\langle xy \rangle}$ is over nearest neighbors and p_{xy} is the number of cubes around an edge. In the infinite lattice case, p_{xy} is always five, but we leave it as a variable to allow for consideration of the case when the lattice is finite and has a boundary. n_x denotes the number of cubes which share a vertex. Again, in the infinite case this is always 20, but we leave it as a variable for the finite lattice case. V_e and V_v are the volumes associated with an edge and a vertex of a cube, respectively. Since each cube has an edge length of a , $V_e = a^3/12$ and

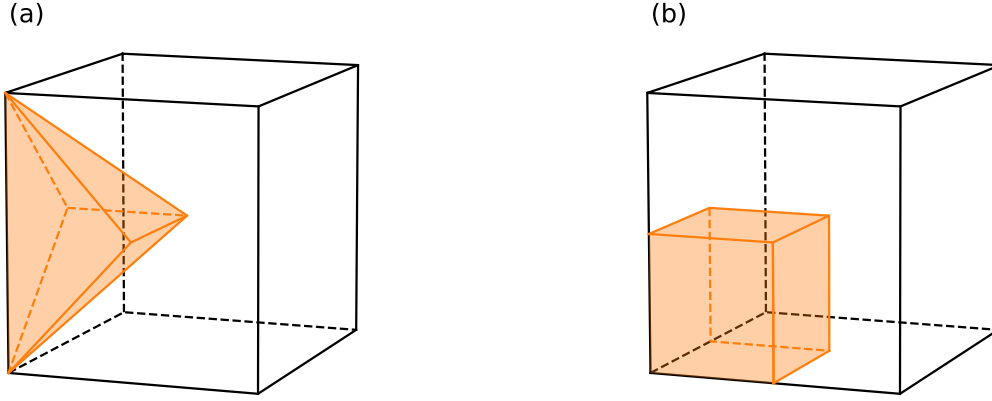


Figure 2.15: (a) The portion of volume associated with an edge of a cube highlighted, in the text, V_e . (b) The portion of volume associated with a vertex of a cube highlighted, in the text, V_v . For a lattice with uniform edge length $a = 1$, these correspond to $1/12$ and $1/8$ respectively.

$V_v = a^3/8$. Illustrations of the two volumes, V_e and V_v are shown in Figs. 2.15(a) and 2.15(b), respectively. The weights again are chosen such that $\sum_{\langle xy \rangle} p_{xy} V_e = \sum_x n_x V_v = V_{\square} N_{\square}$, with V_{\square} being the volume of a cube, and N_{\square} the number of cubes. Above, a is reinserted for clarity but we assume the lattice edge length is one, as before.

We rewrite the lattice action to clearly identify the inverse lattice propagator, even in the presence of a boundary. To do this, we start by expanding and collecting terms to get

$$\begin{aligned}
S_{\text{lat}} &= \frac{1}{2} \sum_{\langle xy \rangle} p_{xy} V_e (\phi_x - \phi_y)^2 + \frac{1}{2} \sum_x n_x V_v m_0^2 \phi_x^2 \\
&= -\frac{1}{2} \sum_{\langle xy \rangle} p_{xy} V_e (\phi_x \phi_y + \phi_y \phi_x) \\
&\quad + \frac{1}{2} \sum_x \left(\sum_y p_{xy} V_e + m_0^2 n_x V_v \right) \phi_x^2,
\end{aligned} \tag{2.16}$$

where \sum_y in the second term is over points neighboring vertex x . Using the fact that

$V_e = (2/3)V_v$, we simplify further to get

$$\begin{aligned}
S_{\text{lat}} &= - \sum_{\langle xy \rangle} \frac{p_{xy}}{3} (\phi_x \phi_y + \phi_y \phi_x) \\
&\quad + \sum_x \left(\sum_y \frac{p_{xy}}{3} + \frac{m_0^2}{2} n_x \right) \phi_x^2.
\end{aligned} \tag{2.17}$$

We express the action in terms of the inverse lattice propagator and get

$$\begin{aligned}
S_{\text{lat}} &= S_{\text{kinetic}} + S_{\text{mass}} \\
&= \sum_{x,y} \phi_x L_{xy} \phi_y
\end{aligned} \tag{2.18}$$

with

$$S_{\text{kinetic}} = - \sum_{x,y} \phi_x \frac{p_{xy}}{3} \delta_{x,y+\hat{1}} \phi_y \tag{2.19}$$

and

$$S_{\text{mass}} = \sum_{x,y} \phi_x \left(\left(\sum_z \frac{p_{xz}}{3} \delta_{z,x+\hat{1}} \right) + \frac{m_0^2}{2} n_x \right) \delta_{x,y} \phi_y. \tag{2.20}$$

In the case of an infinite lattice, this simplifies to

$$L_{xy} = -\delta_{x,y+\hat{1}} + 12 \left(1 + \frac{m_0^2}{2} \right) \delta_{x,y}, \tag{2.21}$$

which is expected for a lattice with 12-fold coordination. Using Eqs. (2.19) and (2.20), we construct an inverse lattice propagator for the hyperbolic lattice considered here, and use it in numerical computations.

Again, the boundary correlator is given by inverting the matrix corresponding to the discrete scalar inverse propagator. A typical set of correlators are shown in Fig. 2.16, corresponding to four bulk masses and squared boundary mass $M^2 = 10$. We take multiple sources on the boundary and compute the one-to-all correlator for those sources on the boundary. In Fig. 2.16 we again plot the correlator as a function of $1 - \cos(\pi r/r_{\text{max}})$. The geodesic

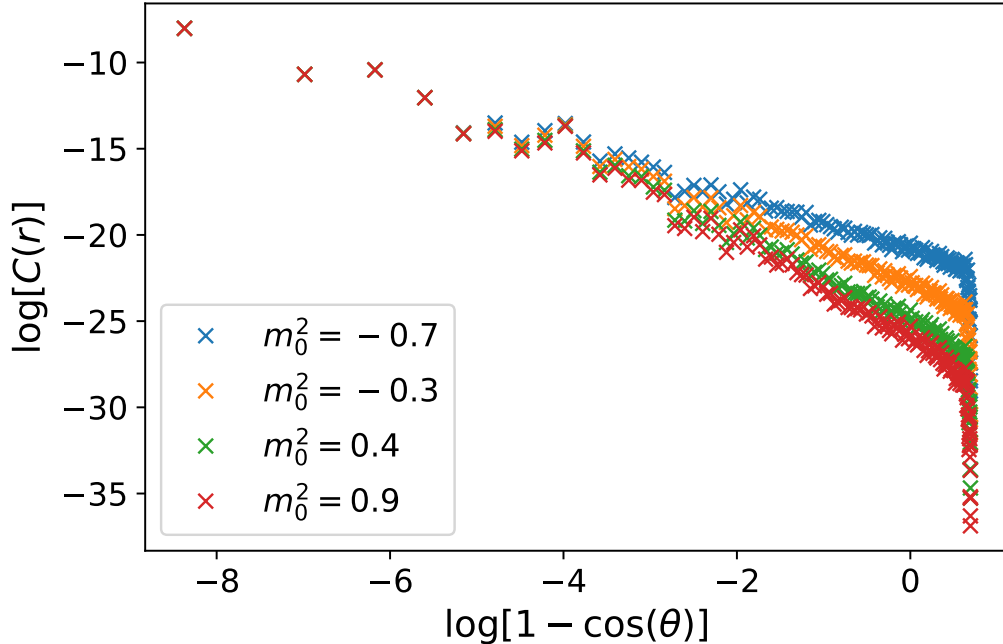


Figure 2.16: A log-log plot of the boundary-boundary correlator, $C(r)$, as a function of distance along the boundary, for a seven-layer lattice. Here the bulk masses from top to bottom are $m_0^2 = -0.7, -0.3, 0.4$, and 0.9 , and the boundary mass is $M^2 = 10$.

distance r is computed by starting at the source vertex, taking a step to all neighboring boundary vertices, then taking a step from those vertices to their neighboring boundary vertices, skipping vertices that have already been visited, and so on, until all vertices have been visited. The error bars are produced using the jackknife method on the sources.

Clearly, a distance window exists in which the correlator follows a power law. This power-law behavior is observed for all masses explored in this study, and seems to solely be a consequence of the lattice geometry. We fit a power law to this window for a series of fixed, squared bulk mass. By far the largest source of error in this analysis is the systematic error in choosing a fit range. To improve this error, we bin the data in the regime of interest, and vary the fit range in the binned data. By resampling from all the reasonable fit ranges we acquire a systematic error. The jackknife error from the sources is added in quadrature with this systematic error to produce the final errors on each power-law fit. From this fit, we obtain the power versus the squared mass.

In the continuum, in the case of anti-de Sitter space, the boundary-boundary two-point

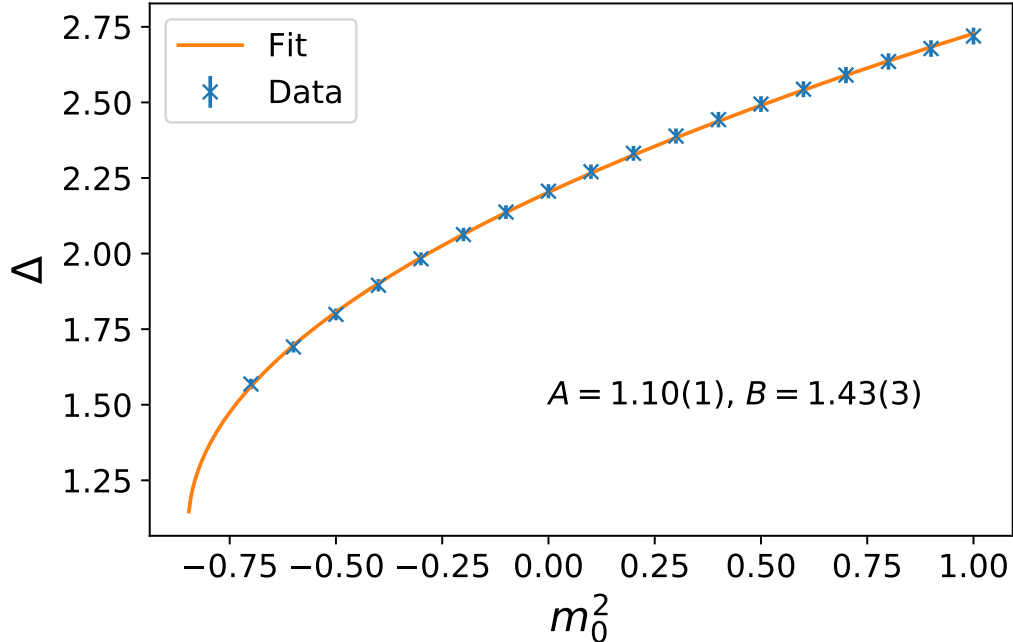


Figure 2.17: A fit of Δ versus the squared mass using Eq. (2.11) for a six-layer lattice. Here the boundary mass is $M^2 = 10$.

correlator is expected to show the behavior from Eq. (2.2) with boundary dimension $d = 2$. We attempt a fit using Eq. (2.11). An example of the fits can be seen in Fig. 2.17. We note that the power, Δ , is well-defined even in the regime of negative squared mass, indicating the operator $-\nabla^2 + m_0^2$ is positive in this regime. Based on these numerical results, the behavior of Δ here matches well with the expected behavior of Δ_+ expressed in Ref. [20].

By repeating this analysis with multiple volumes, we consider the extrapolation to infinite volume. Here we consider three different volumes, corresponding to five, six and seven-layers of cubes. These correspond to 2643, 10497, and 41511 cubes, respectively. Using the fit parameters from multiple volumes allows us to extrapolate to infinite cubes. In Figs. 2.18 and 2.19 we see the finite-size scaling of the fit parameters, A and B , respectively, from Eq. (2.11). The fit is of the form of Eq. (2.12), with N_{bound} being the size of the two-dimensional boundary of the three-dimensional hyperbolic lattice. We find $A_\infty \simeq 1.11(2)$, and $B_\infty \simeq 1.62(9)$ in the infinite volume limit, with the squared boundary mass $M^2 = 10$.

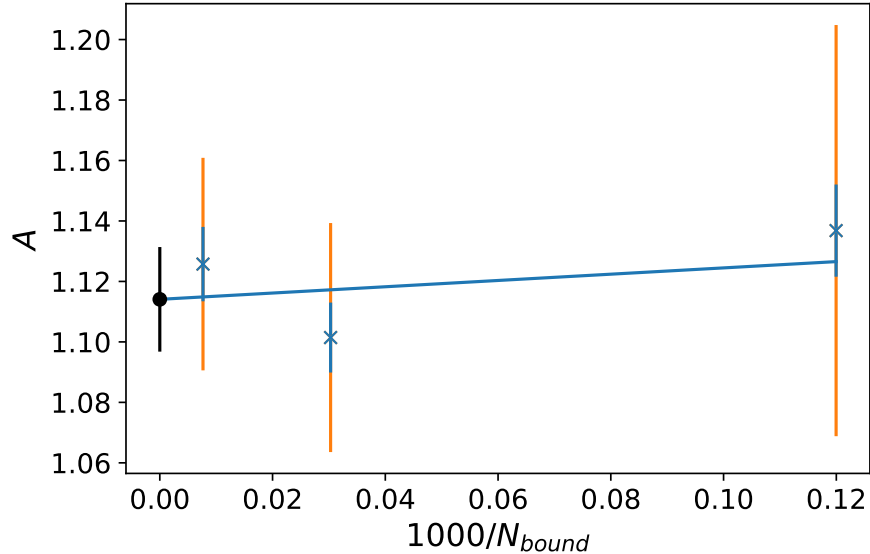


Figure 2.18: The finite-size scaling of the fit parameter, A , from Eq. (2.11). The volumes have been rescaled by 1000 for readability. All three volumes use the same boundary mass of $M^2 = 10$.

2.5 Conclusions

In this chapter we have studied the behavior of boundary correlations of massive scalar fields propagating on discrete tessellations of hyperbolic space. Both two and three dimensions are examined and good quantitative agreement with the continuum formula relating the power of the boundary two-point correlator to the bulk mass is obtained. Specifically, the functional form for the dependence of the boundary scaling dimension on bulk mass is reproduced accurately, including the inferred dimension of the boundary theory. A single parameter, B , identifies the effective squared radius of curvature of the lattice. In fact, in two dimensions, if one considers the continuum formula for the squared radius of curvature for a $\{p, q\}$ -tessellation of \mathbf{H}^2 ,

$$L^2 = \frac{1}{4 \operatorname{arccosh}^2 \left(\frac{\cos(\pi/p)}{\sin(\pi/q)} \right)}, \quad (2.22)$$

one would predict values of 0.84, 0.43 and 0.64 for $\{3, 7\}$, $\{3, 8\}$ and $\{4, 5\}$ tessellations, respectively. These numbers differ from our fitted values for B by a factor of approximately

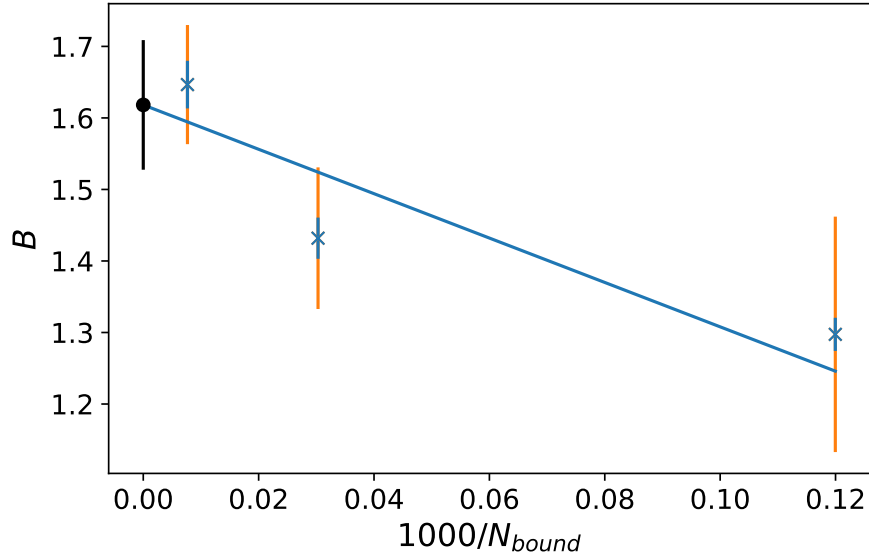


Figure 2.19: The finite-size scaling of the fit parameter, B , from Eq. (2.11). The volumes have been rescaled by 1000 for readability. All three volumes use the same boundary mass of $M^2 = 10$.

two (see the appendix). This factor of two can be completely understood in terms of our choice of weights. If one uses the dual weight prescription for the kinetic term as given in [59] which sets $p_{xy}V_e = \ell a$ where ℓ is the dual edge length, and a is the lattice spacing, this factor of two arises naturally and gives the correct normalization for the squared radius of curvature.

In this work we held the lattice spacing fixed at $a = 1$. This appears in the results of the correlator at short distances as wiggles in the data, and at longer distances as a spread, and noise, in the correlators. This is particularly apparent in the $\{4, 5\}$ correlator data in the appendix. One could refine the tessellation to approach the continuum manifold. In Ref. [59] they did exactly this and considered a refinement of the $\{3, 7\}$ tessellation by continually inserting triangles inside of existing triangles at a fixed physical volume.

A very interesting next step would be to investigate the effects of allowing for dynamical fluctuations in the discrete geometries in order to simulate the effect of gravitational fluctuations-perturbative and non-perturbative. In such scenarios, the effects of the back reaction of matter fields on the geometries can be explored. If the holographic behavior persists in non-perturbative regime, it should allow us to develop holographic dictionary in regimes

that are difficult to explore using analytical approaches. We will hold on to this endeavor until chapter 4. In the next chapter, we will consider another model – Ising model – on fixed background geometry. Fundamental difference is that the model has nearest neighbour interaction whereas the model considered in this chapter is a free field theory.

Chapter 3

Ising spins on hyperbolic space

3.1 Introduction

Motivated by the success of investigating AdS/CFT correspondence for a free scalar field model in lattice setting, we now attempt to use Monte Carlo simulation to investigate the Ising model formulated on tessellations of the two-dimensional hyperbolic disk. We focus in particular on the behavior of boundary-boundary correlators, which exhibit power-law scaling both below and above the bulk critical temperature indicating scale invariance of the boundary theory at any temperature. This conclusion is strengthened by a finite-size scaling analysis of the boundary susceptibility which yields a scaling exponent consistent with the scaling dimension extracted from the boundary correlation function. This observation provides evidence that the connection between continuum boundary conformal symmetry and isometries of the bulk hyperbolic space survives for simple interacting field theories even when the bulk is approximated by a discrete tessellation.

As discussed in the previous section, boundary correlators bear signature of the conformality of the boundary theory. Key to the holographic duality is the relation between boundary and bulk distance. In a space with negative curvature, in this discussion presumed to be rigid, the length of a bulk geodesic between two boundary points is logarithmic in the distance for a path restricted to the boundary hypersurface. Specifically, $\sqrt{-k} d_{\text{bulk}} \sim \log(\sqrt{-k} d_{\text{boundary}})$, where k is the curvature of the hyperbolic space.

At generic points in coupling space, a bulk $d+1$ dimensional theory will be gapped at scale

μ , and correlation functions will decay exponentially, falling off like $e^{-\mu d_{\text{bulk}}}$. If expressed in terms of distance along the boundary, that same correlator will instead fall off as a power-law: $(d_{\text{boundary}})^{-\mu}$. Hence, the geometry of the bulk thus dictates that conformal behavior on the boundary will be robust as physical parameters of the bulk theory are varied.

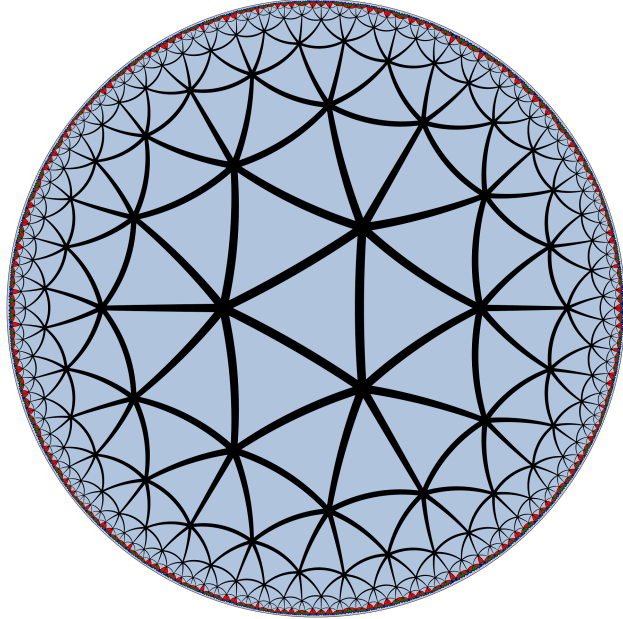
Surprisingly, the most remarkable feature of this duality—the robustness of critical behavior of the boundary theory—persists even when only crude features of the geometry and field content are maintained. For example: in previous chapter, we studied a model of a massive free scalar field propagating on tessellations of two and three-dimensional hyperbolic space. Despite strong lattice artifacts associated with finite lattice spacing and finite volume, the boundary lattice theory displays the usual features of conformality, exhibiting power-law fall-off of boundary-to-boundary correlators with boundary distance, where the inferred scaling dimensions match precisely with continuum analysis.

Here we take the story further, exploring a simple but strongly interacting lattice quantum field theory living on hyperbolic space. The Ising model on the discretized Poincaré disk exhibits phase structure much like the flat space 2D Ising model: it possesses gapped ferromagnetic and paramagnetic phases separated by a phase transition. However, we will show that boundary-to-boundary correlators exhibit signals of criticality for a wide range of temperatures, as predicted by properties of the geometry.

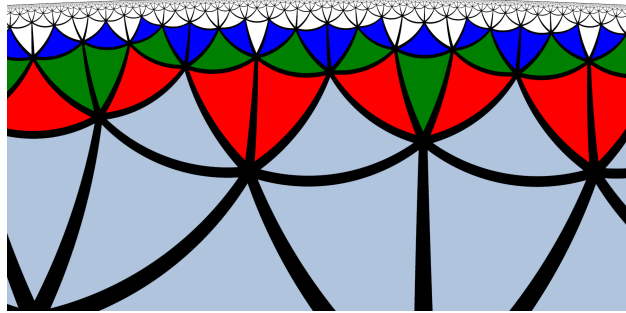
This study is novel in that it explores the impact of strongly coupled bulk physics on the AdS/CFT correspondence. The correspondence is more typically understood in the regime of large N CFTs with weakly coupled AdS duals, so this paper probes the correspondence in a regime uniquely suited to the tools of lattice quantum field theory.

To form our conclusions, we have used Monte Carlo simulation and measured both boundary and bulk observables—with emphasis on the boundary observables—for a range of temperatures. We furthermore show that this behavior can be understood theoretically using a combination of high-temperature expansion and duality arguments.

The organization of this chapter is described here for the reader. In section 3.2, we describe the model in detail and discuss the bulk phase structure. In section 3.3 we investigate the behavior of boundary observables—the two-point correlation function and thermodynamics. We summarise our main results and discuss the prospects of our work in section 3.4.



(a) $\{3, 7\}$ disk



(b) Boundary structure of the disk

Figure 3.1: (a) The full $\{3, 7\}$ lattice, highlighting 10 layers and 591 nodes. The first 10 layers are drawn in one color and the subsequent 3 layers each colored uniquely. (b) A close-up of the boundary of the lattice. Connectivity of the boundary vertices has no fixed pattern as additional layers are added.

3.2 The model and bulk phase structure

We construct a $\{3, 7\}$ tessellated disk as shown in Fig. 3.1 to obtain a lattice representation of hyperbolic geometry. Details of the lattice construction can be found in the previous two chapters in Section 1.5 & Section 2.2. We place Ising spins on each vertex of the tessellation shown in the figure. The partition function of the nearest-neighbor Ising system is then given

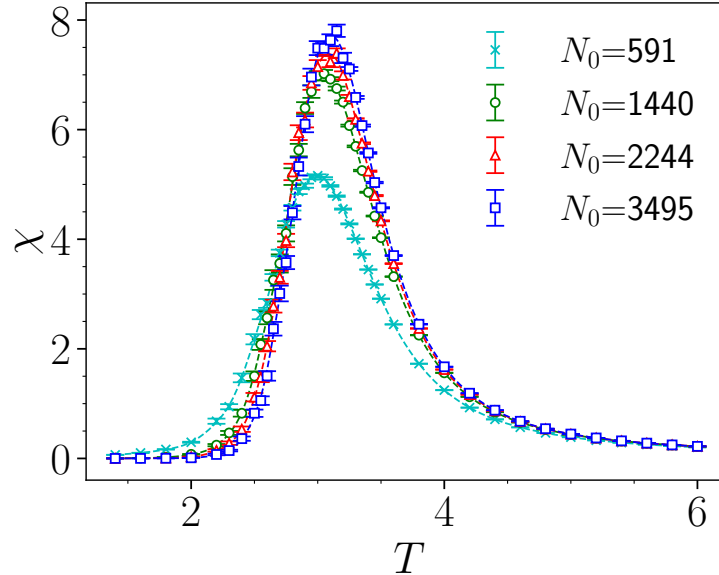


Figure 3.2: The bulk magnetic susceptibility computed from $N_{\text{bulk}} = 591$ spins on the 10 innermost layers of the tessellation as additional outer layers are added up to a maximum of $N_0 = 3495$.

by

$$Z = \sum_{\{s\}} \left[\prod_{\langle ij \rangle} \exp(\beta s_i s_j) \right]. \quad (3.1)$$

where, β is the inverse of the temperature (T), the product $\prod_{\langle ij \rangle}$ is over all nearest-neighbor pairs, and the sum $\sum_{\{s\}}$ is over all possible spin configurations. We simulate the model with Markov chain Monte Carlo using the Metropolis and Wolff cluster algorithms. The algorithms are reviewed in the introductory chapter at Section 1.6.1 & Section 1.6.2.

We use open boundary conditions in our work. Since the fraction of vertices on the boundary relative to the bulk is essentially constant as the volume increases for such a tessellation, one must then be careful in defining the expectation value of bulk observables. We have examined the dependence of such bulk expectation values on the distance from the boundary by comparing expectation values over a fixed set of innermost layers of the tessellation as additional outer layers are added. We first present result of the magnetic susceptibility χ which shows a clear peak when plotted against temperature. The susceptibility

of the magnetization was computed using the following definition

$$\chi = \frac{\beta}{N_{\text{bulk}}}(\langle M^2 \rangle - \langle M \rangle^2). \quad (3.2)$$

Figure 3.2 shows a plot of the bulk magnetic susceptibility versus temperature for a series of lattices ranging up to $N_0 = 3495$ vertices where the bulk quantity is only computed using the $n = 10$ innermost layers corresponding to $N_{\text{bulk}} = 591$ spins. It is straightforward to extrapolate such data to the case where the bulk lies an infinite distance from the boundary. In practice, we observe that allowing for three outer layers leads to results that are independent of these limiting values within statistical errors.

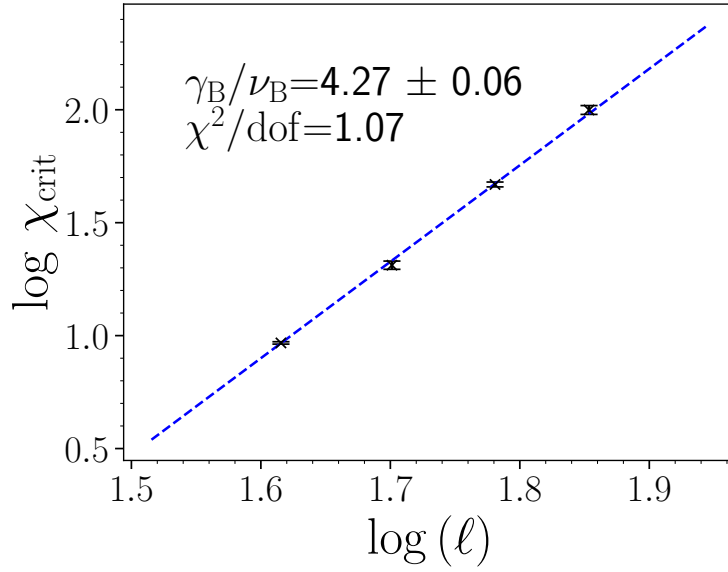
We also examine the finite-size scaling of susceptibilities considering bulk spins $N_{\text{bulk}} = 153, 240, 378$ and 591 . The scaling of the peak of the bulk susceptibility is shown in Fig. 3.3a which plots the logarithm of the peak height versus the logarithm of the linear scale $\ell = \log N_{\text{bulk}}$ that characterizes the geometry. On a hyperbolic disk, it is a natural choice for ℓ since this characterizes maximum bulk lattice geodesics and the system is pseudocritical once the correlation length approaches this scale. The slope of the linear fit yields an estimate of the bulk critical exponent $\gamma_B/\nu_B = 4.27(6)$. We also showed data collapse of the rescaled susceptibility data 3.3b and extracted best choice of the exponent $\nu_B = 0.55$. Again, the choice of characteristic length scale is of the order of the diameter of the Poincaré disk and so $\ell = \log N_{\text{bulk}}$ is chosen.

We present additional results of the bulk observables like magnetization, energy and heat capacity to further justify the position of the critical point. The following definitions were used to compute the absolute magnetization per spin

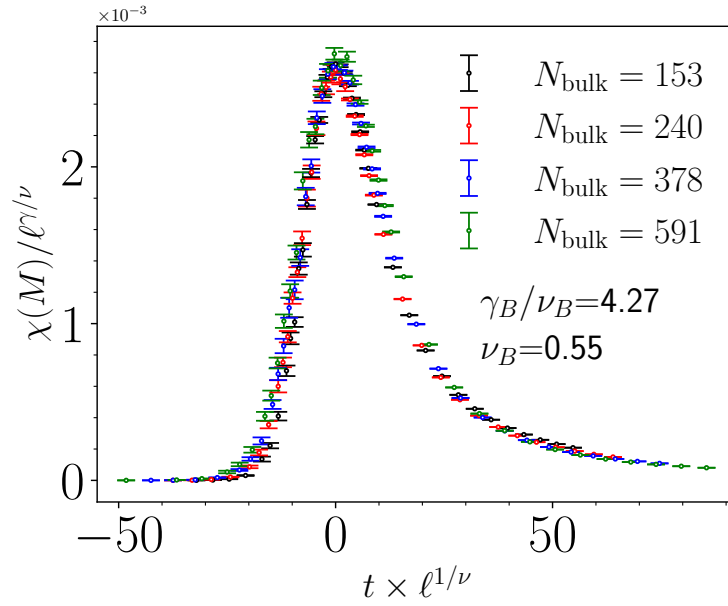
$$m = \frac{M}{N_{\text{bulk}}} = \frac{1}{\mathcal{N}} \sum_{\text{configs}} \left(\frac{1}{N_{\text{bulk}}} \left| \sum_{j \in \text{bulk}} s_j \right| \right), \quad (3.3)$$

the internal energy per spin

$$\epsilon = \frac{E}{N_{\text{bulk}}} = \frac{1}{\mathcal{N}} \sum_{\text{configs}} \left(\frac{1}{N_{\text{bulk}}} \sum_{\langle jk \rangle \in \text{bulk}} s_j s_k \right), \quad (3.4)$$



(a)



(b)

Figure 3.3: (a) The peak in the bulk susceptibility vs $\ell = \log(N_{\text{bulk}})$ in log-log coordinates. The scaling exponent γ_B/ν_B corresponds to the slope of the fitted line. (b) Collapsing bulk susceptibility data with rescaling allows to find the exponent ν_B .

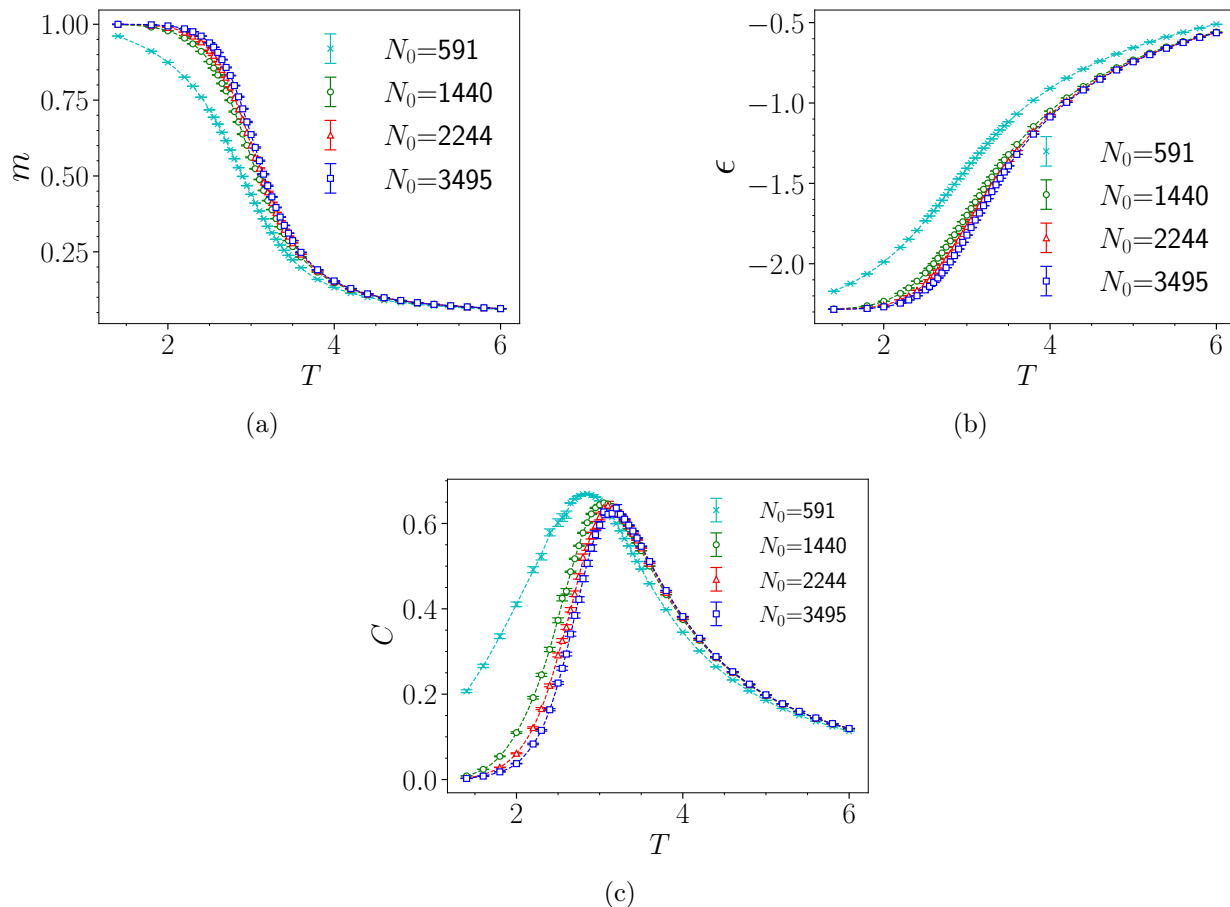


Figure 3.4: (a) Bulk magnetization, (b) internal energy and (c) heat capacity are computed from $N_{\text{bulk}} = 591$ spins on 10 innermost layers of the tessellation as additional outer layers are added up to a maximum of $N_{\text{total}} = 3495$.

and heat capacity per spin was computed with

$$C = \frac{\beta^2}{N_{\text{bulk}}} (\langle E^2 \rangle - \langle E \rangle^2). \quad (3.5)$$

Here, \mathcal{N} denotes the total number of thermalized configurations in the simulation which is $\sim 10^7$ sweeps for the Metropolis algorithm and ~ 15000 sweeps for the cluster algorithm. Each sweep in the metropolis algorithm attempts N_0 spin flips while each sweep in the cluster algorithm attempts ~ 15000 cluster flips. N_0 is the number of total vertices in the lattice; that is, it includes both what we consider as bulk spins and what we consider as outer layer spins.

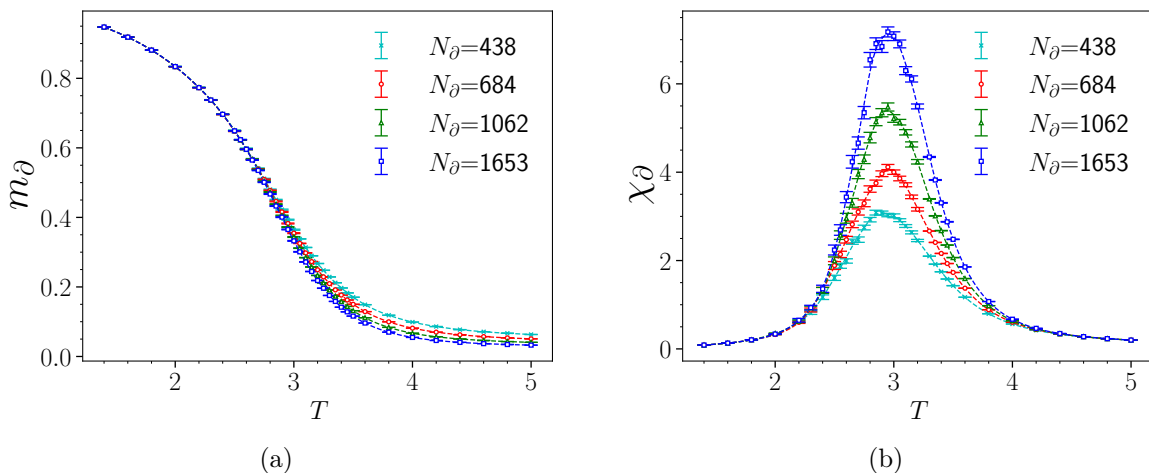


Figure 3.5: (a) Boundary magnetization and (b) boundary susceptibility are plotted against bulk-temperature from 10 to 13 layered Poincaré disk with increasing number of boundary spins N_∂ .

Plots for the magnetization, internal energy per spin and heat capacity are shown in Fig. 3.4. Again we find that for a certain number of bulk spins N_{bulk} , adding more outer layers gradually alleviate the boundary effects while computing bulk quantities. We find that adding 3 additional layers is sufficient for the lattice bulk volumes we investigated. Notice that the use of an open boundary condition means that our current work differs from earlier studies. For example, Ref. [65] studies the bulk properties of the model having imposed a periodic boundary condition on the boundary. This boundary condition corresponds to using a hyperbolic manifold with genus $g \geq 1$ [65, 66]. In contrast, Nishino *et al.* use a fixed ferromagnetic boundary condition in their Corner Transfer Matrix renormalization group approach [67]. Earlier works using Padé approximations from the low and high-temperature expansion can be found in Ref. [68].

However, the open boundary condition we employ in the current work is the more natural choice in a holographic context that closely resembles a Dirichlet condition. The scheme we use for implementing the open boundary condition is similar in spirit to the work of Shima *et al.* [69].

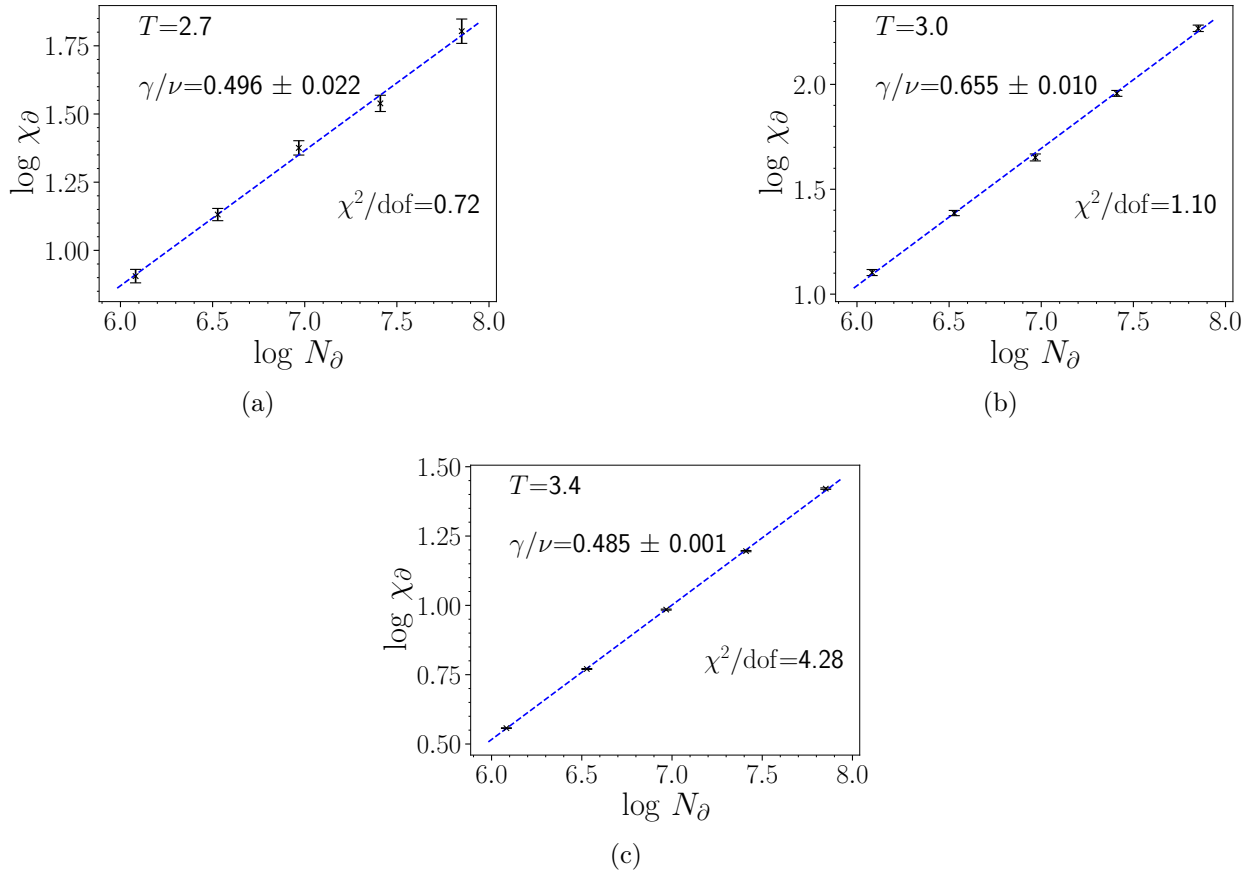


Figure 3.6: Logarithm of the boundary susceptibility (χ_∂) is plotted against logarithm of the total number of boundary points (N_∂) for $T =$ (a) 2.7, (b) 3.0, (c) 3.4. Scaling exponents of the boundary susceptibility (γ/ν) are computed from the linear fit of the data.

3.3 Boundary Thermodynamics

In this section, we will focus on the boundary observables. Fig. 3.5a and Fig. 3.5b show the plot of (the absolute value of) the boundary magnetization and magnetic susceptibility versus temperature for a range of lattice sizes. Notice that the latter exhibits a peak close to that seen in the bulk susceptibility. However, this peak is broad and shows no sign of narrowing with increasing lattice size. Indeed, if we attempt a finite-size scaling analysis of the susceptibility we find evidence for a line of a continuously varying critical exponent γ/ν —see Fig. 3.6.

Associated with this scaling, we can examine the boundary-boundary correlators over the same range of temperatures. Correlation functions for three temperatures are shown in

Fig. 3.7 with a choice of “best-fit” with the solid line. After binning the data, we proceed using a single-elimination jackknife. Then, we perform correlated fits. We fit over several fit ranges to estimate a systematic error associated with our “best” choice of fit range. Our fit ansatz has the form,

$$\langle s(0)s(r) \rangle = a(T) + b(T)r^{-2\Delta(T)}, \quad (3.6)$$

where the distance measured on the boundary r can be traded for an angle via the relation $r^2 \sim (1 - \cos \theta)$. Notice that the conformal behavior is given by the connected correlator which is insensitive to $a(T)$. The final error shown in the plots includes the systematic error associated with the fit range added in quadrature with the statistical error obtained from the best fit.

The boundary susceptibility is of course nothing more than the integral of this correlation function, and hence we predict that the susceptibility exponent $\gamma/\nu = 1 - 2\Delta$. A plot showing the value of the scaling dimension extracted from the susceptibility together with the value obtained by a power-law fit to the correlation function is shown in Fig. 3.8. The agreement is excellent, furnishes a nice consistency test of our procedure, and provides strong evidence that the boundary theory indeed exhibits power-law behavior both at high and low temperatures. The minimal value of the boundary scaling dimension Δ is obtained for $T \sim T_c$ corresponding to the point where the bulk mass gap on hyperbolic space has been tuned to zero. Notice that once $1 - 2\Delta < 0$, the susceptibility no longer diverges with lattice size, which explains the location of the edges of the broad peak shown in Fig. 3.5b.

In fact it is easy to see that the boundary correlation function should exhibit a power law for high temperature. Expanding the Boltzmann factors for small β we find the correlator is given by

$$\langle s_k s_\ell \rangle \propto \sum_{\{s\}} s_k s_\ell \left(\prod_{\langle ij \rangle} (1 + s_i s_j \tanh \beta) \right). \quad (3.7)$$

The leading-order contribution in β corresponds to the minimal-length path in the lattice between the two boundary spins. On a hyperbolic disk this path runs through the bulk and yields

$$\langle s_k s_\ell \rangle \propto (\tanh \beta)^R \quad (3.8)$$

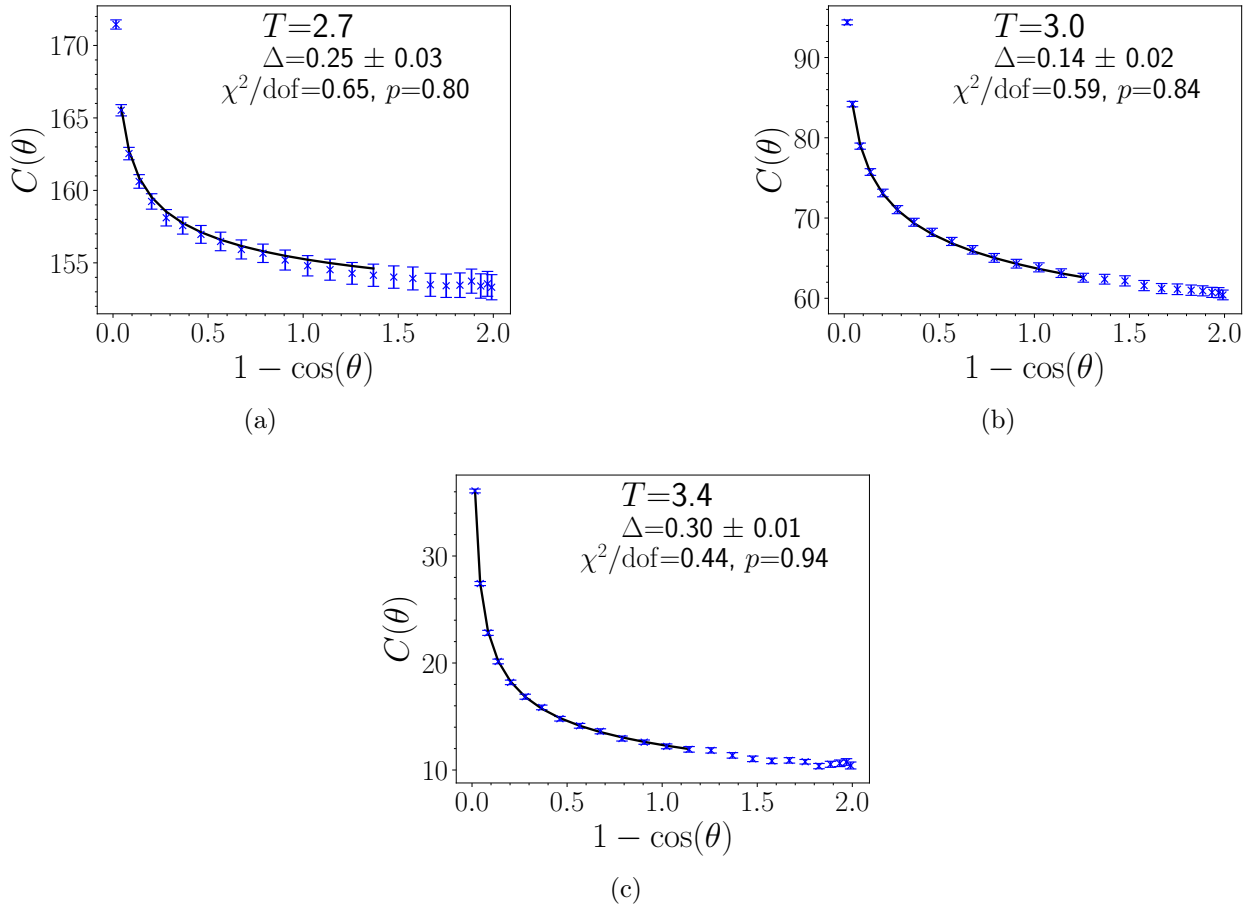


Figure 3.7: The boundary-boundary correlation function at $T =$ (a) 2.7, (b) 3.0, (c) 3.4, plotted against boundary distance squared $r^2 \sim (1 - \cos \theta)$. Results shown here are from the analysis of a 12 layered Poincaré disk with boundary length $N_\partial = 1062$. χ^2 per degree of freedom and the p-value of the fits are noted in the figures.

where R is the length of the geodesic between k and ℓ . But $R \sim \log r$ on the hyperbolic disk with r the boundary distance between the spins. Thus we find

$$\langle s_k s_\ell \rangle \propto r^{-2\Delta} \quad (3.9)$$

where $\Delta \sim \frac{1}{2} \log \coth \beta \sim -\log \beta$ for $\beta \rightarrow 0$. Thus it is natural to expect a conformal boundary phase for a range of high temperatures. To understand the low-temperature behavior we can perform a duality transformation [70] on the model. This maps the original Ising system with spins $\{s_i\}$ on a $\{3, 7\}$ tessellation at (inverse) temperature β into another Ising model with spins $\{\sigma_j\}$ living on the dual $\{7, 3\}$ tessellation at temperature $\tilde{\beta} = \frac{1}{2} \log \coth \beta$.

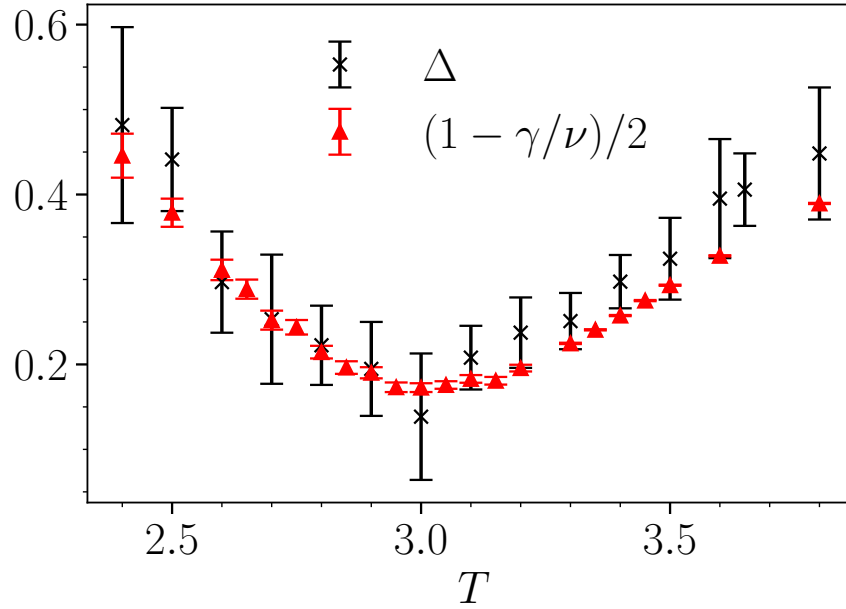


Figure 3.8: The scaling exponent of the boundary spin operator computed from fits to the boundary two-point correlator, denoted by Δ , and from the finite-size scaling of the boundary susceptibility, denoted by $(1 - \gamma/\nu)/2$.

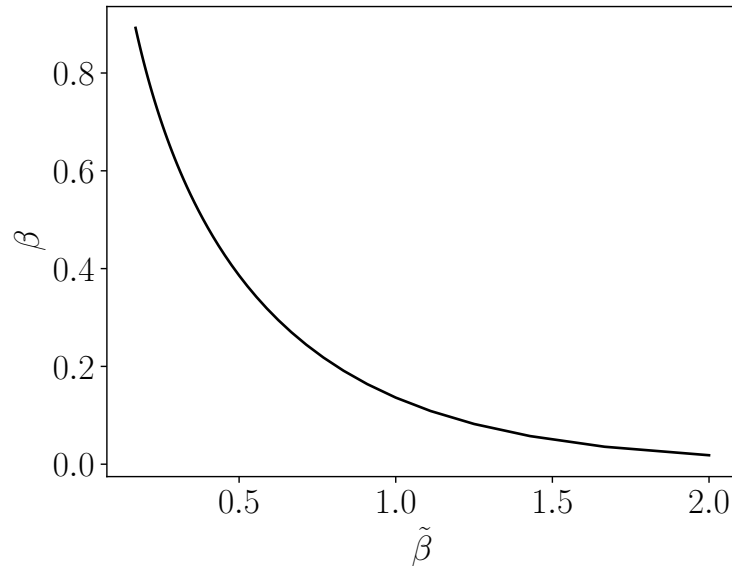


Figure 3.9: Relation between dual inverse temperature and the dual temperature.

Notice that high temperatures in the original model are mapped to low temperatures in the dual model, see the mapping of the dual inverse temperature to the inverse temperature in Fig 3.9. Furthermore, the functional relationship between the boundary distance and the length of the corresponding bulk geodesic is the same for both $\{3, 7\}$ and $\{7, 3\}$ tessellations.

This implies that the power-law behavior of the $\{s_i\}$ system at high temperature produces a power law correlator for the dual $\{\sigma_i\}$ system at low temperature. But the dual system is just another discretization of hyperbolic space and so one concludes that the $\{s_i\}$ boundary correlator on the original lattice should also possess power-law behavior at low temperature with $\Delta \sim \log \coth \tilde{\beta} \sim \beta$ for $\beta \rightarrow \infty$. And indeed, this is precisely what is observed in our simulations.

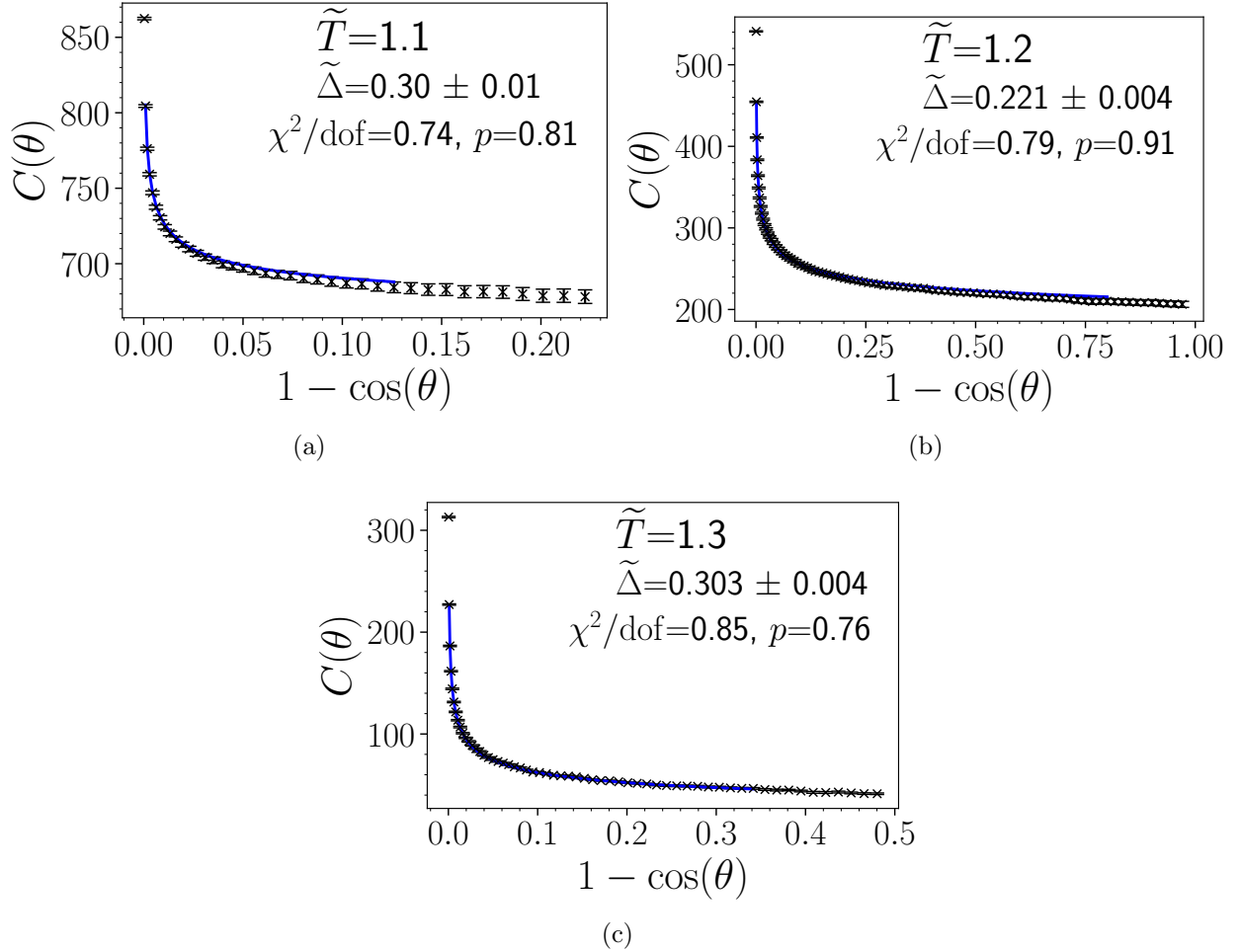


Figure 3.10: The boundary-boundary correlation function of the dual spin variable ($C = \langle \sigma_0 \sigma_r \rangle$) at $\tilde{T} =$ (a) 1.1, (b) 1.2, (c) 1.3 plotted against boundary distance squared $r^2 \sim (1 - \cos \theta)$. Results shown here are from the analysis of a six-layered $\{7, 3\}$ Poincaré disk with boundary length $N_\partial = 3647$.

Next, we show the boundary correlator of the dual-spin variable σ placed on the vertices of the $\{7, 3\}$ tessellated disk. Spin-spin correlator ($\langle \sigma_0 \sigma_r \rangle$) plots at three different temperatures

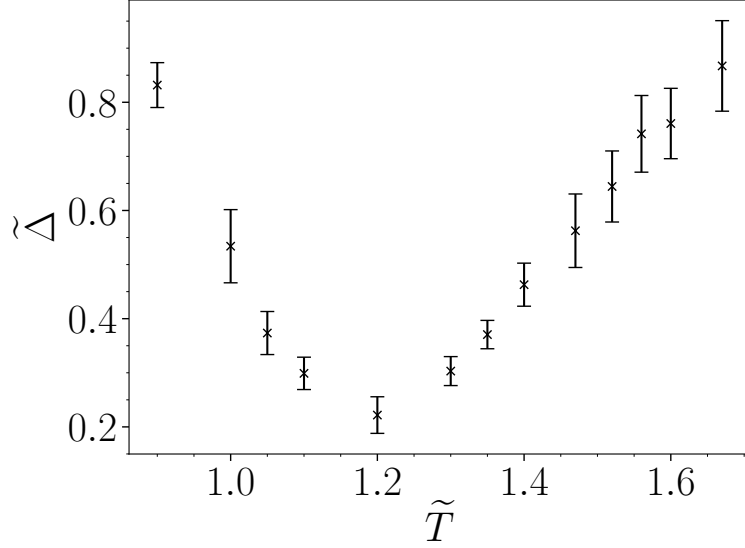


Figure 3.11: Scaling exponent of the dual boundary spin operator ($\tilde{\Delta}$) computed from the fits of the boundary correlator.

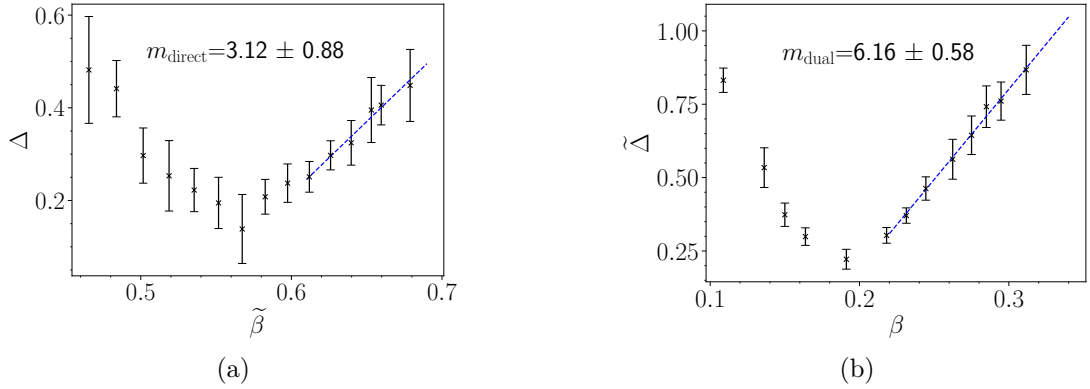


Figure 3.12: (a) Scaling exponents at direct lattice Δ vs. dual inverse temperature ($\tilde{\beta}$), and (b) scaling exponent at dual lattice ($\tilde{\beta}$) vs. inverse temperature at direct lattice (β). Linear fits at high temperature are shown with the extracted slope denoted in the figure.

are shown in Fig. 3.10. Using a similar fitting form described in the main text, scaling dimension $\tilde{\Delta}$ for the correlators of the disorder variables were extracted. We find similar temperature (\tilde{T}) dependence of the scaling exponent $\tilde{\Delta}$ where the lowest point of a dip correlates to the bulk transition temperature, see Fig. 3.11.

The consistency of our measurements of Δ and $\tilde{\Delta}$ can be checked by noting that the high temperature expansions for the spin-spin correlators on both the dual and direct lattice

imply that the correlators take the form

$$G_{\text{direct}} \sim e^{R \log \tanh \beta} \sim e^{-2R\tilde{\beta}} \quad (3.10)$$

$$G_{\text{dual}} \sim e^{\tilde{R} \log \tanh \tilde{\beta}} \sim e^{-2\tilde{R}\beta}. \quad (3.11)$$

where R is the geodesic distance between spins. If we assume the continuum relation $R = \alpha L \log \frac{r}{L}$ with r measured at a finite—effective—boundary, α a constant, and L the AdS radius of the space, these expressions imply the following relations for the scaling dimensions extracted from the boundary correlators

$$\Delta = \alpha L \tilde{\beta} \quad \tilde{\beta} \rightarrow \infty \quad (3.12)$$

$$\tilde{\Delta} = \alpha \tilde{L} \beta \quad \beta \rightarrow \infty. \quad (3.13)$$

In Fig. 3.12 we show plots of Δ v.s. $\tilde{\beta}$ and $\tilde{\Delta}$ v.s. β including a linear fit to the large $\tilde{\beta}$, β regions. The ratio of the slopes is equal to $m_{\text{dual}}/m_{\text{direct}} = 1.97$. If the unit lattice spacing is used for the construction of the Poincaré disk, the AdS radius L for a $\{p, q\}$ tessellation is given by the following formula [71]

$$1/L = 2 \cosh^{-1} \left(\frac{\cos \frac{\pi}{p}}{\sin \frac{\pi}{q}} \right). \quad (3.14)$$

This leads to the prediction $\frac{\tilde{L}}{L} = 1.93$ which agrees remarkably well with the numerical result.

3.4 Summary and Prospects

We have simulated the Ising model on a tessellation of the hyperbolic disk, exploring the AdS/CFT correspondence at strong coupling on the lattice. On a $\{3, 7\}$ tessellation, we find evidence for a bulk phase transition at $T_c \sim 3$ separating a low temperature magnetized phase from a disordered phase at high temperature. Since the number of boundary points is always a constant significant fraction of the bulk points, special care was taken to define bulk observables which are insensitive to the presence of this boundary.

The primary focus of this paper was the correlation functions and thermodynamics of the Ising spins located at the boundary. Our numerical results show that boundary-boundary correlation functions exhibit power-law behavior over a wide range of temperatures starting at high temperature, through the bulk phase transition, and persisting into the low-temperature ordered phase. The high-temperature conformal phase is straightforward to understand using high-temperature expansions and relies only on the geodesic structure inherited by tessellations of hyperbolic space. At low temperatures, arguments rooted in the duality transformation of the Ising model suggest that boundary criticality will persist in the ordered phase.

We conjecture that this low-temperature conformal boundary phase extends all the way to $T = 0$ in the thermodynamic limit but that the rapid increase in the scaling dimension as $T \rightarrow 0$ makes it difficult to verify this on finite lattices.

The fact that the boundary theory is scale-invariant at long distances for any temperature is consistent with the usual arguments for the AdS/CFT correspondence in the continuum which ties the conformal symmetry of the boundary theory to the bulk isometries of anti-de Sitter space. Since our tessellation approximates the latter and is fixed independent of temperature we would not expect the approximate conformality of the lattice theory to depend on couplings in the matter sector.

In this first study of its type, conformal invariance of the boundary theory was apparently maintained through a regime of strongly coupled bulk physics. It will be fascinating to continue exploring the AdS/CFT correspondence in regions where perturbative methods are unavailable. The first step toward this direction is taken through studies of a scalar field on a fluctuating hyperbolic disk in the following chapter.

Chapter 4

Scalar fields on fluctuating hyperbolic geometries

4.1 Introduction

In this chapter we present results on the behavior of the boundary-boundary correlation function of scalar fields propagating on discrete two-dimensional random triangulations representing manifolds with the topology of a disk. We use a gravitational action that includes a curvature squared operator, which favors a regular tessellation of hyperbolic space for large values of its coupling. We probe the resultant geometry by analyzing the propagator of a massive scalar field and show that the conformal behavior seen in the uniform hyperbolic space survives as the coupling approaches zero. The analysis of this boundary correlator suggests that holographic predictions survive, at least, weak quantum gravity corrections. We then show how such an R^2 operator might be induced as a result of integrating out massive lattice fermions and show preliminary results for boundary correlation functions that include the effects of this fermionic backreaction on the geometry.

Regular hyperbolic lattices furnish a representation of wick-rotated anti-de Sitter spacetime. In previous works, we have shown how the AdS-CFT correspondence can be seen by studying the propagation of free massive scalar fields on such hyperbolic lattices [72]. This earlier work confirmed that the correlation function of the scalar fields in the boundary fall-off algebraically with boundary separation. This agrees with what is expected in the

continuum where the magnitude of the scaling exponent Δ of the boundary field operator is related to the bulk scalar mass, m , via the relation given by Klebanov & Witten [20]

$$\Delta_{\pm} = \frac{d}{2} \pm \sqrt{\frac{d^2}{4} + m^2}. \quad (4.1)$$

Here, m is expressed in units of the AdS curvature, while d is the dimension of the boundary. Depending on the choice of the boundary condition, either mode in the equation above can be recovered [20]. The analysis we presented earlier uses a Dirichlet boundary condition which targets the Δ_+ mode.

In this work, we have taken the first steps towards investigating what aspects of holography survive when fluctuations are allowed in the bulk geometry. Such fluctuations represent the effects of quantum gravity, and since they change the continuum isometries of the bulk, they can affect the conformal nature of the boundary theory. These effects are difficult to study in the continuum but can be investigated in the lattice using Monte Carlo simulation. In this work, we first study the effects of introducing a R^2 operator which is designed to favor regular hyperbolic lattices for strong coupling. We then decrease the coupling to probe the structure of the boundary theory as increasingly large fluctuations are allowed in the bulk geometry. We then argue that such an operator is naturally generated in the effective gravitational action after integrating out massive Kähler-Dirac fermions.

The structure of the chapter is described here. In section 4.2, the methodology for studying the fluctuating hyperbolic disk is presented. Next, we present numerical results for the scaling exponents of the boundary field operators for different values of the R^2 coupling in 4.3. In the following section 4.4, we formulate a model which includes dynamical fermions, and in section 4.5, we present preliminary results for the propagator of fermions on such geometries that include the backreaction effects. Finally, we summarize our findings and discuss prospects in section 4.6.

4.2 Introducing bulk curvature fluctuations

To simulate the effects of quantum gravity fluctuations in the bulk we have replaced the regular tessellations studied in our earlier work with more general random triangulations. These are restricted so that connectivity of the boundary nodes is held fixed throughout and corresponds to the connectivity of a regular $\{3, 7\}$ tessellation with some fixed boundary length while the connectivity of the inner bulk nodes is allowed to fluctuate. This approximates the continuum notion that the metric has negative average curvature and approaches AdS at the boundary. The amount of fluctuation in the bulk of the disk is controlled by a discretization of the 2d gravity action supplemented with additional R^2 terms. The partition function can be written as,

$$Z = \sum_{\mathcal{T}} e^{S(k_d, \beta)} \quad (4.2)$$

Here, the summation is carried out over all possible 2d triangulations with disk topology and fixed boundary. The action is given by a sum over a cosmological constant and a curvature squared term S_Q :

$$S = k_2 N_2 + \beta S_Q \quad (4.3)$$

The first term above is the contribution from the pure gravity action in the lattice*. The modified curvature-squared term S_Q takes the form

$$S_Q = \sum_{i \in P_{\text{bulk}}} (q_i - 7)^2 / q_i \quad (4.4)$$

For large β the coordination number of any bulk vertex is driven to seven corresponding to the $\{3, 7\}$ tessellation of the hyperbolic disk.

In practice, we also introduce a volume tuning term S_V . If in a configuration the total number of triangles in the disk is N_2 , then the volume tuning term is

$$S_V = \gamma(N_2 - V)^2. \quad (4.5)$$

The term is required to ensure generating a pseudo-canonical ensemble of geometries of the

*The Einstein-Hilbert term in two dimensions is a topological invariant

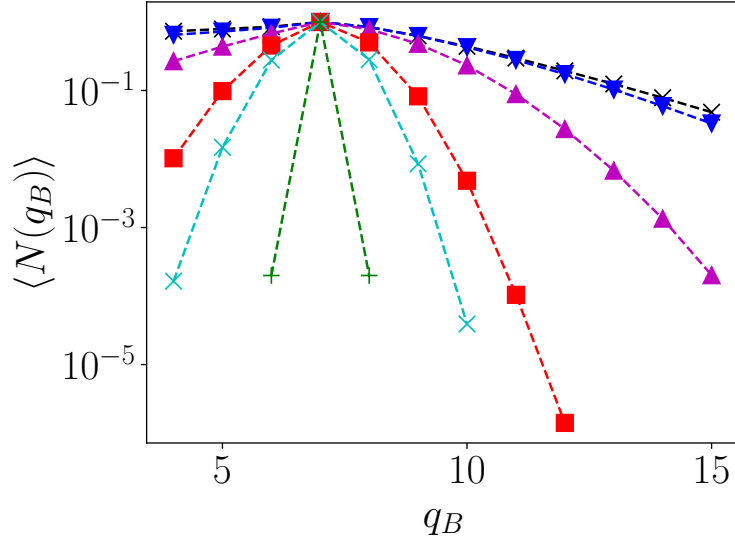


Figure 4.1: Number of bulk vertices $N(q_B)$ with coordination number q are plotted at different β : $\beta = 0.0$ (black), $\beta = 0.01$ (blue), $\beta = 0.1$ (purple), $\beta = 0.5$ (red), $\beta = 1.0$ (cyan), and $\beta = 3.0$ (green).

topology of the disk with a target volume V . The coupling constant γ is periodically adjusted to ensure the volume N_2 of the generated configurations are close to V .

4.3 Results: curvature-squared operator

In this section, we will present our Markov Chain Monte Carlo (MCMC) simulation results for the modified R^2 action defined in eqn. 4.4. We have focused on the properties of the boundary theory and hence have examined the boundary-boundary correlator for a massive scalar field propagating on this geometry. To mock up the effects of a Dirichlet boundary condition on this scalar field we have introduced a large boundary mass. We find that the dependence of the correlators on the boundary mass vanishes as we increase the boundary mass. The analysis was repeated for several bulk masses, and similar behavior was observed for all the cases. For details of the analysis of choosing an appropriate boundary mass to introduce Dirichlet boundary condition is discussed in the appendix of [72].

Once the boundary mass is chosen for the analysis, we investigated several collective geometry properties of the ensemble of dynamically triangulated disks. We performed a strong

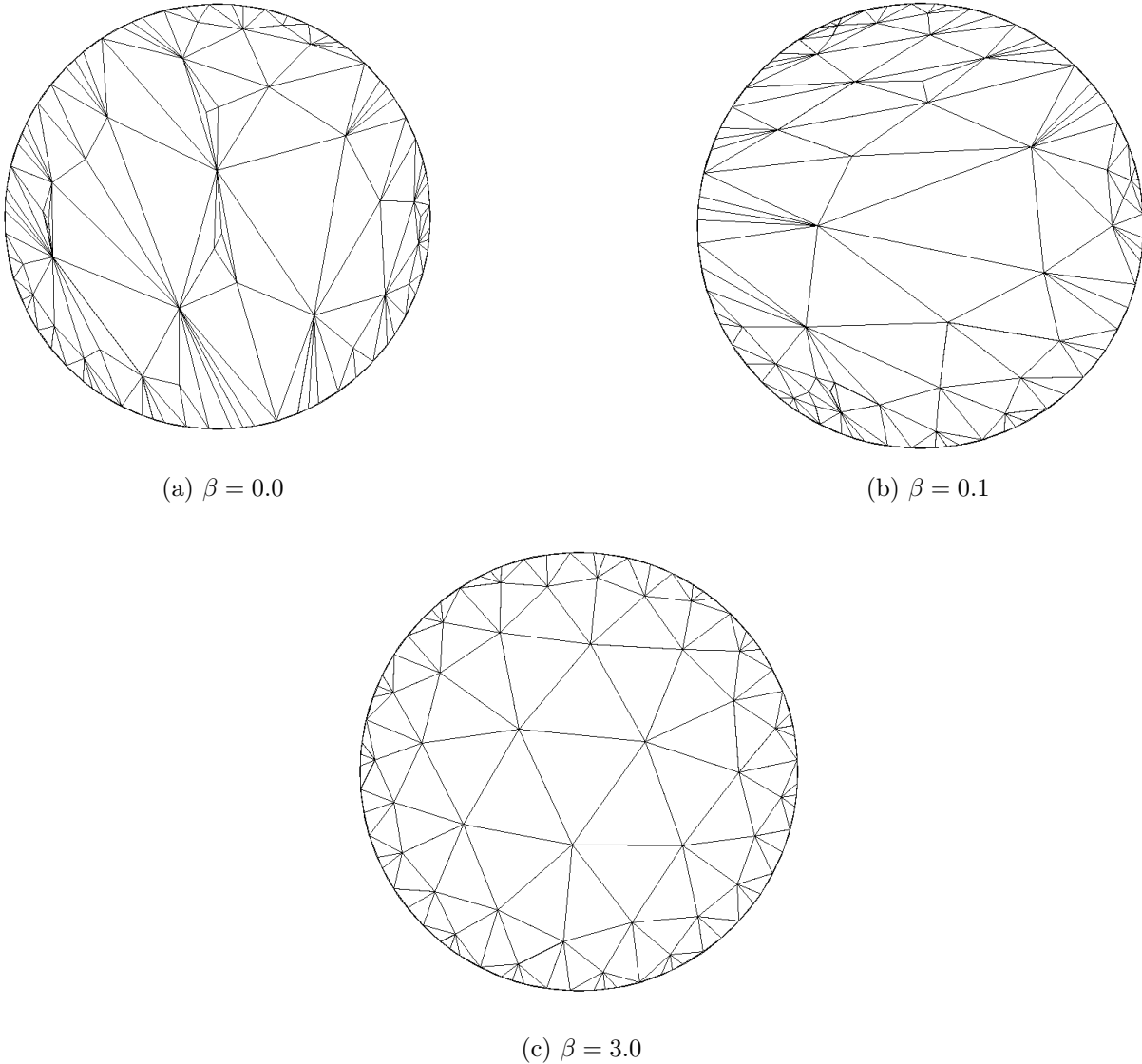


Figure 4.2: Sample thermalized configurations from time evolution of geometry during MCMC simulation at different β .

coupling expansion and compared the numerical results with this strong coupling expansion, giving confidence in our analysis. Fig. 4.1 shows the relative number of vertices (N_{q_B}) with a bulk coordination number q_B at different coupling strength β for a target lattice volume $V = 742$. The peak in the number of vertices N_q is seen at seven at all nonzero coupling we considered and corresponds to a negative curvature. A fixed boundary configuration was deployed in our analysis that resembles the boundary of the $\{3, 7\}$ Poincaré disk. The choice of this initial configuration is sufficient to ensure that the average bulk curvature is

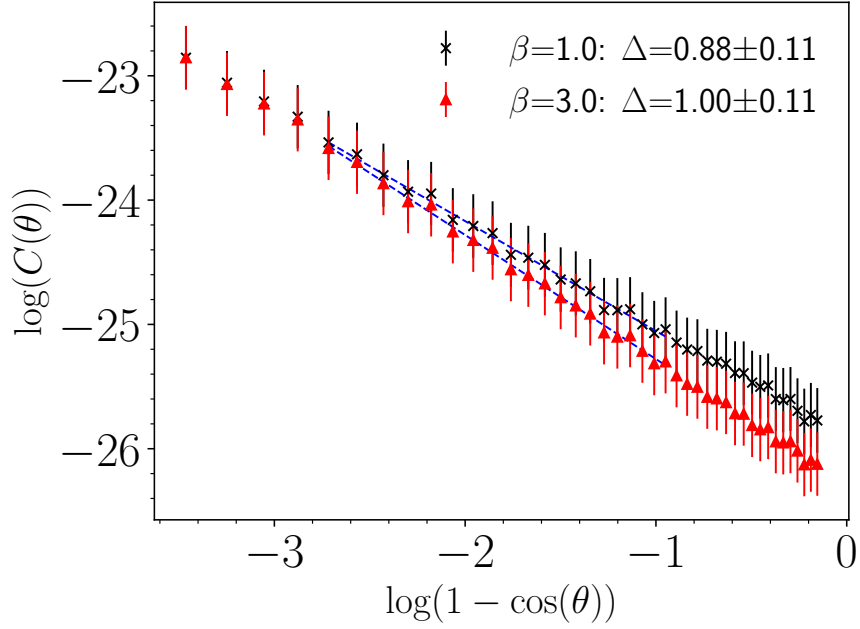


Figure 4.3: Two point function is plotted against boundary distance in angular coordinate for a scalar field with bulk mass $m = 0$, here $r^2 \propto (1 - \cos \theta)$. Slope of the fitted line denotes the scaling exponent Δ of the boundary operator.

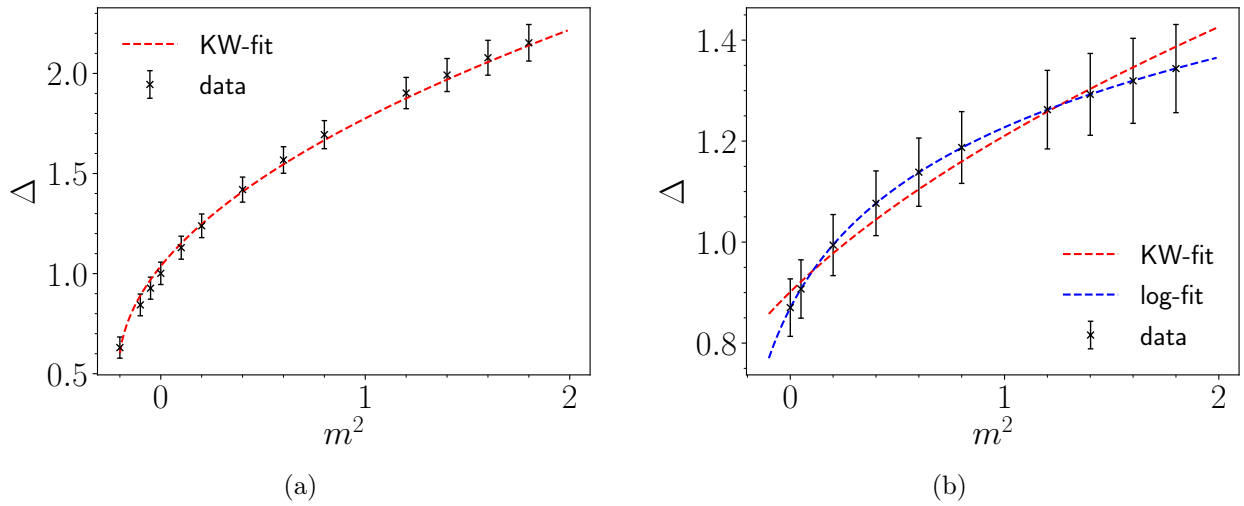


Figure 4.4: Bulk mass dependence of the scaling exponent at (a) $\beta = 3.0$ and (b) $\beta = 1.0$.

equal to its value on the $(3, 7)$ regular hyperbolic disk. Not surprisingly, the peak is sharpened in the strong coupling limit, and we recover the geometry of the fixed tessellated disk with a high probability in our MCMC simulation. The weak coupling limit, where the peak is broad, represents stronger curvature fluctuation in the background hyperbolic manifold. The non-uniform curvature in the geometry can be seen from the snapshots of the geometry during MCMC simulation. Sample configurations at different couplings are shown in Fig. 4.2.

Next, we discuss the main results of our analysis – the boundary-boundary correlator function. We compute the lattice propagators at different couplings β and different bulk masses m . With geometry fluctuation in play, we still find conformal behavior for the correlators for a wide range of couplings. Fig 4.3 shows the boundary correlators at two different couplings for scalar mass $m = 0$. Note that even at a small value of $\beta = 1.0$, where 63% bulk vertices on average are 7-fold connected, we find a signature of conformal behavior. At a stronger coupling of $\beta = 3.0$, where 99.6% vertices are 7-fold connected, we find that the scaling exponent extracted from the linear fit of the correlator matches the Klebanov-Witten relation at Eqn. 4.1. The predicted continuum result of the boundary exponent for the zero bulk mass is $\Delta = 1$ for geometry with constant negative curvature, which matches closely with our numerical result at $\beta = 3.0$.

Next, the scaling exponents for different bulk mass at a fixed β are plotted. Results are shown for $\beta = 3.0$ in the Fig. 4.4a and for $\beta = 1.0$ in the Fig. 4.4b. We use two fit functions, one corresponding to the Klebanov-Witten (KW) formula and corresponding to Eqn. 4.1, written with three fit parameters A , B and L

$$\Delta = A + \sqrt{B + m^2 L^2}. \quad (4.6)$$

The other fit function we use is a logarithmic function with three fit parameters A, B, C expressed as

$$\Delta = A \log(m^2 + B) + C. \quad (4.7)$$

We find that the KW relation fits well in the limit of small fluctuations, whereas the logarithmic fit describes the data better for larger fluctuations.

4.4 Curvature fluctuation from matter fields

In the previous section we presented results on the holographic behavior of a model in which the behavior of a boundary theory is influenced by bulk quantum gravity corrections. The magnitude of the quantum corrections were controlled by an R^2 operator which was added to the action by hand. It is interesting to construct models where such operators could be induced via coupling the system to additional dynamical matter fields. We construct such a model in this section.

We will see that to pick out uniform hyperbolic space we need to employ fermionic matter. To avoid the complication of having to carry around additional structure like a spin connection and frame we have used Kähler-Dirac fermions. The Kähler-Dirac operator squares to the (curved) space Laplacian and allows us to express the effective action in terms of powers of the determinant of the curved space Laplacian. Consider N degenerate Kähler-Dirac (KD) fermions with mass m . The partition function is given by

$$\begin{aligned} Z &= \sum_{\mathcal{T}} \int D\phi e^{-k_2 N_2} \prod_1^N D\phi D\bar{\phi} e^{-\bar{\phi}^a (K-m)\phi^a} \\ &= \sum_{\mathcal{T}} \det^{\frac{N}{2}}(\tilde{\square}) e^{-k_2 N_2}. \end{aligned} \quad (4.8)$$

where, $\tilde{\square}(\mathcal{T}) = -\square(\mathcal{T}) + m^2$. The effective gravitational action can then be written as

$$S = \frac{N}{2} \ln (\det \tilde{\square}) - k_2 N_2 \quad (4.9)$$

It can be seen from the above expression that the Boltzmann factor is given by a non-local term. A local form of the action can be deduced with some approximations. In order to do that, the Laplacian operator is factorized into three matrices

$$\tilde{\square} = DAD$$

where D is a diagonal matrix with diagonal entries $d_i = \sqrt{q_i}$; and A is a matrix that depends on the connectivity of the vertices in a particular triangulation with diagonal and off-diagonal components described by

$$A_{ii} = 1 + m^2,$$

$$A_{ij} = -\frac{1}{\sqrt{q_i q_j}} C_{ij}.$$

In the large mass limit $m \rightarrow \infty$, A only contributes a constant factor. Hence,

$$\det \tilde{\square} \sim (\det D)^2 = \prod_i q_i. \quad (4.10)$$

With this approximation, we arrive at a local form for the action in the large mass limit

$$S_{\text{KD}} = -\frac{N}{2} \sum_{i \in \text{bulk}} \ln(q_i). \quad (4.11)$$

Thus the complete action with the Kähler Dirac fermion is

$$S = S_{\text{KD}} - k_2 N_2 + \lambda(\langle q \rangle - 7). \quad (4.12)$$

The last term in the equation is introduced as a constraint – the average bulk coordination number remains seven during the evolution of the geometry in the MCMC simulation. We find from the numerical analysis that the fixed boundary geometry with identical connectivity to the $\{3, 7\}$ Poincaré disk is sufficient to ensure this constraint. The logarithmic term in the effective action is then equivalent to the curvature-squared term in Eqn. 4.4 since

$$\ln(q_i) \sim -\frac{1}{2\pi^2} R_i^2 + \dots$$

From the discussion above, it is evident that massive Kähler Dirac fermions dynamically generate a curvature squared term. In the $N \rightarrow \infty$ limit, the regular $\{3, 7\}$ tessellation of the Poincaré disk will be recovered with certainty. The number of fermions N plays the same role as β in the previous construction. A transition from a holographic to a non-holographic

regime may exist as N is varied. In this approach with dynamical fermionic matter fields, smaller N amounts to a larger curvature-fluctuation region.

4.5 Kähler Dirac Operator Construction and Results

In this section, we outline the construction of lattice Kähler Dirac fermions. For the details of the construction in the continuum and in the lattice, see this work by Banks *et. el.* [73, 74]. The use of the operator in the context of degenerate triangulation is discussed by Catterall *et. el.* [75].

The Kähler Dirac operator (K) is a square root of the Laplacian operator and in flat spacetime it is possible to show that each Kähler Dirac fermion (KD) is equivalent to two Dirac fermions in two dimensions. The equation of motion of a KD field reads

$$(d - d^\dagger + m)\Omega = 0. \quad (4.13)$$

where, $\Omega = (\omega_0, \omega_\mu, \dots, \omega_{\mu_1 \dots \mu_D})$ is a collection of forms. Construction of the operator K is natural in curved spacetime too, but the equivalence with Dirac spinors disappears. It is easy to see that Laplacian operator can be written as

$$-\square = K^2 = (d - d^\dagger)^2 = -dd^\dagger - d^\dagger d. \quad (4.14)$$

The above expression follows from the fundamental relation in the exterior calculus $d^2 = d^{\dagger 2} = 0$.

One of the most important properties of the Kähler-Dirac equation is that it has a natural discretization on simplicial manifolds. Coboundary \bar{d} and boundary $\bar{\delta} = \bar{d}^T$ operators are introduced which are the lattice equivalent of d and d^\dagger respectively. The lattice operators act on lattice analogs of the continuum p -forms which are associated with p -simplices in the lattice. For example, the action of the $\bar{\delta}$ on a ordered list of vertices (v_1, v_2, v_3) representing a triangle and carrying a 2-form field will return an oriented linear combination of the associated links (v_1, v_2) , (v_2, v_3) and (v_3, v_1) carrying 1-form fields. The detailed construction of the lattice Kähler Dirac operator can be found here [75] for the case of 4D dynamical

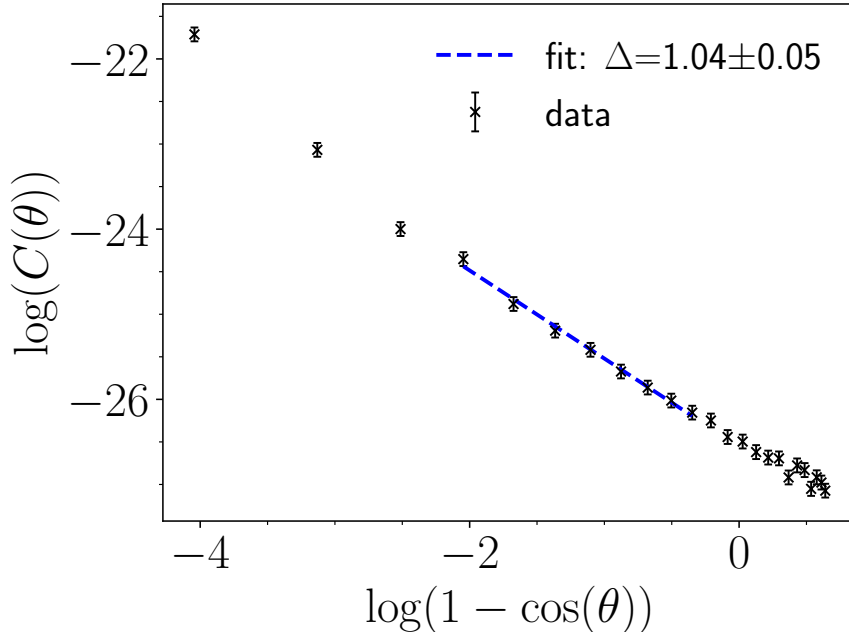


Figure 4.5: Lattice propagator computed from the simulation with $N_f = 10$ Kähler Dirac fermions is plotted against distance-squared $r^2 \propto (1 - \cos \theta)$. The slope Δ of the linear fit denotes the scaling exponent of the boundary field operator.

triangulation. The resultant lattice Laplacian operator is a block diagonal matrix with three non-zero blocks, each associated with different types of simplices in 2D. Thus in Eqn. 4.10, there are contributions from three different matrices associated with vertices, links, and triangles.

We constructed the lattice Kähler Dirac operator to simulate a fluctuating hyperbolic disk equipped with ten Kähler Dirac fermions. Resultant action is described by Eqn. 4.9. We found that the holographic nature of the boundary theory is reproduced in the correlator plot computed from the Markov chain Monte Carlo simulation with KD fermions. The plot is shown in Fig. 4.5.

4.6 Conclusions

In this chapter, we have described some preliminary results of the effects of bulk curvature fluctuations on the holographic behavior of a two-dimensional model formulated on a space whose average curvature is negative. We presented results from two different kinds of sim-

ulations, and they both indicate that the holographic nature of the model survives at least for weak bulk quantum gravity corrections. Further investigation is necessary to provide concrete evidence of conformality in the strongly coupled bulk quantum gravity regime.

We also show how to couple lattice fermions to the system so that the gravity corrections are suppressed for a large number of fields, with the effective action picking up a curvature-squared term. It would be interesting to investigate whether a phase transition exists from the holographic to the non-holographic regime as the number of fermions N is varied. Work in these directions is ongoing, and the results will be published soon.

Chapter 5

Conclusions

The main goal of the thesis was to explore holographic aspects of field theories using lattice techniques. We successfully demonstrated that lattice models were capable of yielding results in agreement with continuum holography. Our first attempt was the computation of the scaling exponents for the boundary field operator of the free scalar field. The mass dependency of the scaling exponent showed excellent matching with the continuum results [17, 20] in both two and three dimensions. Our lattice analysis demonstrates that even with a crude uniform tessellation of geometry, information is recoverable from boundary lattice propagators. Global information of the bulk geometry – the radius of curvature – was also recovered from lattice analysis from the dual lattice prescription. It's non-trivial to implement boundary conditions while investigating holography since boundary field values are required to compute boundary observables. Since naive implementation pushes all the boundary field values to exactly zero, we devised a way to impose a pseudo-Dirichlet boundary condition with the introduction of a large boundary mass. Our lattice analysis revealed the existence of a conformal regime for a wide range of scalar mass, including negative mass-squared cases.

The next step that we took after the successful lattice implementation of a free theory was to understand the conformal boundary behavior for an interacting bulk theory – the 2D Ising model on the Poincaré disk. The main result of this analysis is that we could recover holographic behavior for a range of temperatures from low to high, including the bulk critical temperature. The temperature dependence of the scaling of the boundary operator is derived in two different ways – from the boundary susceptibility and from the two-point function.

The critical temperature is obtained from a bulk computation of the susceptibility, but we showed that the minima of the boundary scaling dimension can also provide the position of the bulk transition. Thus, the holographic nature of the system is evident: finding β for which $\partial_\beta \Delta = 0$ gives the bulk transition temperature. At first glance, it is surprising to find evidence of criticality for the 1D boundary theory for the Ising system since the 1D nearest-neighbor Ising model does not possess any phase transition. However, the effective boundary theory evades this constraint in the presence of long-range interactions which appear as a result of the presence of the bulk. As in the free scalar field model, we have argued that some geometry information, the ratio of intrinsic length scales, can also be recovered from comparing the lattice and dual-lattice data.

In the penultimate chapter of the thesis, we have investigated the effects of allowing for dynamical fluctuations in the geometry which simulates the effect of gravitational fluctuations. Tuning a R^2 term, both perturbative and non-perturbative geometry fluctuation effects can be generated, and a new formula relating the boundary scaling exponent to the bulk mass is proposed in the non-perturbative regime. This chapter also discusses the introduction of Kähler-Dirac (KD) fermions in discrete hyperbolic space. It is shown that with a suitable boundary condition, the matter backreaction of several KD matter fields can strongly influence the nature of the bulk geometry yielding a constant curvature hyperbolic space for large numbers of fields as revealed from the computation of the boundary correlators. It should be stressed that these lattice simulations probe regimes with strong bulk gravity which are inaccessible to analytic approaches.

In the future, we plan to investigate in more detail the effects of varying the number of KD fermions. We also plan to extend the ideas to four spacetime dimensions. Another obvious extension of our work is the introduction of other kinds of matter fields. Some efforts in this direction are ongoing. We are currently investigating Ising gauge matter fields in three spacetime dimensions. We will be attempting to recover the well-known Ryu-Takanagi formula [76] from lattice simulation. Initial attempts have been made to compute the boundary Wilson loop and boundary plaquette-plaquette correlator. The results of the pure Ising gauge theory thus can be verified from the analysis of the Ising model in the dual lattice. It would also be interesting to analyze the holographic aspects of Dirac fields on hyperbolic

lattices adapting the ideas developed in [77] . We also would like to apply holographic ideas to improve our understanding of quantum computation. Specifically, it would be interesting to find a mapping of the tensor network representation of the bulk theory as some effective boundary theory. The mapping would allow the investigation of a gravitational theory with quantum computers by developing quantum circuits and probing the phase space of gravitational models that are not easily accessible with traditional approaches.

To conclude, the techniques developed in this thesis demonstrate that lattice realization of holographic theories is possible. We have also demonstrated that the tools could be used in developing an AdS/CFT dictionary in regimes not accessible with traditional continuum analysis. The tools can be used in developing tensor network models on hyperbolic tessellations and can be used in many applications in quantum information science, including quantum error correction and quantum entanglement entropy computation.

Bibliography

- [1] G. T. Horowitz and J. Polchinski, Approaches to quantum gravity pp. 169–186 (2009).
- [2] G. T. Horowitz and E. J. Martinec, Physical Review D **57**, 4935 (1998).
- [3] V. E. Hubeny, Classical and Quantum Gravity **32**, 124010 (2015).
- [4] D. Mateos, Classical and Quantum Gravity **24**, S713 (2007).
- [5] S. S. Gubser and A. Karch, arXiv preprint arXiv:0901.0935 (2009).
- [6] J. Casalderrey-Solana, H. Liu, D. Mateos, K. Rajagopal, and U. A. Wiedemann, *Gauge/string duality, hot QCD and heavy ion collisions* (Cambridge University Press, 2014).
- [7] P. K. Kovtun, D. T. Son, and A. O. Starinets, Physical review letters **94**, 111601 (2005).
- [8] C. P. Herzog, Journal of Physics A: Mathematical and Theoretical **42**, 343001 (2009).
- [9] J. McGreevy, Advances in High Energy Physics **2010** (2010).
- [10] S. Afonin and A. Katanaeva, Physical Review D **98**, 114027 (2018).
- [11] M. Chernicoff and A. Güijosa, Journal of High Energy Physics **2008**, 005 (2008).
- [12] S. A. Hartnoll, C. P. Herzog, and G. T. Horowitz, Physical Review Letters **101**, 031601 (2008).
- [13] M. Greiner and S. Fölling, Nature **453**, 736 (2008).

- [14] S. Bhattacharyya, S. Minwalla, V. E. Hubeny, and M. Rangamani, *Journal of High Energy Physics* **2008**, 045 (2008).
- [15] G. T. Horowitz and J. E. Santos, arXiv preprint arXiv:1408.5906 (2014).
- [16] J. M. Maldacena, *Int. J. Theor. Phys.* **38**, 1113 (1999), hep-th/9711200.
- [17] E. Witten, *Adv. Theor. Math. Phys.* **2**, 253 (1998), hep-th/9802150.
- [18] C. R. Graham and J. M. Lee, *Advances in mathematics* **87**, 186 (1991).
- [19] S. S. Gubser, I. R. Klebanov, and A. M. Polyakov, *Phys. Lett.* **B428**, 105 (1998), hep-th/9802109.
- [20] I. R. Klebanov and E. Witten, *Nuclear Physics B* **556**, 89 (1999), ISSN 05503213, arXiv: hep-th/9905104, URL <http://arxiv.org/abs/hep-th/9905104>.
- [21] D. Z. Freedman, S. D. Mathur, A. Matusis, and L. Rastelli, *Nuclear Physics B* **546**, 96 (1999).
- [22] W. Mueck and K. Viswanathan, *Physical Review D* **58**, 041901 (1998).
- [23] W. Mueck and K. Viswanathan, *Physical Review D* **58**, 106006 (1998).
- [24] M. Henningson and K. Sfetsos, *Physics Letters B* **431**, 63 (1998).
- [25] R. Rashkov, *Physics Letters B* **466**, 190 (1999).
- [26] G. Chalmers, H. Nastase, K. Schalm, and R. Siebelink, *Nuclear Physics B* **540**, 247 (1999).
- [27] W. l'Yi, arXiv preprint hep-th/9808051 (1998).
- [28] P. Minces and V. O. Rivelles, *Physics Letters B* **455**, 147 (1999).
- [29] H. Liu and A. A. Tseytlin, *Nuclear Physics B* **533**, 88 (1998).
- [30] G. Arutyunov and S. Rolov, *Nuclear Physics B* **544**, 576 (1999).

- [31] S. Corley, Physical Review D **59**, 086003 (1999).
- [32] A. Volovich, Journal of High Energy Physics **1998**, 022 (1998).
- [33] G. Arutyunov and S. Frolov, Physics Letters B **441**, 173 (1998).
- [34] W. l'Yi, Physics Letters B **448**, 218 (1999).
- [35] A. Polishchuk, Journal of High Energy Physics **1999**, 007 (1999).
- [36] P. Breitenlohner and D. Z. Freedman, Annals of physics **144**, 249 (1982).
- [37] P. Minces and V. O. Rivelles, Nuclear Physics B **572**, 651 (2000).
- [38] D. B. Kaplan, J.-W. Lee, D. T. Son, and M. A. Stephanov, Physical Review D **80**, 125005 (2009).
- [39] V. Balasubramanian, P. Kraus, A. Lawrence, and S. P. Trivedi, Physical Review D **59**, 104021 (1999).
- [40] N. Metropolis, A. W. Rosenbluth, M. N. Rosenbluth, A. H. Teller, and E. Teller, The journal of chemical physics **21**, 1087 (1953).
- [41] W. K. Hastings (1970).
- [42] B. A. Berg, *Markov chain Monte Carlo simulations and their statistical analysis: with web-based Fortran code* (World Scientific Publishing Company, 2004).
- [43] W. H. Press, S. A. Teukolsky, W. T. Vetterling, and B. P. Flannery, *Numerical recipes 3rd edition: The art of scientific computing* (Cambridge university press, 2007).
- [44] U. Wolff, Physical Review Letters **62**, 361 (1989).
- [45] R. H. Swendsen and J.-S. Wang, Physical review letters **58**, 86 (1987).
- [46] E. Luijten, H. W. Blöte, and K. Binder, Physical Review E **54**, 4626 (1996).
- [47] E. Luijten and H. W. Blöte, Physical Review B **56**, 8945 (1997).

- [48] A. Hucht, *Journal of Physics A: Mathematical and General* **35**, L481 (2002).
- [49] D. M. Hübscher and S. Wessel, *Physical Review E* **87**, 062112 (2013).
- [50] J. Ambjørn, L. Glaser, A. Görlich, and J. Jurkiewicz, *Journal of High Energy Physics* **2013**, 100 (2013), ISSN 1029-8479, URL [http://link.springer.com/10.1007/JHEP10\(2013\)100](http://link.springer.com/10.1007/JHEP10(2013)100).
- [51] J. Laiho, S. Bassler, D. Coumbe, D. Du, and J. T. Neelakanta, *Physical Review D* **96**, 064015 (2017), ISSN 2470-0010, 2470-0029, arXiv: 1604.02745, URL <http://arxiv.org/abs/1604.02745>.
- [52] R. Loll, *Classical and Quantum Gravity* **37**, 013002 (2019).
- [53] J. Ambjorn, A. Görlich, J. Jurkiewicz, and R. Loll, *International Journal of Modern Physics D* **22**, 1330019 (2013).
- [54] S. McGuire, S. Catterall, M. Bowick, and S. Warner, *Nuclear Physics B* **614**, 467 (2001).
- [55] R. Krmar, A. Gendiar, K. Ueda, and T. Nishino, *Journal of Physics A: Mathematical and Theoretical* **41**, 125001 (2008), URL <https://doi.org/10.1088%2F1751-8113%2F41%2F12%2F125001>.
- [56] S. K. Baek, H. Mäkelä, P. Minnhagen, and B. J. Kim, *Phys. Rev. E* **84**, 032103 (2011), URL <https://link.aps.org/doi/10.1103/PhysRevE.84.032103>.
- [57] D. Benedetti, *Journal of Statistical Mechanics: Theory and Experiment* **2015**, P01002 (2015), URL <https://doi.org/10.1088%2F1742-5468%2F2015%2F01%2Fp01002>.
- [58] N. P. Breuckmann, B. Placke, and A. Roy, *Phys. Rev. E* **101**, 022124 (2020), URL <https://link.aps.org/doi/10.1103/PhysRevE.101.022124>.
- [59] R. C. Brower, C. V. Cofburn, A. L. Fitzpatrick, D. Howarth, and C.-I. Tan, arXiv preprint arXiv:1912.07606 (2019).
- [60] A. Zamolodchikov, *JHEP* **07**, 029 (2002), hep-th/0109078.

- [61] R. C. Brower, M. Cheng, E. S. Weinberg, G. T. Fleming, A. D. Gasbarro, T. G. Raben, and C.-I. Tan, *Phys. Rev. D* **98**, 014502 (2018), 1803.08512.
- [62] H. S. M. Coxeter, in *Proceedings of the International Congress of Mathematicians* (Cite-seer, 1954), vol. 3, pp. 155–169.
- [63] T. Needham, *Visual Complex Analysis* (Oxford University Press, USA, 1999), ISBN 9780198534464, URL <http://amazon.com/o/ASIN/0198534469/>.
- [64] R. Nelson and H. Segerman, *Journal of Mathematics and the Arts* **11**, 4 (2017).
- [65] N. P. Breuckmann, B. Placke, and A. Roy, *Physical Review E* **101**, 022124 (2020), ISSN 2470-0045, 2470-0053, arXiv: 1909.12107, URL <http://arxiv.org/abs/1909.12107>.
- [66] F. Sausset and G. Tarjus, *Journal of Physics A: Mathematical and Theoretical* **40**, 12873 (2007), ISSN 1751-8113, 1751-8121, URL <https://iopscience.iop.org/article/10.1088/1751-8113/40/43/004>.
- [67] R. Krcmar, A. Gendiar, K. Ueda, and T. Nishino, *Journal of Physics A* **41**, 125001 (2008).
- [68] R. Rietman, B. Nienhuis, and J. Oitmaa, *Journal of Physics A: Mathematical and General* **25**, 6577 (1992), ISSN 0305-4470, 1361-6447, URL <https://iopscience.iop.org/article/10.1088/0305-4470/25/24/012>.
- [69] H. Shima and Y. Sakaniwa, *Journal of Physics A: Mathematical and General* **39**, 4921 (2006), ISSN 0305-4470, 1361-6447, URL <https://iopscience.iop.org/article/10.1088/0305-4470/39/18/010>.
- [70] R. Savit, *Reviews of Modern Physics* **52**, 453 (1980).
- [71] R. Mosseri and J. Sadoc, *Journal de Physique Lettres* **43**, 249 (1982).
- [72] M. Asaduzzaman, S. Catterall, J. Hubisz, R. Nelson, and J. Unmuth-Yockey, *Physical Review D* **102**, 034511 (2020), publisher: American Physical Society, URL <https://link.aps.org/doi/10.1103/PhysRevD.102.034511>.

- [73] T. Banks, Y. Dothan, and D. Horn, Physics Letters B **117**, 413 (1982), ISSN 0370-2693, URL <https://www.sciencedirect.com/science/article/pii/0370269382905718>.
- [74] J. M. Rabin, Nuclear Physics B **201**, 315 (1982), ISSN 0550-3213, URL <https://www.sciencedirect.com/science/article/pii/0550321382904345>.
- [75] S. Catterall, J. Laiho, and J. Unmuth-Yockey, Physical Review D **98**, 114503 (2018), ISSN 2470-0010, 2470-0029, URL <https://link.aps.org/doi/10.1103/PhysRevD.98.114503>.
- [76] S. Ryu and T. Takayanagi, Physical review letters **96**, 181602 (2006).
- [77] R. C. Brower, E. S. Weinberg, G. T. Fleming, A. D. Gasbarro, T. G. Raben, and C.-I. Tan, Physical Review D **95**, 114510 (2017).

VITA

AUTHOR: Muhammad Asaduzzaman

NATIONALITY: Bangladeshi

DATE OF BIRTH: May 4, 1990

Education

- **Syracuse University**, Syracuse, NY, 13210, US.
Ph.D. candidate, Department of Physics, August 2016 to present.
Thesis supervisor: Dr. Simon Catterall
- **University of Dhaka**, Dhaka, Bangladesh. M.Sc., department of theoretical Physics, March, 2016.
Thesis supervisor: Dr. Golam Mohammed Bhuiyan
- **Bangladesh University of Engineering & Technology**, Dhaka.
B.Sc., Electrical and Electronic Engineering, February 2013.

Internship Experience

- **Argonne National Lab (ANL)**, Research Aide, computational science division, May 25 to August 14, 2020.
- **CERN**, ALICE collaboration, June 29 to August 21, 2015.

Selected talks

- Quantum Simulation with Interacting Staggered Fermions; APS April meeting, 2022.
- Fermionic Simulation on NISQ-era machines; QuLat Collaboration meeting, 2022.
- Scalar fields on fluctuating hyperbolic geometries; APS April meeting, 2021.
- Fields in fluctuating hyperbolic space; Lattice 2021, the 38th Symposium on the lattice field theory

Teaching Experiences

- Part-time faculty: Physics 211- General Physics-I., Summer-2017 session, department of Physics, Syracuse University.
- Teaching assistant, department of Physics, Syracuse University, Fall 2016-Fall 2020.
- Lecturer, *January 2014 -July 2016*, Dept. of Electrical and Electronics Engineering, Presidency University, Dhaka, Bangladesh.

Academic Honors

- **Research Excellence Doctoral Funding** (REDF) fellowship, academic year 2021-2022, Syracuse University
- 2017 Levinstein Fellowship for **outstanding junior graduate student**, department of physics, Syracuse University
- **‘Dean’s List Scholarship’** during undergraduate studies
- **‘University Merit Scholarship’** for the first year in the undergraduate study
- Completed undergraduate studies with honors

Publication Orcid-ID 0000-0001-7559-3873

1. **Tensor network formulation of two-dimensional gravity**; Muhammad Asaduzzaman, Simon Catterall and Judah Unmuth-Yockey; Phys. Rev. D 102, 054510 (September, 2020)
<https://link.aps.org/doi/10.1103/PhysRevD.102.054510>
2. **Holography on tessellations of hyperbolic space**; Muhammad Asaduzzaman, Simon Catterall, Jay Hubisz, Roice Nelson and Judah Unmuth-Yockey; Phys. Rev. D 102, 034511 (August, 2020)
<https://link.aps.org/doi/10.1103/PhysRevD.102.034511>
3. **Lattice Gauge Theory and Two Dimensional Quantum Gravity** Muhammad Asaduzzaman, Simon Catterall, and Judah Unmuth-Yockey; PoS LATTICE2019 (2020), 043.
<https://pos.sissa.it/363/043>
4. **Holography for Ising spins on the hyperbolic plane**; Muhammad Asaduzzaman, Simon Catterall, Jay Hubisz, Roice Nelson and Judah Unmuth-Yockey; arXiv:2112.00184

[hep-lat].

<https://arxiv.org/abs/2112.00184>

5. **Scalar fields on fluctuating hyperbolic geometries** Muhammad Asaduzzaman, Simon Catterall; prepared for lattice proceedings, 2021; arXiv: 2112.00927 [hep-lat].
<https://arxiv.org/abs/2112.00184>
6. **4D gravity with combinatorial triangulation**; Muhammad Asaduzzaman, Simon Catterall; arXiv:2207.12642 [hep-lat] (July 2022)
<https://arxiv.org/pdf/2207.12642.pdf>
7. **Quantum Simulation of the N flavor Gross-Neveu Model** Muhammad Asaduzzaman; Simon Catterall; Goksu Can Toga; Yannick Meurice; Ryo Sakai; arXiv:2208.05906 [hep-lat] (August 2022)
<https://arxiv.org/abs/2208.05906>

Grant Writing Experience

- Azure Quantum Credits Program, project: “Investigation of $SO(4)$ Invariant Four Fermi model”